



Final Report SPR-FY23(013)

High-Mast Tower Foundation – Phase II

Ammar Al Maabreh, MS

Research Assistant

Durham School of Architectural Engineering and Construction
University of Nebraska-Lincoln

Abdelrahman Awawdeh, MS

Research Assistant

Marc Maguire, PhD

Associate Professor

Jay Puckett, PhD

Professor

Brandon Kreiling

Associate Professor of Practice

Nebraska Department of Transportation Research

Headquarters Address (402) 479-4697
1400 Nebraska Parkway <https://dot.nebraska.gov/business-center/research/>
Lincoln, NE 68509
ndot.research@nebraska.gov

Nebraska Transportation Center

262 Prem S. Paul Research (402) 472-1932
Center at Whittier School <http://ntc.unl.edu>
2200 Vine Street
Lincoln, NE 68583-0851

This report was funded in part through grant from the U.S. Department of Transportation Federal Highway Administration. The views and opinions of the authors expressed herein do not necessarily state or reflect those of the U.S. Department of Transportation.

High-Mast Tower Foundation – Phase II

Ammar Al Maabreh, MS
Research Assistant
Durham School of Architectural
Engineering and Construction
University of Nebraska-Lincoln

Jay Puckett, PhD
Emeritus Professor
Fmr. Director, Durham School of
Architectural Engineering and Construction
University of Nebraska-Lincoln

Abdelrahman Awawdeh, MS
Research Assistant
Durham School of Architectural
Engineering and Construction
University of Nebraska-Lincoln

Brandon Kreiling
Associate Professor of Practice
Durham School of Architectural
Engineering and Construction
University of Nebraska-Lincoln

Marc Maguire, PhD
Associate Professor
Durham School of Architectural
Engineering and Construction
University of Nebraska-Lincoln

Sponsored By
Nebraska Department of Transportation and U.S. Department of Transportation Federal
Highway Administration

September 30th 2024

TECHNICAL REPORT DOCUMENTATION PAGE

1. Report No. SPR-FY23(013)		2. Government Accession No.		3. Recipient's Catalog No.	
4. Title and Subtitle High-Mast Tower Foundation – Phase II				5. Report Date September, 2024	
				6. Performing Organization Code	
7. Author(s) Ammar Al Maabreh, Abdelrahman Awawdeh, Marc Maguire, Jay Puckett, Brandon Kreiling				8. Performing Organization Report No. SPR-FY23(013)	
9. Performing Organization Name and Address University of Nebraska-Lincoln 1110 South 67 th St. Omaha, Nebraska 68182-0178				10. Work Unit No.	
				11. Contract	
12. Sponsoring Agency Name and Address Nebraska Department of Transportation Research Section 1400 Nebraska Parkway Lincoln, NE 68502				13. Type of Report and Period Covered Final Report October 2022 – September, 2024	
				14. Sponsoring Agency Code	
15. Supplementary Notes					
16. Abstract					
17. Key Words High-Mast Tower Foundation			18. Distribution Statement No restrictions. This document is available through the National Technical Information Service. 5285 Port Royal Road Springfield, VA 22161		
19. Security Classification (of this report) Unclassified		20. Security Classification (of this page) Unclassified		21. No. of Pages 190	22. Price
Form DOT F 1700.7 (8-72)			Reproduction of completed page authorized		

Table of Contents

Disclaimer	xi
Acknowledgments	xii
Executive Summary	xiii
Chapter 1 Introduction	1
1.1 Background	1
1.2 Research Objective	2
1.3 Research Benefits.....	2
Chapter 2 Literature Review	4
2.1 Introduction.....	4
2.2 Research Literature	4
Chapter 3 Design and Pole Installation.....	6
3.1 Test Pole Design	6
3.2 Design Procedure	17
3.3 Installation.....	17
Chapter 4 Field Evaluation Tests	27
4.1 Instrumentation	27
4.2 Summary of All Experimental Tests Performed.....	39
Chapter 5 Analysis Methods.....	41
5.1 p-y Analysis Description.....	41
5.2 Frame Model.....	46
5.3 Dynamic Analysis Methods.....	48
Chapter 6 Experimental Results and Analysis.....	51
6.1 Static Test Results.....	51
6.2 Pluck Test Results.....	66
6.3 Forced-Vibration Test Results	77
6.4 Finite Element Analysis Results.....	79
6.5 Observed Damage and Failure Modes.....	85
Chapter 7 Discussion	87
7.1 Load performance of the foundation.....	87
7.2 Effect of damping on design.....	96
Chapter 8 Conclusions	103
8.1 Summary	103
8.2 Conclusions.....	103
References.....	107
Appendix A Early Design Computations (prior to establishing the shaft diameter and depths)	108
Appendix B Force Vibration Response via FFT.....	123
Appendix C Inclinometer Rotations	135
Appendix D Inclinometer Rotations at Maximum, 0.5 Maximum (approximate design), and Unloaded.....	146
Appendix E Discussion on Musco Foundations	160
Appendix F NDOT Sample Construction Specification for Direct Embedded Poles	163
Appendix G Service Analysis of NDOT Pole Design	174
Appendix H Concrete Foundation Mixture Design.....	175

List of Figures

Figure 1.1 High-mast Lighting Tower in Milford, Nebraska (photo provided by NDOT)	1
Figure 3.1 Borehole report	7
Figure 3.2 Tested poles in the field before installation.....	8
Figure 3.3 Pole geometries	9
Figure 3.4 Poles geometry	13
Figure 3.5 Section for directly embedded foundations of poles with concrete backfill	16
Figure 3.6 Section in directly embedded foundations of poles with gravel backfill	16
Figure 3.7 Auger Drive Digger used to excavate the holes	19
Figure 3.8 Installing the concrete donuts and welding the steel plates to the top of the poles.....	20
Figure 3.9 Lifting the pole using a crane and placing it inside the hole.....	21
Figure 3.10 Process of attaching the inclinometer casing to the pole.....	22
Figure 3.11 Installing the pole vertically in the pole and make sure it is installed at the center ..	23
Figure 3.12 Placing the concrete backfill and using an electric vibrator to ensure proper compaction.....	24
Figure 3.13 Placing the gravel backfill and using an electric tamper to ensure uniformly compacted around the annulus.....	25
Figure 3.14 Poles in the field at the end of the installation process.....	26
Figure 4.1 The Vertical In-Place Inclinometer System Model 6180	27
Figure 4.2 Layout of the casing and inclinometer for each embedment length.....	28
Figure 4.3 Tension S beam load cell with a capacity of 10 kips used in the static tests.....	29
Figure 4.4 String potentiometer used to measure the transverse translation near the ground surface	29
Figure 4.5 STS404 Wireless Intelliducer Node	30
Figure 4.6 STS4 Wireless Base Station	30
Figure 4.7 Steel cable connected to the top of the pole for static and pluck tests	31
Figure 4.8 Pull setup for static and pluck tests	31
Figure 4.9 Measuring the transverse translation near the ground surface using a string potentiometer for static tests	32
Figure 4.10 Static test (one direction).....	32
Figure 4.11 Accelerometers used to measure the acceleration at different locations during dynamic tests.....	33
Figure 4.12 Locations of accelerometers installed for the dynamic tests for 12- and 16-ft direct embedments	34
Figure 4.13 Pluck test before release	34
Figure 4.14 Static test and pluck test setup.....	35
Figure 4.15 APS 400 Electro-SEIS shaker used in the forced vibration test.....	36
Figure 4.16 Installation of the shaker at the top of each pole before the forced vibration test....	36
Figure 4.17 The APS 145 power amplifier and the signal generator used in the forced vibration test.....	37
Figure 4.18 The installation of BDI accelerometers on the poles to measure the acceleration during forced vibration test.....	37
Figure 4.19 Forced-vibration test setup	38
Figure 5.1 Steel pipe section used to model the part of the pole above the ground surface.....	42
Figure 5.2 Case 1 – modeled in LPILE with a Round Shaft with casing and core/insert, and 16-ft embedment depth	42

Figure 5.3 Case 2 – modeled in LPILE with Round Shaft with casing and core/insert, and 16-ft embedment depth	43
Figure 5.4 Case 3 – modeled in LPILE with steel pipe section and 16-ft embedment depth.....	44
Figure 5.5 Case 4 – modeled in LPILE with steel pipe section and 12-ft embedment depth.....	44
Figure 5.6 Case 5 – modeled in LPILE with steel pipe section, and 16-ft embedment depth surrounding with gravel medium	45
Figure 5.7 Case 6 – modeled in LPILE with steel pipe section, and 12-ft embedment depth surrounding with gravel medium	45
Figure 5.8 Modeled section in SAP2000™ for the foundation of Case 1 and Case 2.....	46
Figure 5.9 Models developed in SAP2000™ for Case 1 and Case 2	47
Figure 5.10 Models developed in SAP2000™ for Cases 3 through 6.....	48
Figure 5.11 Illustration of a log-decrement method to calculate the damping ratio	49
Figure 5.12 Illustration of half-power bandwidth method to calculate the damping ratio	50
Figure 6.1 The load and moment vs translation at ground level of static tests performed on pole 16–Concrete	51
Figure 6.2 The load and moment vs translation at ground level of static tests performed on pole 16–Gravel.....	52
Figure 6.3 The load and moment vs translation at ground level of static tests performed on pole 12–Concrete	52
Figure 6.4 The load and moment vs translation at ground level of static tests performed on pole 12–Gravel.....	53
Figure 6.5 Reduction in stiffness for all poles as more static tests performed (tests 1-3 are pulled in one direction, and 4-6 are pulled in the opposite direction)	55
Figure 6.6 Translation vs depth of static tests on SE direction performed on pole 16 – Concrete, the 700-yr design load is approximately 0.5 of the maximum load.....	58
Figure 6.7 Translation vs depth of static tests on NE direction performed on pole 16 – Gravel, the 700-yr design load is approximately 0.5 of the maximum load	59
Figure 6.8 Translation vs depth of static tests on SW direction performed on pole 16–Gravel, the 700-yr design load is approximately 0.5 of the maximum load	60
Figure 6.9 Translation vs depth of static tests on NE direction performed on pole 12–Concrete, the 700-yr design load is approximately 0.5 of the maximum load.....	61
Figure 6.10 Translation vs depth of static tests on SW direction performed on pole 12–Concrete, the 700-yr design load is approximately 0.5 of the maximum load.....	62
Figure 6.11 Translation vs depth of static tests on NE direction performed on pole 12–Gravel, the 700-yr design load is approximately 0.5 of the maximum load	63
Figure 6.12 Translation vs depth of static tests on SW direction performed on pole 12–Gravel, the 700-yr design load is approximately 0.5 of the maximum load.....	64
Figure 6.13 Time vs acceleration response of the pluck tests performed in the NW direction for pole 16–Concrete	68
Figure 6.14 Time vs acceleration response of the pluck tests performed in the SE direction for pole 16–Concrete.....	68
Figure 6.15 Time vs acceleration response of the pluck tests performed in the NE direction for pole 16–Gravel.....	69
Figure 6.16 The time vs acceleration response of the pluck tests performed in the SW direction for pole 16–Gravel.....	69

Figure 6.17 Time vs acceleration response of the pluck tests performed in the NE direction for pole 12–Concrete	70
Figure 6.18 Time vs acceleration response of the pluck tests performed in the SW direction for pole 12–Concrete.....	70
Figure 6.19 Time vs acceleration response of the pluck tests performed in the NE direction for pole 12–Gravel	71
Figure 6.20 Time vs acceleration response of the pluck tests performed in the SW direction for pole 12–Gravel.....	71
Figure 6.21 Comparison between the damping performance for poles with different backfill material	72
Figure 6.22 The reduction in damping ratio with time for 16-Gravel pole (a) 5-cycle running, and (b) 7-cycle running.....	73
Figure 6.23 The reduction in damping ratio with time for 12-Gravel pole (a) 5-cycle running, and (b) 7-cycle running.....	74
Figure 6.24 The change in damping ratio with amplitude for (a) 16-Gravel pole, and (b) 12-Gravel pole.....	75
Figure 6.25 Mode shapes and natural frequencies obtained from FEA for Case 1	79
Figure 6.26 Mode shapes and natural frequencies obtained from FEA for Case 2	79
Figure 6.27 Mode shapes and natural frequencies obtained from FEA for Case 3	80
Figure 6.28 Mode shapes and natural frequencies obtained from FEA for Case 4	80
Figure 6.29 Mode shapes and natural frequencies obtained from FEA for Case 5	81
Figure 6.30 Mode shapes and natural frequencies obtained from FEA for Case 6	81
Figure 6.31 Comparison between LPILE cases for gravel backfill (a) 16-foot gravel backfilled pole, and (b) 12-foot backfilled pole.....	83
Figure 6.32 Observed damage in poles with concrete backfill after static tests.....	85
Figure 6.33 Observed damage in poles with gravel backfill after static tests.....	86
Figure 7.1 Comparison between translation profiles obtained from experimental results for poles with different backfill and embedment depths at various loads (a) pole with concrete backfill and different 16-ft embedment, (b) pole with gravel backfill and different embedment depths, (c) pole with 16-ft embedment depth and concrete backfill, and (d) poles with 12-ft embedment depth and gravel backfill.....	88
Figure 7.2 Comparison between translation at ground level obtained from experimental results for poles with different backfill and embedment depths (a) poles with concrete backfill and different embedment depths, (b) poles with gravel backfill and different embedment depths, (c) poles with 16-ft embedment depth and different backfill, and (d) poles with 12-ft embedment depth and different backfill	89
Figure 7.3 Comparison between the translation profile obtained from experimental results and LPILE for poles with different backfill and embedment depths at various loads (a) pole with concrete backfill and 16-ft embedment depths, (b) pole with concrete backfill and 12-ft embedment depths, (c) pole with gravel backfill and 16-ft embedment depths, and (d) pole with gravel backfill and 12-ft embedment depths	92
Figure 7.4 Comparison between translation at ground level obtained from experimental results and LPILE for poles with different backfill and embedment depths (a) pole with concrete backfill and 16-ft embedment depths, (b) pole with concrete backfill and 12-ft embedment depths, (c) pole with gravel backfill and 16-ft embedment depths, and (d) pole with gravel backfill and 12-ft embedment depths.....	93

Figure 7.5 Comparison between translation profiles obtained from LPILE for cases with different backfill and embedment depths at various loads (a) cases with concrete backfill and different embedment depths, (b) cases with different backfill and 16-ft embedment depths, (c) cases with gravel backfill and different embedment depths, and (d) cases with different backfill and 12-ft embedment depths.....	94
Figure 7.6 A comparison between translation at ground level obtained from LPILE for poles with different backfill and embedment depths (a) cases with concrete backfill and different embedment depths, (b) cases with different backfill and 16 ft embedment depths, (c) cases with gravel backfill and different embedment depths, and (d) cases with different backfill and 12-ft embedment depths.....	95
Figure 7.7 Two 5"x7" unreinforced access holes (courtesy of WYDOT).....	99
Figure 7.8 Pole translation in a galloping event (courtesy Utah DOT).....	100
Figure 7.9 Wind-tunnel testing of a multisided pole section (courtesy of WYDOT).....	101
Figure B.1 The results of FFT of the forced vibration test performed on the NW direction on Pole 16-Concrete showing the natural frequency of first mode shape	123
Figure B.2 The results of FFT of the forced vibration test performed in the NW direction on Pole 16-Concrete showing the natural frequency of the second mode shape.....	123
Figure B.3 The results of FFT of the forced vibration test performed in the NW direction on Pole 16-Concrete showing the natural frequency of the third mode shape	124
Figure B.4 The results of FFT of the forced vibration test performed in the SE direction on Pole 16-Concrete showing the natural frequency of the first mode shape.....	124
Figure B.5 The results of FFT of the forced vibration test performed on the SE direction in Pole 16-Concrete showing the natural frequency of the second mode shape.....	125
Figure B.6 The results of FFT of the forced vibration test performed on the SE direction in Pole 16-Concrete showing the natural frequency of the third mode shape	125
Figure B.7 The results of FFT of the forced vibration test performed on the NE direction on Pole 16-Gravel showing the natural frequency of first mode shape.....	126
Figure B.8 The results of FFT of the forced vibration test performed in the NE direction on Pole 16-Gravel showing the natural frequency of the second mode shape	126
Figure B.9 The results of FFT of the forced vibration test performed in the NE direction on Pole 16-Gravel showing the natural frequency of the third mode shape.....	127
Figure B.10 The results of FFT of the forced vibration test performed in the SW direction on Pole 16-Gravel showing the natural frequency of the first mode shape.....	127
Figure B.11 The results of FFT of the forced vibration test performed on the SW direction in Pole 16-Gravel showing the natural frequency of the second mode shape	128
Figure B.12 The results of FFT of the forced vibration test performed on the SW direction on Pole 16-Gravel showing the natural frequency of third mode shape.....	128
Figure B.13 The results of FFT of the forced vibration test performed in the NE direction on Pole 12-Concrete showing the natural frequency of the first mode shape.....	129
Figure B.14 The results of FFT of the forced vibration test performed on the NE direction on Pole 12-Concrete showing the natural frequency of second mode shape.....	129
Figure B.15 The results of FFT of the forced vibration test performed in the NE direction on Pole 12-Concrete showing the natural frequency of the third mode shape	130
Figure B.16 The results of FFT of the forced vibration test performed in the SW direction on Pole 12-Concrete showing the natural frequency of the first mode shape	130

Figure B.17 The results of FFT of the forced vibration test performed on the SW direction on Pole 12-Concrete showing the natural frequency of second mode shape.....	131
Figure B.18 The results of FFT of the forced vibration test performed in the SW direction on Pole 12-Concrete showing the natural frequency of the third mode shape	131
Figure B.19 The results of FFT of the forced vibration test performed in the NE direction on Pole 12-Gravel showing the natural frequency of the first mode shape	132
Figure B.20 The results of FFT of the forced vibration test performed in the NE direction on Pole 12-Gravel showing the natural frequency of the second mode shape	132
Figure B.21 The results of FFT of the forced vibration test performed in the NE direction on Pole 12-Gravel showing the natural frequency of the third mode shape	133
Figure B.22 The results of FFT of the forced vibration test performed on the SW direction on Pole 12-Gravel showing the natural frequency of first mode shape	133
Figure B.23 The results of FFT of the forced vibration test performed in the SW direction on Pole 12-Gravel showing the natural frequency of the second mode shape	134
Figure B.24 The results of FFT of the forced vibration test performed in the SW direction on Pole 12-Gravel showing the natural frequency of the third mode shape	134
Figure C.1 The results of the first static test performed in the SE direction on Pole 16-concrete showing the inclination vs load and moment.....	135
Figure C.2 The results of the second static test performed in the SE direction on Pole 16-Concrete showing the inclination vs load and moment	135
Figure C.3 The results of the third static test performed in the SE direction on Pole 16-Concrete showing the inclination vs load and moment.....	136
Figure C.4 The results of the first static test performed in the NE direction on Pole 16-Gravel showing the inclination vs load and moment.....	136
Figure C.5 The results of the second static test performed in the NE direction on Pole 16-Gravel showing the inclination vs load and moment.....	137
Figure C.6 The results of the third static test performed in the NE direction on Pole 16-Gravel showing the inclination vs load and moment.....	137
Figure C.7 The results of the first static test performed in the SW direction on Pole 16-Gravel showing the inclination vs load and moment.....	138
Figure C.8 The results of the second static test performed in the SW direction on Pole 16-Gravel showing the inclination vs load and moment.....	138
Figure C.9 The results of the third static test performed in the SW direction on Pole 16-Gravel showing the inclination vs load and moment.....	139
Figure C.10 The results of the first static test performed in the NE direction on Pole 12-Concrete showing the inclination vs load and moment.....	139
Figure C.11 The results of the second static test performed in the NE direction on Pole 12-Concrete showing the inclination vs load and moment	140
Figure C.12 The results of the third static test performed in the NE direction on Pole 12-Concrete showing the inclination vs load and moment.....	140
Figure C.13 The results of the first static test performed in the SW direction on Pole 12-Concrete showing the inclination vs load and moment.....	141
Figure C.14 The results of the second static test performed in the SW direction on Pole 12-Concrete showing the inclination vs load and moment	141
Figure C.15 The results of the third static test performed in the SW direction on Pole 12-Concrete showing the inclination vs load and moment	142

Figure C.16 The results of the first static test performed in the NE direction on Pole 12-Gravel showing the inclination vs load and moment.....	142
Figure C.17 The results of the second static test performed in the NE direction on Pole 12-Gravel showing the inclination vs load and moment.....	143
Figure C.18 The results of the second static test performed in the NE direction on Pole 12-Gravel showing the inclination vs load and moment.....	143
Figure C.19 The results of the first static test performed in the SW direction on Pole 12-Gravel showing the inclination vs load and moment.....	144
Figure C.20 The results of the second static test performed in the SW direction on Pole 12-Gravel showing the inclination vs load and moment.....	144
Figure C.21 The results of the third static test performed in the SW direction on Pole 12-Gravel showing the inclination vs load and moment.....	145
Figure D.1 The rotation vs inclination at ground level of static test 11 and 12 in SE direction performed on pole 16 – Concrete, the 700-yr design load is approximately 0.5 of the maximum load	146
Figure D.2 The rotation vs inclination at ground level of static tests 18 and 19 in NE direction performed on pole 16 – Gravel, the 700-yr design load is approximately 0.5 of the maximum load	148
Figure D.3 The rotation vs inclination at ground level of static test 25 and 26 in SW direction performed on pole 16 – Gravel, the 700-yr design load is approximately 0.5 of the maximum load	150
Figure D.4 The rotation vs inclination at ground level of static tests 32 and 33 in NE direction performed on pole 12 – Concrete, the 700-yr design load is approximately 0.5 of the maximum load	152
Figure D.5 The rotation vs inclination at ground level of static tests 39 and 40 in SW direction performed on pole 12 – Concrete, the 700-yr design load is approximately 0.5 of the maximum load	154
Figure D.6 The rotation vs inclination at ground level of static tests 46 and 47 in NE direction performed on pole 12 – Gravel, the 700-yr design load is approximately 0.5 of the maximum load	156
Figure D.7 The rotation vs inclination at ground level of static tests 53 and 54 on SW direction performed on pole 12 – Gravel, the 700-yr design load is approximately 0.5 of the maximum load	158
Figure E.1 Example foundation (https://cms5.revize.com/revize/orionparks/RFP/2020/Ballfield%20Lighting%20RFP/2016.08.17%20-%20musco%20lighting%20submittal%20-%20revised%202%20-%20signed.pdf)	162

List of Tables

Table 3.1 Results of borehole report showing the soil layers with their properties.....	8
Table 3.2 The geometry properties of each pole.....	14
Table 3.3 Embedment length and backfill material used for each pole.....	14
Table 4.1 Summary of experimental tests performed showing the test number, test performed, direction, embedment length and backfill type.....	39
Table 5.1 Investigated cases using LPILE.....	41
Table 6.1 Stiffness calculations for all static tests performed	54
Table 6.2 Results of the pluck tests performed on the poles showing the damping ratio in each direction	67
Table 6.3 The natural frequencies determined from the FFT analysis	77
Table 6.4 Percent reduction observed in the natural frequencies	77
Table 6.5 Damping ratios calculated using Half-Power Band Width.....	78
Table 6.6 Comparison between the natural frequencies obtained from the experimental results and the FEA results.....	81
Table 7.1 Effect of damping on fatigue loads.....	98
Table E.1 AASHTO Standard Specification LTS summary	160
Table H.1 Concrete Mixture Design for the high-mast tower concrete foundations.....	175

Disclaimer

The contents of this report reflect the views of the authors, who are responsible for the facts and the accuracy of the information presented herein. The contents do not necessarily reflect the official views or policies of either the Nebraska Department of Transportations or the University of Nebraska-Lincoln. This report does not constitute a standard, specification, or regulation. Trade or manufacturers' names, which may appear in this report, are cited only because they are considered essential to the objectives of the report.

The United States (U.S.) government and the State of Nebraska do not endorse products or manufacturers. This material is based upon work supported by the Federal Highway Administration under contract SPR-P1 FY23(013). Any opinions, findings and conclusions or recommendations expressed in this publication are those of the author(s) and do not necessarily reflect the views of the Federal Highway Administration.”

This report has been reviewed by the Nebraska Transportation Center for grammar and context, formatting, and compliance with Section 508 of the Rehabilitation Act of 1973.

Acknowledgments

The authors thank the Nebraska Department of Transportation, which provided funding, staff for technical review, resources for the boring logs, and the test site. Also, the authors thank Kansas DOT for providing the poles, and a special thank you to Peak Contracting Group, who provided resources to drill the shafts and install the foundations. Kiewit Engineering provided the engineering analysis and design of the shaft based on their experience with the electrical utility industry. This confirmation of our work was necessary. All these contributions were invaluable.

Executive Summary

Challenge: High-mast luminaire supports used in the US transportation sector are typically steel poles that are attached to a baseplate via a butt or socket weld. Many have failed primarily due to fatigue cracking at the weld toe. Significant research in the US improved the fatigue performance of these structures; however, failures still occur due to high-cycle cracking at the weld toes, or at other fatigue-prone details. Additionally, poles are failing in moderate winds that create galloping. Galloping is an aerodynamic phenomenon where the wind excitation frequency matches the pole's natural frequency creating resonance. The top amplitudes are many times the pole tip diameter, e.g., 30 ft one way due to the inherently low damping. These movements and associated strains create low-amplitude fatigue (repeated yielding) typically causing the pole to fall.

Alternative design: An alternative to the traditional design is to directly embed the pole into a foundation shaft and backfill with concrete or gravel. This eliminates the fatigue-prone details associated with baseplates, welds, bolts, anchorages, and rebars. This process is routinely used in the electrical utility, telecom, and sports-lighting sectors. It can potentially remove the fatigue issue, provide a cheaper fabrication and construction method, and increase damping.

Research: This research was conducted in two phases: Phase I reviewed the literature, specifications, best practices, and construction methods. Phase II used this work to design, construct, and test four poles to near failure. Phase II work is the focus of this report. Four pole foundations were designed: two with concrete and two with gravel backfill. Two foundation depths of 12 and 16 ft were used, and the pole diameters were 36 in. The boring log was used to support LPILE (Ensoft Inc., 2022) and other analyses to check these designs and predict the performance. The AASHTO 700-year mean recurrence interval (MRI) wind load was applied to NDOT's new standard 80-ft luminaire pole, and these reactions were used as the basis for this research.

Dynamic pluck tests were conducted in one direction followed by three static pulls near the 3000-year design load. Damping and hysteretic behavior were observed. Next, forced vibration was used to excite the pole over a range of frequencies, including the pole's first three modes of vibration. The frequency response curves were developed. The load direction was then moved to the opposite direction, and all tests were repeated.

Observations: The groundline translations were within an inch in all cases. The hysteretic behavior was stable after some initial translations. As expected, the gravel foundations had more movement than the concrete, and the 12-ft foundation moved more than the 16-ft foundation. The downhole translations compared with the LPILE predictions. The 12-ft translation near the bottom indicates translation in the opposite direction of the pull and the rotation at that level was non-zero. The 16-ft foundation had a smaller translation near the bottom, and the rotation was smaller, indicating that the p-y behavior had become small. All these designs were reasonably aggressive, especially the 12-Concrete. The goal was to use a foundation small enough to obtain meaningful, and large enough data for analysis to support design.

Damping is essential to mitigate large-amplitude events. The wind speed whereby galloping will lock-in is a function of damping. This critical velocity is directly proportional to the damping ratio. Therefore, the inherent damping associated with direct embedment can drive the critical lock-in velocity to longer MRIs, significantly eliminating these troublesome events.

Summary: These tests demonstrated the application of direct embedment for high-mast towers used in the transportation sector. The tested poles behaved well even under extreme loads much

larger than the 700-MRI design wind. The design requires a p-y analysis for the soil conditions to estimate the groundline translations. Acceptable (codified) translations have not yet been set and this research will help to guide those judgments. To set standards, NDOT could develop conservative shaft details for soil profiles typically located in this state. Although the designs in this research were shallow by design, increasing the depth to provide a more conservative shaft could provide yet more safety at a small marginal cost. Finally, these foundations are especially ductile, tough, and resilient as large displacements that might create voids can be readily backfilled.

Chapter 1 Introduction

1.1 Background

High-mast tower (HMT) foundations have been traditionally designed and constructed using cast-in-place foundations with anchor bolts to secure the tower to the foundation. This type of design requires a base plate that is welded to the tower shaft as shown in Figure 1.1(a). The Nebraska Department of Transportation (NDOT) has recently experienced issues with stresses that this type of design presents at the anchor bolt/foundation or base plate/tower shaft interface. In the worst cases, this issue may lead to a premature failure due to high-cycle fatigue as shown in one of the towers at Milford, Nebraska that fell during a winter snowstorm event in 2018.



(a) High-mast Tower Base Plate, Anchor, Non-shrink Grout, and Cast-in-Place Foundation



(b) High-mast Tower Failure (cite)

Figure 1.1 High-mast Lighting Tower in Milford, Nebraska (photo provided by NDOT)

There have been several research efforts in the past decade to evaluate the fatigue behavior of these HMTs (Thompson 2011, Connor et al. 2012) to propose retrofit strategies that could reduce wind-induced vibrations observed in these structures (Ahearn and Puckett, 2010). Goode and van de Lindt (2007) developed a reliability-based design procedure for High-mast Lighting Towers while Connor and Hodgson (2006) conducted field instrumentation and pluck tests on these structures to measure the dynamic characteristics.

While most previous studies have focused on the 100-120 ft tall structures, there is limited, or no research conducted for the substructure related to these towers. All research related to load effects, mitigation of vibrations, and/or resistance of the pole-to-baseplate connection always evaluates the connection to a plate that is bolted for the foundation.

A Phase I study was conducted to investigate alternatives to the traditional baseplate by eliminating this fail-prone connection by directly embedding the poles. With this project, SPR-P1(20) M111 (Phase I), our UNL/NDOT team explored direct embedment. Direct embedment means placing the pole within a drilled shaft and backfilling the shaft with either concrete or aggregate, eliminating the fatigue-prone baseplate, anchor bolts, and welds required by a typical

design. Phase I addressed a review of the research literature, design specifications, state of practice in electrical- and communication-tower embedment, and corrosion. A mastic layer is typically provided for corrosion protection. Next, the required resistance for a typical NDOT tower was computed with the developed tools. The foundation analysis and designs were conducted for sandy and clay soils typical in Nebraska with the resistance established. A finite element tool was developed for rigorous analysis, combined with analysis from LPILE, an industry standard. Finally, and significantly, site conditions and construction practices were documented. An appendix was developed that outlines project requirements, execution methods, and construction documentation. The Phase I report should be reviewed with this report. The information included therein is not necessarily repeated in this report. Note that Phase I does not include testing.

1.2 Research Objective

This research project aims to develop an alternative design for HMT foundations that can eliminate fatigue-prone details associated with the pole-to-base plate connection, which is the primary location of failure. To address critical issues, the objectives are to:

1. Develop a pole design and procedures for the construction of foundations for high-mast poles.
2. Demonstrate these procedures with the installation of high-mast poles.
3. Confirm the performance with static tests to approximate the design winds.
4. Obtain damping ratios for these poles.
5. Dynamically test the poles to model long-term performance under dynamic loads.
6. Based on these findings, provide design and construction provisions to be integrated into NDOT specifications for design and construction.
7. Document the work product in a final report.
8. Share results nationally via AASHTO's Committee on Bridges and Structures – Traffic Structures Technical Committee with the hope of improving design specifications.

1.3 Research Benefits

The main goal of this research is to eliminate problematic fatigue-prone details, create a safer, longer-lasting design, and decrease the cost associated with the fabrication of the baseplate, welding, and NDT. This study will help eliminate the need to inspect in-service welding and bolt tightness. The construction practice and installation methods are documented.

This research will help Nebraska to lead the US by being the first state to employ this method in high-mast structures and extend this application to mast-arm structures and sign bridges.

Chapter 2 Literature Review

2.1 Introduction

The literature review performed on Phase I is considered sufficient; thus, more information about previous studies and field tests can be found in the Phase I report. No recent studies were found, so some studies that investigated the high-mast towers are mentioned below.

2.2 Research Literature

One of the primary concerns with high-mast towers and similar transportation sector structures is the base plate fatigue issues. For this reason, much of the literature has focused on this work, and some of it is summarized in the Phase I report. The goal of the present investigation is to eliminate concerns with base-plate fatigue and cracking. The purpose of the literature summary below is to summarize work that has been conducted because the Phase I report and to illustrate the concerns of the industry that can now be avoided using the direct embed method.

Several studies have investigated the base plate connection on high-mast towers (Warpinski et al., 2010) suggesting that the base plate connection's geometric characteristics affect the connection's flexibility. Warpinski et al. (2010) investigated the effect of base connection geometry on the fatigue performance of high-mast towers with a parametric study using a finite element model with different base plate thicknesses, tube wall thicknesses, and anchor rod configurations. The results showed that the fatigue life can be improved by increasing the base plate thickness due to decreased stress in the tube wall.

Another finite element model of the base plate connection was developed by Nasouri et al. (2019) to investigate the influence of crack development during the galvanizing process of steel connections. The results showed the regions with the highest potential for crack development which can inform the required strength of steel to prevent cracks from developing. Frymoyer & Berman (2010) outlined the research results of experimental fatigue testing and finite element analysis of luminaire support structures conducted by Transportation Northwest (TransNow) and Washington State Transportation Center (TRAC). The motivation was to help TRAC develop rational inspection procedures to inspect and replace luminaire support structures that exceed their design lifetime. Two in-service poles were investigated and tested by performing quasi-static and high-cycle fatigue tests and used to validate a finite element model. The finite element model investigated the effect of base plate geometry, such as base plate thickness. Finally, based on the two poles and the finite element model results, a framework was developed to estimate the remaining lifetime of luminaire support structures in Washington State.

The Iowa Department of Transportation conducted a field study on two high-mast towers in Iowa (Connor et al., 2007). Several static and dynamic tests were performed to determine the natural frequencies and damping characteristics. Moreover, a long-term investigation was conducted to outline the tower's response under wind load. Another field study, a long-term monitoring study, was performed by Sherman & Connor (2019), on 11 high-mast lighting towers at different locations in the United States. Wind and strain data were collected for two years at each location to predict the response at different stages of the towers' lifetimes. The collected data were used to generate stress-range histograms. The results help to modify the AASHTO specifications for luminaire structural supports.

Wind-induced stress was investigated (Puckett & Ahearn, 2010) to characterize the effects of the lock-in phenomenon that occurs in high-mast lighting towers when subjected to a small range of wind speeds. The study took place in Laramie, Wyoming, with two 120-foot-tall poles monitored

to collect wind speed, direction, and the dynamic response of each pole. Moreover, several retrofitting methods were performed to enhance aerodynamic damping. Among the retrofitting methods applied, a 16-foot-long perforated shroud was a successful method to prevent lock-in. The above studies highlight several issues with high-mast towers that may be mitigated by the use of direct embedment of the foundation. Base plate fatigue issues and the dynamic effects that drive the cyclic loading that causes fatigue may be mitigated through this construction technique. The reader is directed to the Phase 1 report for more information on these topics and others related to traditional high-mast tower foundations as well as direct embedment of pole structures.

Chapter 3 Design and Pole Installation

3.1 Test Pole Design

The design process of the embedment foundations was performed by following the LRFD design procedures mentioned in the *Drilled Shafts: Construction Procedures and Design Methods Manual* (Brown et al, 2018). The side resistance and base resistance were checked for all geomaterial layers through which the trial shaft extended. Moreover, the factored resistance and settlement check for each trial embedment length ensured it was safe, with a tolerable settlement of one inch assumed. LPILE was used for the pushover analysis, and the p-y method was used to check the minimum diameter and embedment length required for lateral loads. The trial design procedure, calculations, and findings are provided in Appendix A.

3.1.1 Soil Data

The soil data were determined by drilling a borehole. The borehole report in Figure 3.1 shows the types of soil observed from the ground surface to 25 feet below the ground surface. The sandy soil was noted to a depth of 22 feet, and then a two-foot layer of alluvium and a 1-foot layer of sandstone were observed. The soil classification, blows, and N-value are reported in Table 3.1. The soil data were used in the trial design of the embedment foundation and the LPILE analyses. Again, see Appendix A.

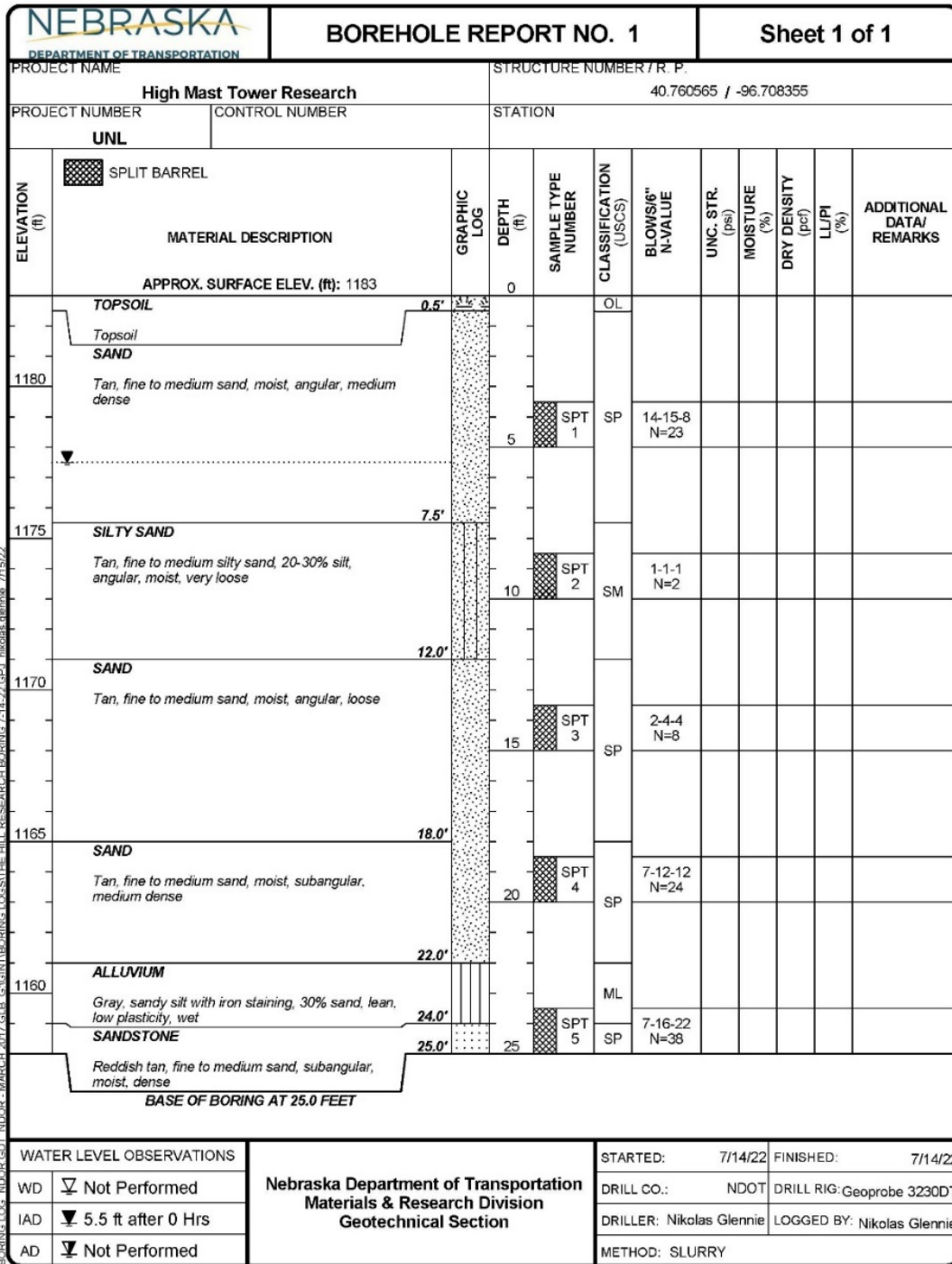


Figure 3.1 Borehole report

Table 3.1 Results of borehole report showing the soil layers with their properties

Soil Type	Layer thickness (ft)	Layer depth (ft)	Soil Classification	Blows/6''	N-Value
Topsoil	0.5	0.5	OL	-	-
Sand	7	7.5	SP	14-15-8	23
Silty Sand	4.5	12	SM	1-1-1	2
Sand	6	18	SP	2-4-4	8
Sand	4	22	SP	7-12-12	24
Alluvium	2	24	ML	-	-
Sandstone	1	25	SP	7-16-22	38

3.1.2 Pole Data

Four poles were studied and tested to evaluate the effect of embedment length and backfill material used. The poles had the same length of 60 feet and consisted of three discrete sections, as shown in Figure 3.2, each with a different thickness and diameter. The taper was 0.14 in/ft for all poles. The geometry of each pole is summarized in Table 3.2 and shown in Figure 3.3. Two lengths were investigated to study the effect of embedment length: 12 ft and 16 ft, and two backfill materials were investigated: concrete and gravel. The depth and type of backfill used for each pole are listed in Table 3.3.



Figure 3.2 Tested poles in the field before installation



Figure 3.3 Pole geometries

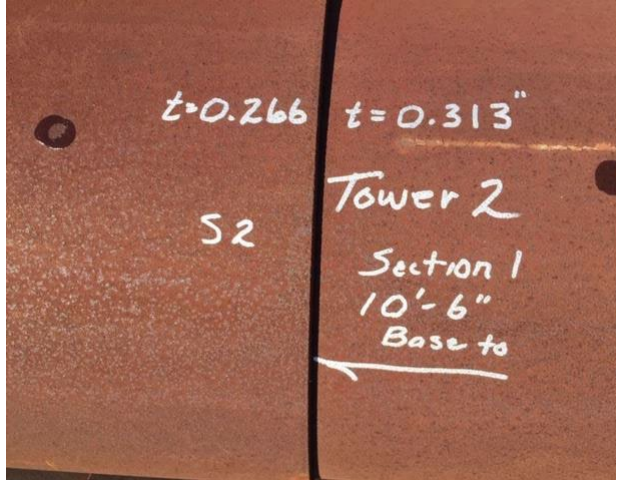


Figure 3.3 Pole geometries



Figure 3.3 Pole geometries



Figure 3.3 Pole geometries

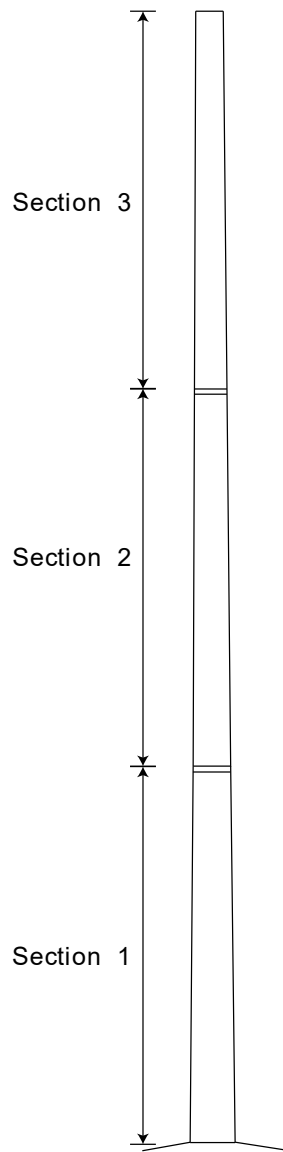


Figure 3.4 Poles geometry

Table 3.2 The geometry properties of each pole

Pole	Base Dia. (in)	Top Dia. (in)	Section 1		Section 2		Section 3	
			Length (ft)	Thickness (in)	Length (ft)	Thickness (in)	Length (ft)	Thickness (in)
16 – Concrete	18.9	11.25	20.41	0.267	29.83	0.260	10.16	0.185
16 – Gravel	21.13	13.75	10.5	0.313	30.33	0.260	20.41	0.267
12 – Concrete	18.9	11.25	20.33	0.280	29.75	0.260	10.5	0.183
12 – Gravel	17.48	10	10.5	0.256	30	0.250	20	0.183

Table 3.3 Embedment length and backfill material used for each pole

Pole	Embedment length (ft)	Backfill material
16 – Concrete	16	Concrete
16 – Gravel	16	Gravel
12 – Concrete	12	Concrete
12 – Gravel	12	Gravel

3.1.3 Design Assumptions and Plans

The foundation is designed to the new NDOT standard HMT with a height of 80 feet, a 22-inch base diameter, and a wall thickness of 0.375 inches. The poles are directly embedded in the foundation with concrete and gravel backfills, as shown in Figure 3.5 and Figure 3.6, respectively. The geotechnical design parameters and conditions were based on the borehole report. The subgrade consists of loose to medium-dense sand and silty sand extended from the ground surface to a depth of 24 feet. Boring was terminated in sandstone at a depth of 25 feet. The groundwater was encountered at 5.5 feet.

The drawing included the following language:

The directly embedded poles shall be erected plum; the center of the borehole shall be within ± 1 inch laterally and within ± 6 inches long longitudinally from the stacked survey hole. Thoroughly tamped by mechanical methods, the stone backfill from the dense base was used to properly set the elevation of the pole as illustrated in the drawings. The contractor may use temporary casing. The backfill material shall consist of a well-blended mixture of cohesionless material consisting of three parts of No. 2 crushed limestone and one part of No. 10 sand. All the material shall consist of sound natural material and crushed aggregates classified by aggregate size designation and ranges in the mechanical analysis per ASTM D 448-86. Alternate backfill gradations may be used with approval. Locally available materials and mixtures providing a recognized cost and performance can be considered. The maximum aggregate size should be less than 3 inches. A well-compacted and uniformly-dense blend must be obtainable considering the site conditions, backfill material, moisture content, and tamping equipment and procedures available. To obtain satisfactory compaction, the backfill material moisture content shall approach optimal, the optimal content shall be determined using ASTM D 698-91, and the state of compaction shall be evaluated using ASTM D-4253-93.

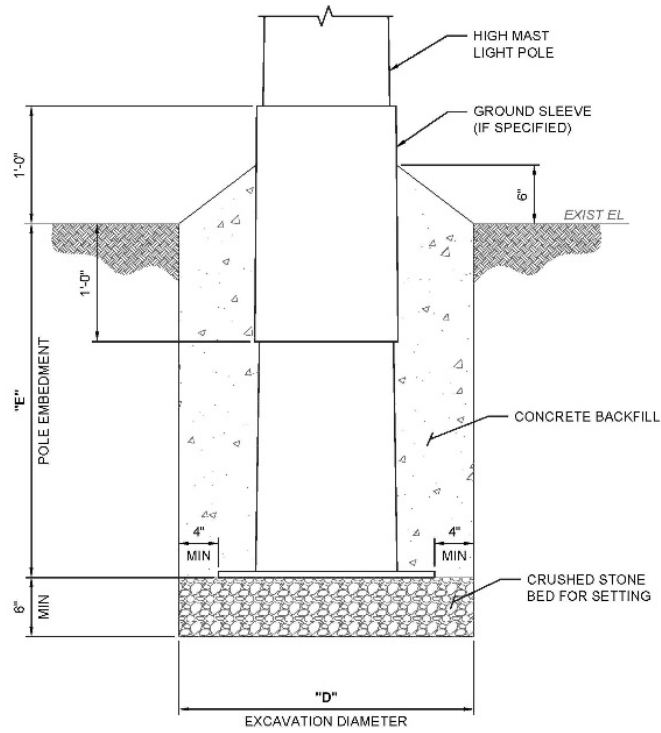


Figure 3.5 Section for directly embedded foundations of poles with concrete backfill

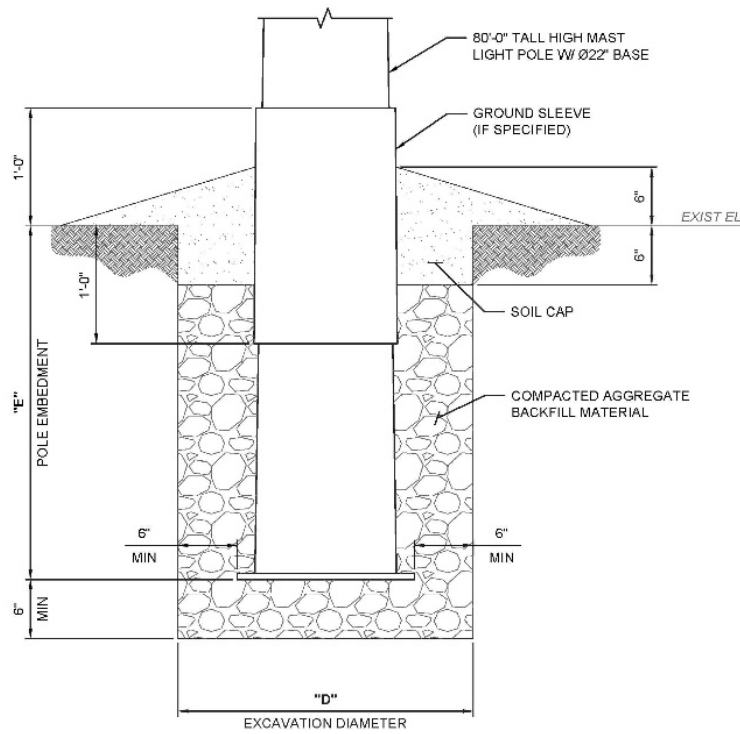


Figure 3.6 Section in directly embedded foundations of poles with gravel backfill

3.2 Design Procedure

For preliminary design, Broms' method may be used; see Section 13 of the AASHTO LTS-LRFD. Here, the soil unit weight, angle of internal friction, and passive soil coefficient are required based on estimates and/or the geotechnical report. The pole shaft diameter may include the concrete backfill or the average diameter of the pole shaft and the drilled shaft for gravel fill. (ASCE/SEI 72-21). However, a detailed process is recommended for strength and translation checks. Section 13 suggests that the first 1.5 diameters of soil depth be neglected in the analysis; however, if the frost depth is lower, the frost depth should conservatively be used.

The detailed design process is demonstrated in Appendices A and E. Appendix G provides computations demonstrating that the Service I limit state will not control the shaft design. This limits the pole tip translation to ten percent of the height, in the case of NDOT's standard 80-ft pole, 8 ft.

The first step is to determine the soil properties from the field; this includes the geomaterial layer thickness and type, unit weight, and field N-value for each soil layer. The factored load demands were then summarized to compare to the factored load resistance. The factored loads are determined from the structural design.

The second step is calculating the nominal and factored side resistance for all the geomaterial layers through which the trial shaft extends. Then, the factored base resistance was calculated for each layer, and the factored resistance was determined for the trial embedment depth and compared to the axial load demand. Unlike bridge foundations, axial loads for LTS are small; this step seldom controls the design.

The next step is to perform a settlement check that evaluates the resistance corresponding to downward translation and compared it to the axial load demand. If the resistance is less than the axial load demand, then a higher trial depth is recommended. Again, this check is unlikely to control the design for high-mast poles.

The next step is to perform a pushover analysis using LPILE, where the backfill material and hole diameter are assumed. Based on testing and the recommendations in ASCE 72-21, the concrete backfill is considered fully effective, i.e., the diameter for analysis is the diameter of the shaft. The pole's strength should not be an issue. For gravel backfill, the average shaft and pole diameters may be used. As discussed below, the shaft diameter provides good agreement; however, this is based on our limited testing. This step included applying the demand load in several increments and computing the corresponding translation. Then the relation between the load increment and translation is plotted. If a nonlinear behavior trend is observed suggesting the onset of instability against overturning, then it is recommended to use another trial embedment depth. Moreover, the bending moment and shear load diagrams were obtained from LPILE to determine the maximum load effects. The groundline translation was computed with LPILE and compared to acceptable service and extreme-load levels. Based on the robust performance demonstrated by the testing, and judgment, a groundline translation limit for the Extreme I loading could be set at 0.75 inches. When reading the following sections, consider this limit when reviewing the test data, this is ultimately an NDOT judgment.

3.3 Installation

A local contractor installed the poles in two days. On the first day, the poles with concrete backfill were installed, and on the second day, the poles with gravel backfill were installed. First,

four holes with a diameter of 36 inches and a depth of either 12 or 16 feet were excavated with an Auger Drive Digger as shown in Figure 3.7. The distance between the holes was approximately 20 feet. To increase the mass of the 60-foot pole so that the first mode shape occurred at a frequency of 1.18 Hz, concrete donuts with different diameters and thicknesses were cast in the lab and moved to the site before the installation as shown in Figure 3.8. The weight of the donuts was determined using finite element software while considering the soil's properties and the geometry of each pole so that the first mode shape occurred at 1.18 Hz, which approximates the NDOT standard pole. These concrete donuts were installed on the poles as shown in Figure 3.8.

Then a 2-ft by 2-ft steel plate with a thickness of 0.5 inches was welded at the top of each pole. This steel plate was to receive the shaking device required for the dynamic test and fix it to the steel plate by four holes each with a diameter of 0.375 inches, as shown in Figure 3.8. After placing all the attachments, each tested pole was erected by a crane as shown in Figure 3.9, positioned near the top of the hole to attach the inclinometer casing. The inclinometer casings were attached before placing the backfill material, as shown in Figure 3.10. This helped to place the inclinometer in the casing during the static tests and remove it after finishing the tests. Later the pole was placed in the hole vertically and was supported by the crane during the entire installation process, as shown in Figure 3.11. After the pole was placed vertically and centered inside the hole to the required depth, a magnetic torpedo level was used to ensure that the pole was properly plumbed. Lumber was also used to help keep the pole at the center of the hole while placing the backfill.

For the concrete backfill, a compressive design strength of 4000 psi was placed in the hole and its important to mention that the concrete mixed design was not a part of the appendix. An electric concrete vibrator was used to help consolidate the freshly poured concrete, and proper compaction was achieved, as shown in Figure 3.12. Moreover, it helped to ensure uniform distribution of the aggregate and cement paste, which provides consistent quality and strength. The exposed concrete was finished to provide a uniform and sloping surface for drainage. For the gravel backfill, the gravel was placed in incremental lifts and thoroughly tamped using a mechanical tamper, as shown in Figure 3.13. Six-inch lifts were used and uniformly compacted around the annulus. A soil cap consisting of native clay soil or a predominantly cohesive soil mixture is recommended to sufficiently cover the compacted backfill gravel. The soil cap is sloped from the pole in all directions, as shown in Figure 3.5.



Figure 3.7 Auger Drive Digger used to excavate the holes



Figure 3.8 Installing the concrete donuts and welding the steel plates to the top of the poles



Figure 3.9 Lifting the pole using a crane and placing it inside the hole



Figure 3.10 Process of attaching the inclinometer casing to the pole



Figure 3.11 Installing the pole vertically in the pole and make sure it is installed at the center



Figure 3.12 Placing the concrete backfill and using an electric vibrator to ensure proper compaction



Figure 3.13 Placing the gravel backfill and using an electric tamper to ensure uniformly compacted around the annulus



Figure 3.14 Poles in the field at the end of the installation process

Chapter 4 Field Evaluation Tests

4.1 Instrumentation

The following sections describe the equipment, sensors, and instrumentation plans used for static and dynamic tests.

4.1.1 Static Test

The Vertical In-Place Incliner System Model 6180 from GEOKON shown in Figure 4.1 was used to determine the inclination of the pole foundation during the static test. It consisted of four segments, each with a length of five feet, that were interconnected using in-line ball joints and spring-loaded wheel assemblies to allow them to positively engage in the grooves of the inclinometer casing. The sensors are connected by a wire bus cable and connected to a Campbell Scientific Datalogger, which monitors data collection. Quick-Lock Incliner Casings from GEOKON were attached to each pole during the installation as mentioned previously. The layout of the casing and inclinometer for each embedment length is shown in Figure 4.2. For the 12-ft embedment depth, Array-1 and 3 ft of Array-2 were above the ground surface during the test, while for the 16-ft embedment length, only 4 ft of Array-1 was above the ground surface.



Figure 4.1 The Vertical In-Place Incliner System Model 6180

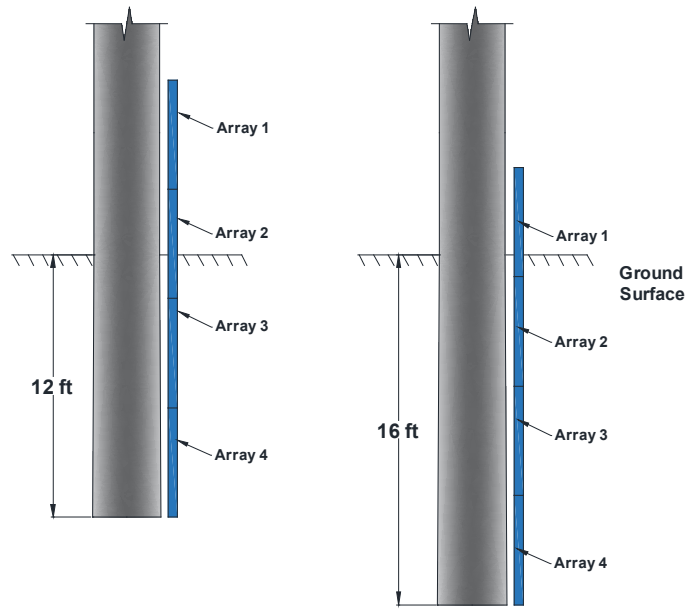


Figure 4.2 Layout of the casing and inclinometer for each embedment length

A tension S beam load cell with a capacity of 10 kips was used to measure the applied load at the top of the pole as shown in Figure 4.3. Two spherical ties were installed so that the load cell could be attached to the pulling setup. A string potentiometer, shown in Figure 4.4, was used to measure the transverse deflection near the ground surface. The load cell and the string potentiometer were connected to the STS404 Wireless Intelliducer Node, a rugged 4-channel wireless data acquisition device as shown in Figure 4.5. These nodes collect the data from the sensors and transform it into the STS4 Wireless Base Station shown in Figure 4.6, which transfers the collected data from all the nodes to the portable computer (PC).



Figure 4.3 Tension S beam load cell with a capacity of 10 kips used in the static tests



Figure 4.4 String potentiometer used to measure the transverse translation near the ground surface



Figure 4.5 STS404 Wireless Intelliducer Node



Figure 4.6 STS4 Wireless Base Station

The static test was performed by pulling a 100-foot steel cable attached to the tension load cell through a shackle at the top of the pole, as shown in Figure 4.7. Another shackle was used to connect the load cell with the person lift, as shown in Figure 4.8. To measure the deformation of the pole at the base during the test, the string potentiometer was fixed to the ground and attached to the base, as shown in Figure 4.9. The load cell and the string potentiometer were connected to

STS nodes, transferring the data into the STS database. Once the test started, the person lift moved away from the pole, causing it to pull the pole in the direction of movement until the person lift could not move anymore. The load and the base deformation were recorded during the test. Each pole was subjected to three static tests in two opposite directions, as shown in Figure 4.10.



Figure 4.7 Steel cable connected to the top of the pole for static and pluck tests



Figure 4.8 Pull setup for static and pluck tests



Figure 4.9 Measuring the transverse translation near the ground surface using a string potentiometer for static tests



Figure 4.10 Static test (one direction)

4.1.2 Dynamic Tests

Two dynamic tests were performed, the pluck test and the force vibration test, to measure the damping ratio and the natural frequencies of the first three mode shapes. Each pole was subjected to three pluck tests and one forced vibration test in opposite directions.

4.1.2.1 Protocol and Equipment for Pluck Test

To determine the damping ratio for each pole and to check the effect of using different embedment lengths and backfill materials, all the poles were subjected to three pluck tests in two opposite directions. The test configuration was the same as the static test, but the person-lift moved until the applied load at the top of each pole was 2 to 3 kips. Seven accelerometers were installed along the length of the poles before testing to capture the free vibration response of the pole, as shown in Figure 4.11. The locations were determined using finite element software, taking into consideration the pole geometry and soil characteristics to capture the first three mode shapes. These locations are shown in Figure 4.12 for 12- and 16-foot embedment lengths. The accelerometers were connected to the BDI nodes mentioned previously, which were connected to the BDI base station to collect and transfer the data to the PC. After installing the accelerometers and attaching the steel cable at the top of the pole, the person lift moved until the applied load reached the desired value, and then the “sea catch” was opened releasing the cable causing the pole to freely vibrate. The accelerometers recorded the accelerations.



Figure 4.11 Accelerometers used to measure the acceleration at different locations during dynamic tests

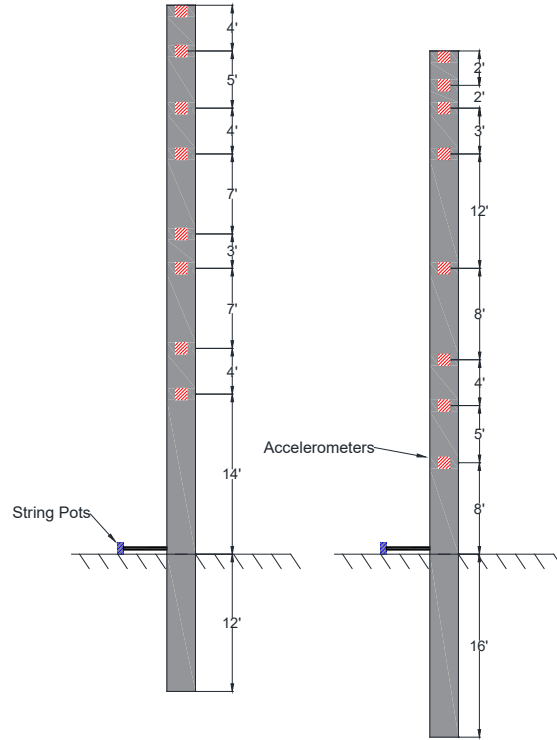


Figure 4.12 Locations of accelerometers installed for the dynamic tests for 12- and 16-ft direct embedments



Figure 4.13 Pluck test before release

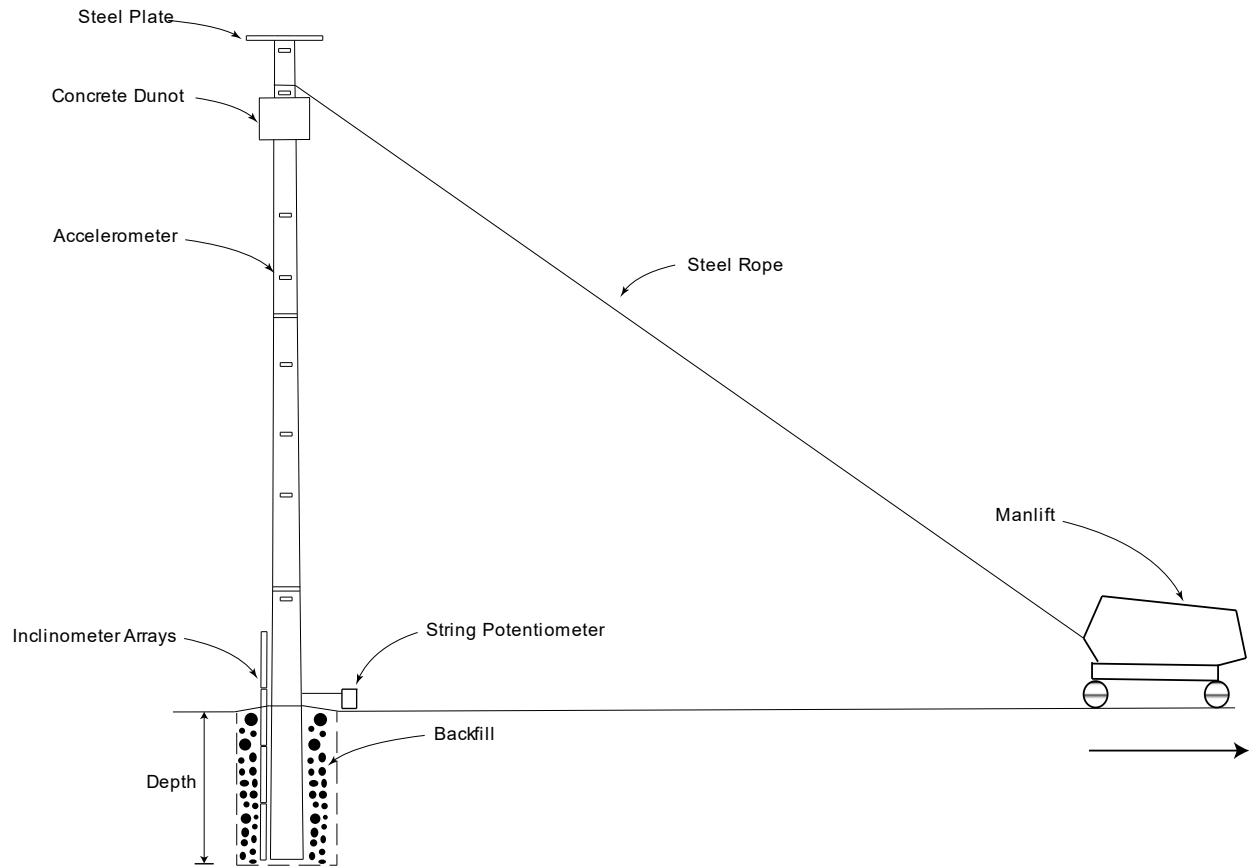


Figure 4.14 Static test and pluck test setup

4.1.2.2 Protocol and Equipment for Forced-Vibration Test

The second dynamic test was the forced-vibration test. The primary purpose was to measure the natural frequencies for the first three mode shapes. An APS 400 Electro-SEIS shaker, shown in Figure 4.15, was used to shake the poles near their natural frequency. Before each test, the shaker was placed on the steel plate at the top of the pole. Four vibration-damping spacers were inserted below the shaker to adjust the bands. Four screws were used to fix the shaker to the steel table; these screws went through the openings of the steel plate to the shaker. C clamps provided more resistance to prevent the shaker from sliding off the steel plate during testing, as shown in Figure 4.16. The shaker was placed in a free armature, fixed body mode with light bands, and connected to the APS 145 power amplifier shown in Figure 4.17. A signal generator was connected to the power amplifier to control the wave shape, frequency, and amplitude. A sine wave was generated during the test with a frequency ranging from 0.5 Hz to 50 Hz and increased slowly, especially around the natural frequencies. The BDI accelerometers, shown in Figure 4.18, were installed at specified locations mentioned in the pluck test. During the test, accelerations were recorded and used to determine the natural frequencies later.



Figure 4.15 APS 400 Electro-SEIS shaker used in the forced vibration test



Figure 4.16 Installation of the shaker at the top of each pole before the forced vibration test



Figure 4.17 The APS 145 power amplifier and the signal generator used in the forced vibration test



Figure 4.18 The installation of BDI accelerometers on the poles to measure the acceleration during forced vibration test

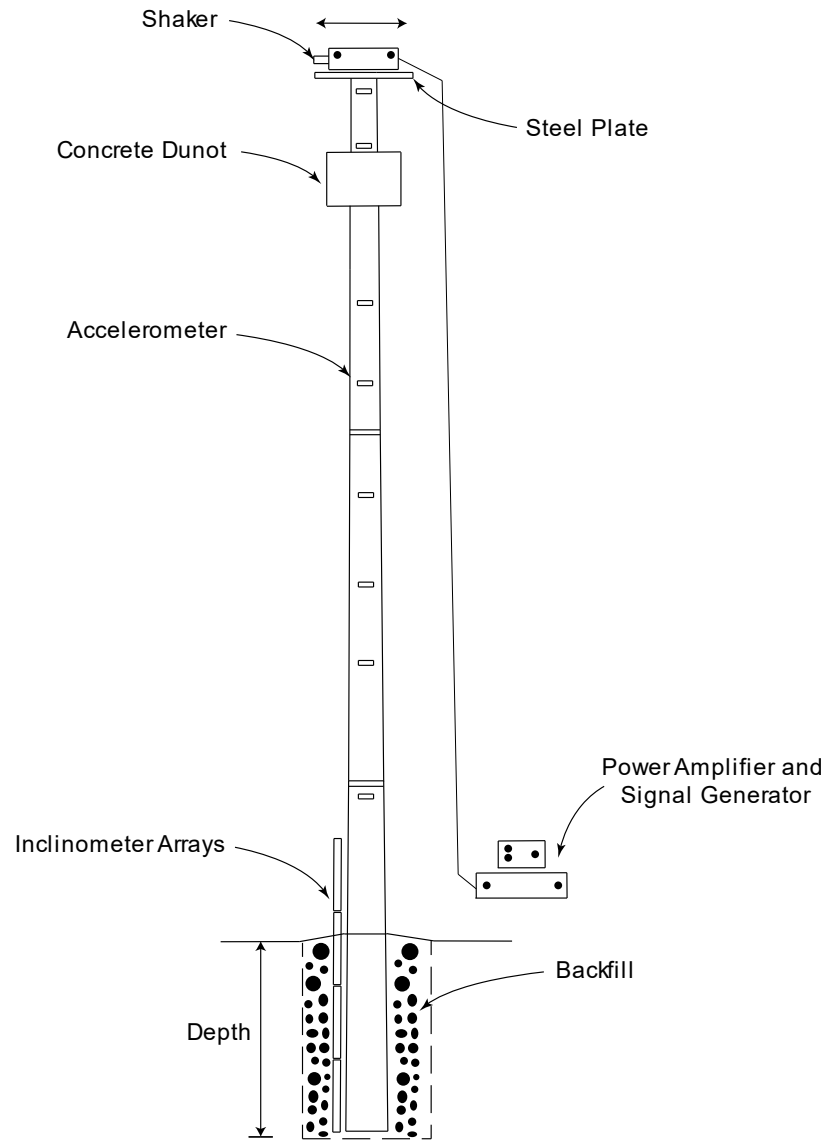


Figure 4.19 Forced-vibration test setup

4.2 Summary of All Experimental Tests Performed

Table 4.1 Summary of experimental tests performed showing the test number, test performed, direction, embedment length and backfill type

Test No.	Test	Direction	Embedment Length (ft)	Backfill
01-Pluck-NW-16-Concrete	Pluck	NW	16	Concrete
02-Pluck-NW-16-Concrete	Pluck	NW	16	Concrete
03-Pluck-NW-16-Concrete	Pluck	NW	16	Concrete
04-Static-NW-16-Concrete	Static	NW	16	Concrete
05-Static-NW-16-Concrete	Static	NW	16	Concrete
06-Static-NW-16-Concrete	Static	NW	16	Concrete
07-Dynamic-NW-16-Concrete	Vibration	NW	16	Concrete
08-Pluck-SW-16-Concrete	Pluck	SW	16	Concrete
09-Pluck-SW-16-Concrete	Pluck	SW	16	Concrete
10-Pluck-SW-16-Concrete	Pluck	SW	16	Concrete
11-Static-SW-16-Concrete	Static	SW	16	Concrete
12-Static-SW-16-Concrete	Static	SW	16	Concrete
13-Static-SW-16-Concrete	Static	SW	16	Concrete
14-Dynamic-SW-16-Concrete	Vibration	SW	16	Concrete
15-Pluck-NE-12-Concrete	Pluck	NE	12	Concrete
16-Pluck-NE-12-Concrete	Pluck	NE	12	Concrete
17-Pluck-NE-12-Concrete	Pluck	NE	12	Concrete
18-Static-NE-12-Concrete	Static	NE	12	Concrete
19-Static-NE-12-Concrete	Static	NE	12	Concrete
20-Static-NE-12-Concrete	Static	NE	12	Concrete
21-Dynamic-NE-12-Concrete	Vibration	NE	12	Concrete
22-Pluck-SW-12-Concrete	Pluck	SW	12	Concrete
23-Pluck-SW-12-Concrete	Pluck	SW	12	Concrete
24-Pluck-SW-12-Concrete	Pluck	SW	12	Concrete
25-Static-SW-12-Concrete	Static	SW	12	Concrete
26-Static-SW-12-Concrete	Static	SW	12	Concrete
27-Static-SW-12-Concrete	Static	SW	12	Concrete
28-Dynamic-SW-12-Concrete	Vibration	SW	12	Concrete

Table 4.1 Summary of experimental tests performed showing the test number, test performed, direction, embedment length and backfill type

Test No.	Test	Direction	Embedment Length (ft)	Backfill
29-Pluck-NE-16-Gravel	Pluck	NE	16	Gravel
30-Pluck-NE-16-Gravel	Pluck	NE	16	Gravel
31-Pluck-NE-16-Gravel	Pluck	NE	16	Gravel
32-Static-NE-16-Gravel	Static	NE	16	Gravel
33-Static-NE-16-Gravel	Static	NE	16	Gravel
34-Static-NE-16-Gravel	Static	NE	16	Gravel
35-Dynamic-NE-16-Gravel	Vibration	NE	16	Gravel
36-Pluck-SW-16-Gravel	Pluck	SW	16	Gravel
37-Pluck-SW-16-Gravel	Pluck	SW	16	Gravel
38-Pluck-SW-16-Gravel	Pluck	SW	16	Gravel
39-Static-SW-16-Gravel	Static	SW	16	Gravel
40-Static-SW-16-Gravel	Static	SW	16	Gravel
41-Static-SW-16-Gravel	Static	SW	16	Gravel
42-Dynamic-SW-16-Gravel	Vibration	SW	16	Gravel
43-Pluck-NE-12-Gravel	Pluck	NE	12	Gravel
44-Pluck-NE-12-Gravel	Pluck	NE	12	Gravel
45-Pluck-NE-12-Gravel	Pluck	NE	12	Gravel
46-Static-NE-12-Gravel	Static	NE	12	Gravel
47-Static-NE-12-Gravel	Static	NE	12	Gravel
48-Static-NE-12-Gravel	Static	NE	12	Gravel
49-Dynamic-NE-12-Gravel	Vibration	NE	12	Gravel
50-Pluck-SW-12-Gravel	Pluck	SW	12	Gravel
51-Pluck-SW-12-Gravel	Pluck	SW	12	Gravel
52-Pluck-SW-12-Gravel	Pluck	SW	12	Gravel
53-Static-SW-12-Gravel	Static	SW	12	Gravel
54-Static-SW-12-Gravel	Static	SW	12	Gravel
55-Static-SW-12-Gravel	Static	SW	12	Gravel
56-Dynamic-SW-12-Gravel	Vibration	SW	12	Gravel

Chapter 5 Analysis Methods

This chapter presents the methods used to analyze the results of static and dynamic tests. Moreover, it presents the LPILE analysis and finite element modeling of the poles using SAP2000™ (CSI, 2024).

5.1 p-y Analysis Description

LPILE was used to perform a p-y analysis that identified the soil-structure interaction and predicted the behavior of the soil under different loading conditions. This helped to understand how the soil deforms and interacts with the embedment foundation. Different cases were established considering embedment length, backfill type, and the medium around the foundation; these cases are shown in Table 5.1.

Table 5.1 Investigated cases using LPILE

Case	Embedment Depth, ft	Foundation Properties	Medium Around the Foundation
1	16	Round Shaft with Casing and Core/insert	Soil
2	12	Round Shaft with Casing and Core/insert	Soil
3	16	Steel Pipe Section	Soil
4	12	Steel Pipe Section	Soil
5	16	Steel Pipe Section	Gravel
6	12	Steel Pipe Section	Gravel

Case 1 and Case 2 simulated the pole foundation with concrete backfill. The casing's outside diameter was set to 36 inches with a 0-inch thickness, and it was assumed to be filled with concrete. The concrete compressive strength was 4000 psi, and it was not filled inside the core as the concrete did not go inside the pole. The core diameter and thickness were the diameter and thickness of the pole, respectively. For all cases, the part of the pole above the ground surface was simulated as a steel pipe section and assigned the pole's diameter, thickness, and elastic modulus, as shown in Figure 5.1. The elastic modulus was assumed to be 29000 ksi, while the yield stress was 50 ksi. Twenty sections were used to simulate the pole's taper, which is the maximum number of sections the LPILE can generate. Each section was three feet long, and the reduction rate in the diameter was 0.14 inches per foot.

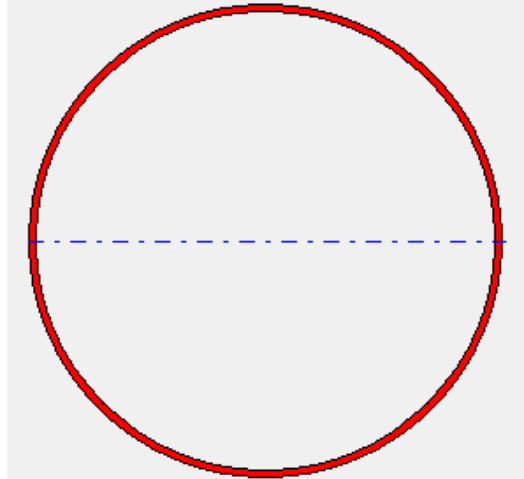


Figure 5.1 Steel pipe section used to model the part of the pole above the ground surface

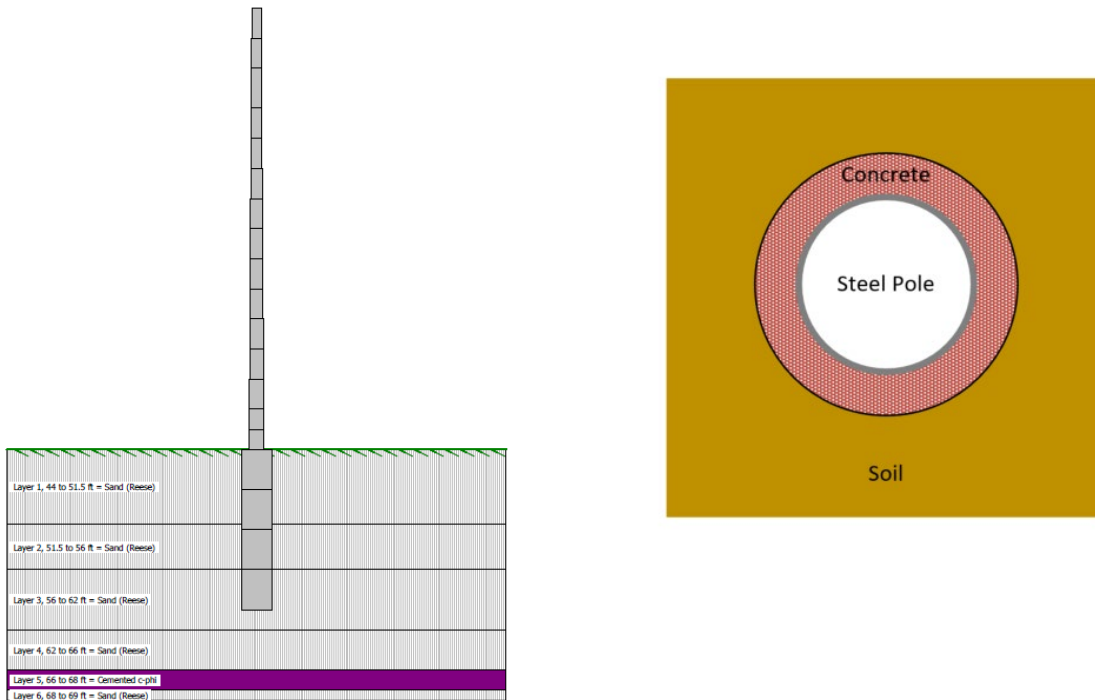


Figure 5.2 Case 1 – modeled in LPILE with a Round Shaft with casing and core/insert, and 16-ft embedment depth

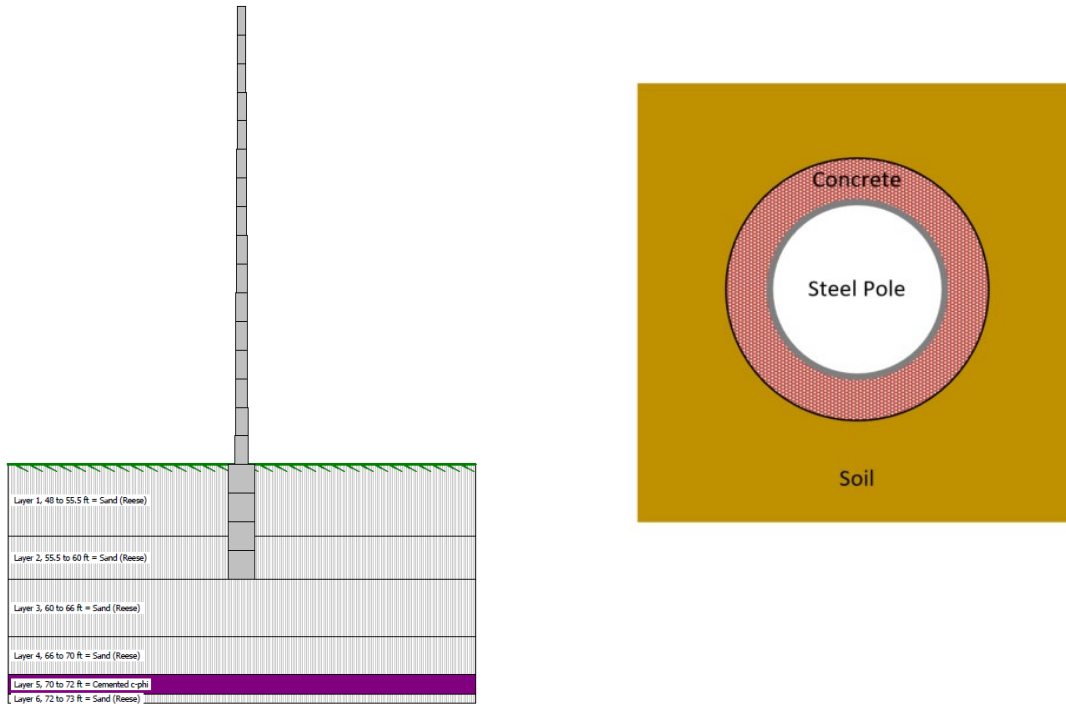


Figure 5.3 Case 2 – modeled in LPILE with Round Shaft with casing and core/insert, and 16-ft embedment depth

The LPILE cannot change the properties of the soil in the radial direction; thus, the pole with gravel backfill cannot be simulated directly. Because of that, two bounding cases were investigated for each pole with gravel backfill. Case 3 and Case 4 assumed the medium around the pole foundation was soil; alternatively, Case 5 and Case 6 assumed gravel. The LPILE cannot add gravel as the surrounding material, thus Strong Rock (Vuggy Limestone) was used as the surrounding medium to approximate gravel properties. For Cases 3 to 6, the foundation was assumed to be a steel pipe section with the same steel properties mentioned before.

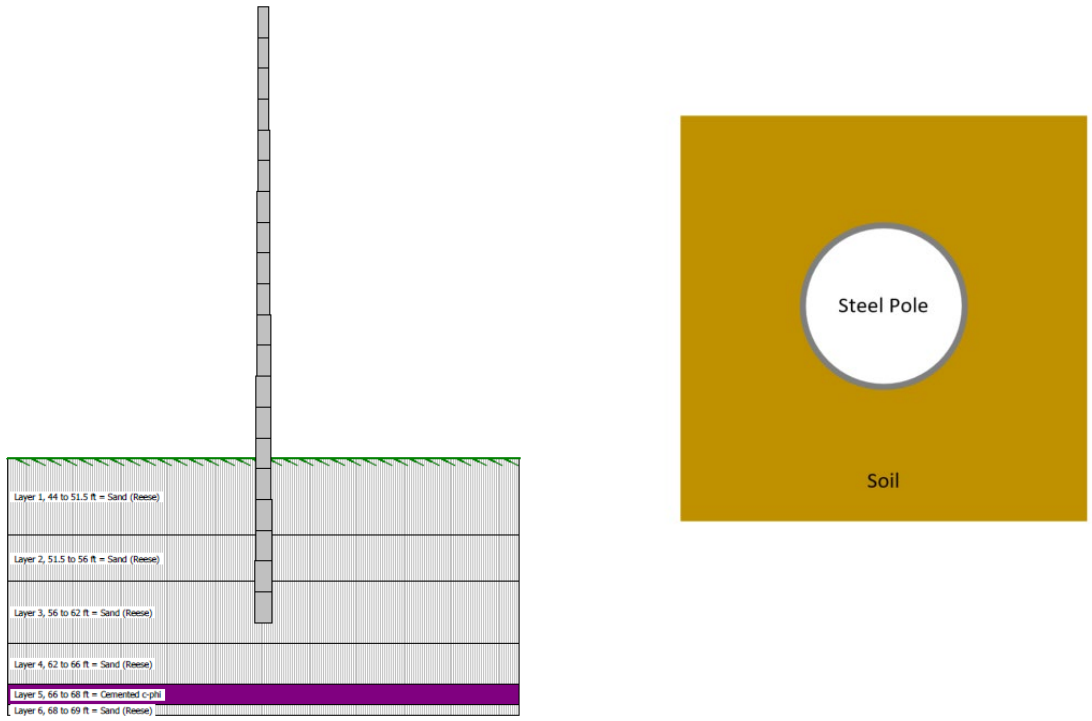


Figure 5.4 Case 3 – modeled in LPILE with steel pipe section and 16-ft embedment depth

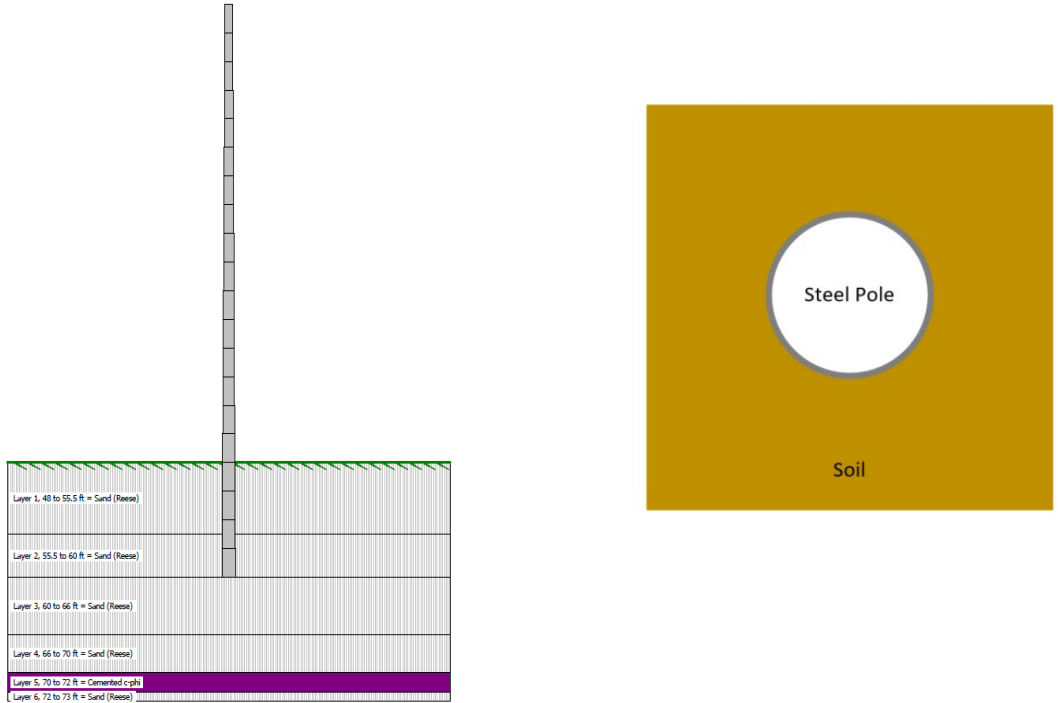


Figure 5.5 Case 4 – modeled in LPILE with steel pipe section and 12-ft embedment depth

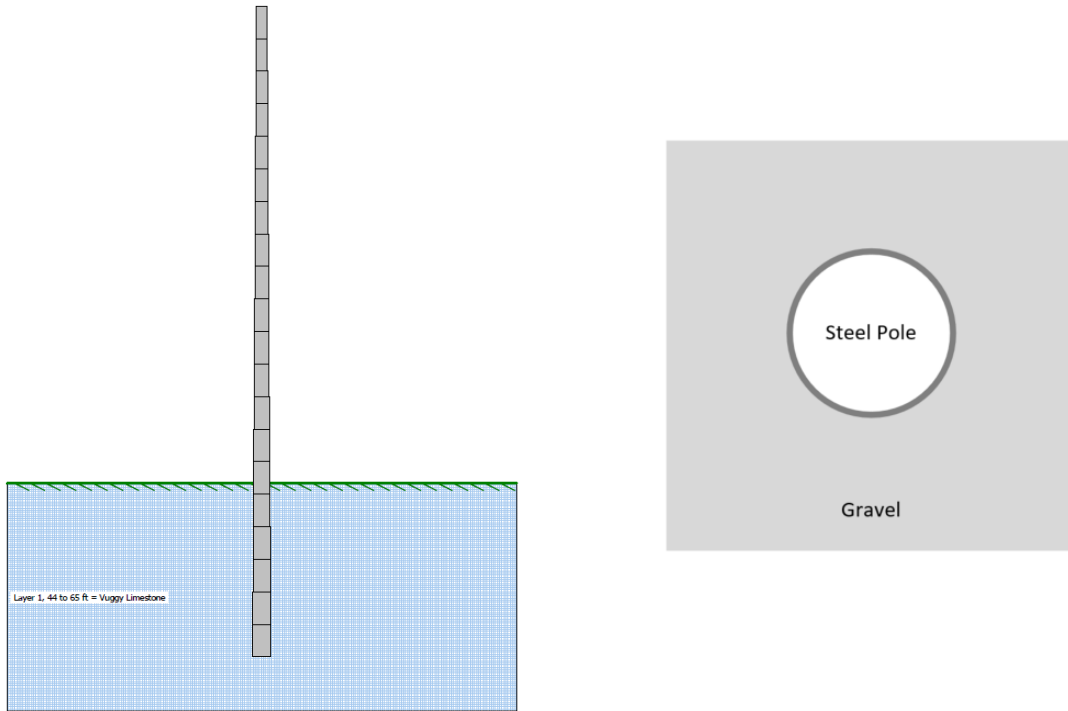


Figure 5.6 Case 5 – modeled in LPILE with steel pipe section, and 16-ft embedment depth surrounding with gravel medium

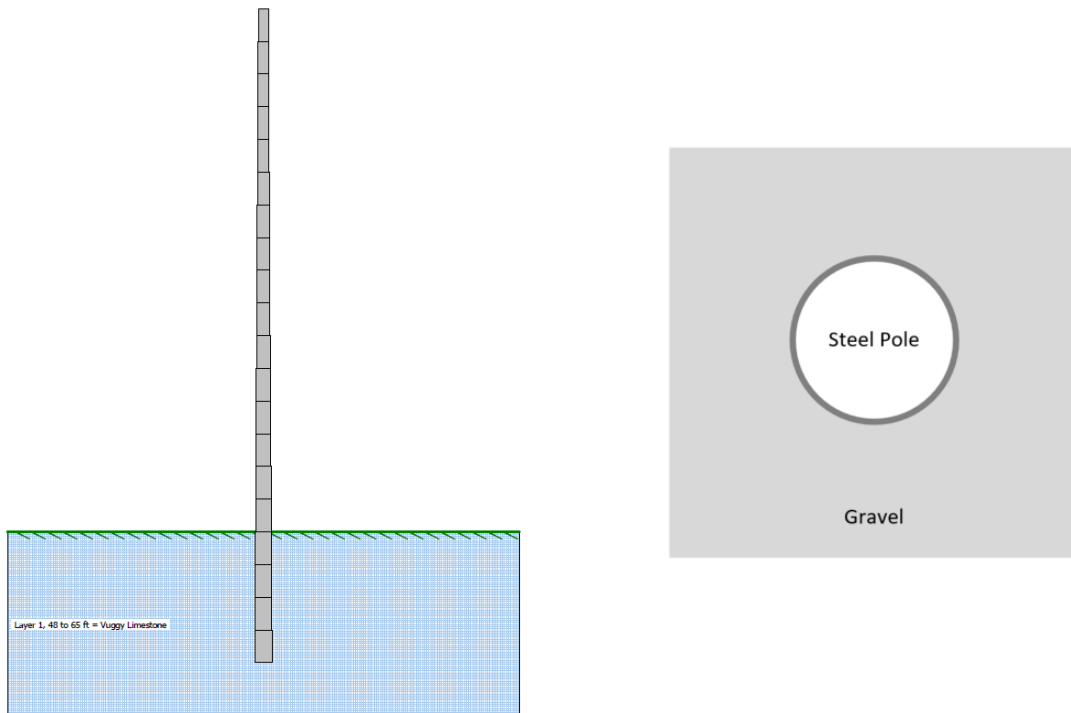


Figure 5.7 Case 6 – modeled in LPILE with steel pipe section, and 12-ft embedment depth surrounding with gravel medium

5.2 Frame Model

After performing the p-y analysis for each case and getting the load-translation curves for each depth at 1-ft increments, the SAP2000™ was used to create a finite element model for each case and determine the modal frequencies and the suggested locations for the accelerometers. The soil-structure interaction was simulated as a one-joint link element positioned at 1-foot intervals along the foundation. The link type was multilinear elastic and assigned nonlinear properties for the U2 and U3 directions (horizontal). The p-y curves obtained from LPILE were used to develop the finite element models for all cases.

To model Case 1 and Case 2, the section designer was used to create the foundation section. It consisted of a concrete annulus with a wall thickness of 8 inches and a diameter of 36 inches to simulate the diameter of the hole. Another annulus of steel was inside the concrete pipe, which assigned the thickness and diameter of the pole. The concrete compressive strength was 4000 psi, while the same properties of steel used in LPILE were used in SAP2000™. The modeled section is shown in Figure 5.8. A non-prismatic section was defined to consider the change in the pole diameter and thickness. The models for Cases 1 and 2 are shown in Figure 5.9.

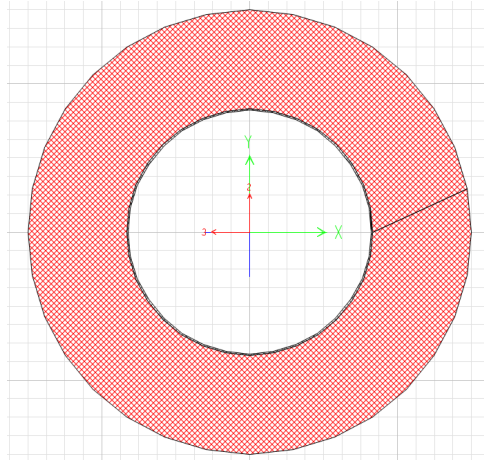


Figure 5.8 Modeled section in SAP2000™ for the foundation of Case 1 and Case 2

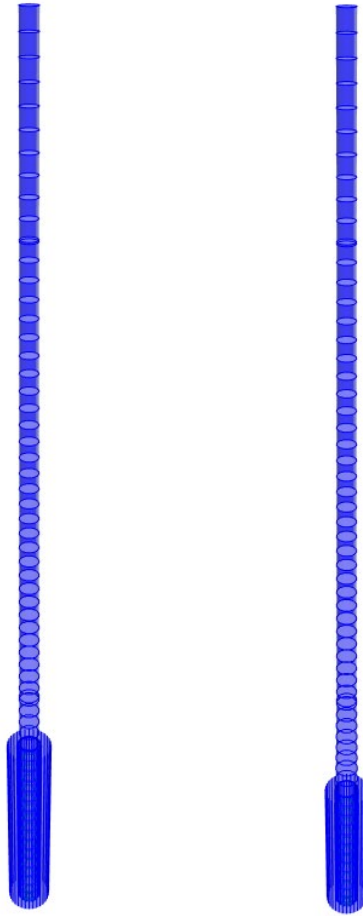


Figure 5.9 Models developed in SAP2000™ for Case 1 and Case 2

For Cases 3 through 6, the pole foundation was modeled as a steel pipe section, with a diameter and thickness assigned for each pole. Joint-link elements were spaced at 1-ft increments along the foundation with the p-y curves obtained from LPILE analysis. Similar to previous cases, a non-prismatic section was created for each case to consider the changes in the pole diameter and thickness. The finite element models are shown in Figure 5.10.

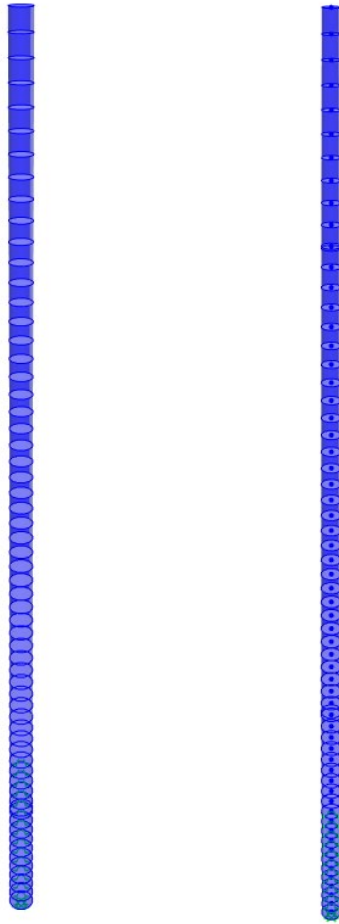


Figure 5.10 Models developed in SAP2000™ for Cases 3 through 6

5.3 Dynamic Analysis Methods

5.3.1 Log-Decrement Method

To calculate the damping ratios for each pole, three pluck tests were performed in each direction; thus, a total of six pluck tests were performed for each pole. The log-decrement method was used to determine the damping ratios, a measure of energy dissipation. The accelerometers measured the time-domain response after it had been pulled and released without any external disturbances and decayed following a sinusoidal waveform, as shown in Figure 5.11. The successive peaks of the vibration response were identified, and then the damping ratio was calculated using the below formula:

$$\zeta = \frac{1}{2\pi n} \ln \frac{u_i}{u_{i+n}} \quad (5.1)$$

where u_i is the acceleration at i^{th} cycle, u_{i+n} is the acceleration at $(i+n)^{\text{th}}$ cycle, and n is the number of cycles between the selected points.

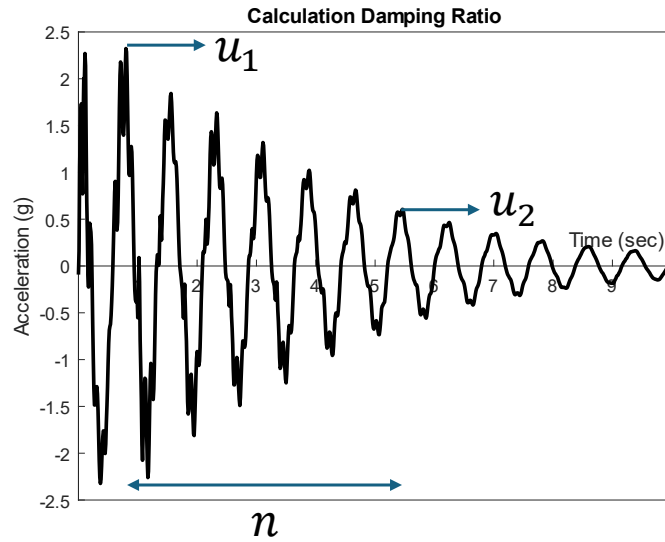


Figure 5.11 Illustration of a log-decrement method to calculate the damping ratio

5.3.2 Fast Fourier Transform

The Fast Fourier Transform method (FFT) was used to transform the data collected from the uniaxial accelerometers from the time domain into the frequency domain. This method allowed for the determination of the natural frequencies for each pole. The first three natural frequencies were computed, as shown in Appendix B.

5.3.3 Half-Power Bandwidth Method

Half-power bandwidth was used to calculate the damping ratios when the poles were subjected to force vibration tests. After transforming the collected data from uniaxial accelerometers from the time domain into the frequency domain and isolating each natural frequency, as shown in Figure 5.12, the point where the amplitude is reduced to the resonant amplitude was determined, and the damping ratio was calculated using the below formula:

$$\zeta = \frac{f_b - f_a}{2f_n} \quad (5.2)$$

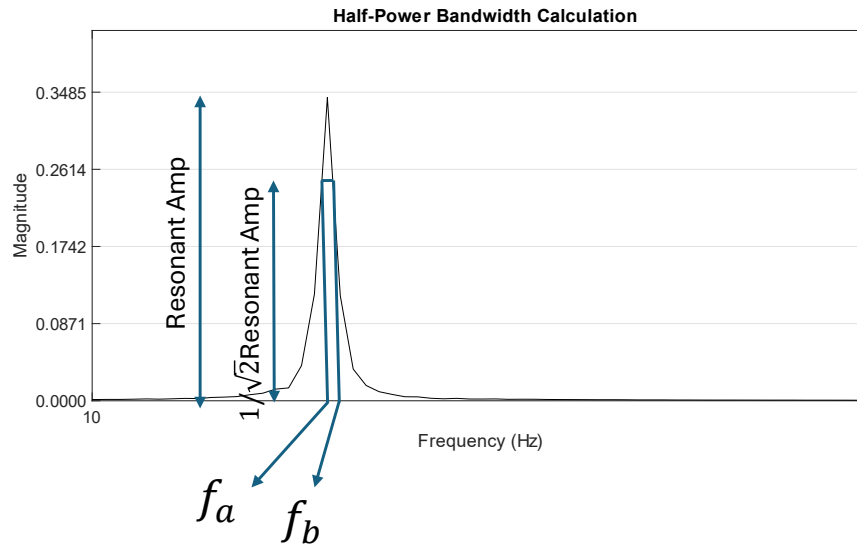


Figure 5.12 Illustration of half-power bandwidth method to calculate the damping ratio

Chapter 6 Experimental Results and Analysis

6.1 Static Test Results

6.1.1 Load versus Translation Results

Each pole was subjected to six static tests in two opposite directions to measure the response of the poles with different embedment depths and backfill materials. The load was measured using a tension load cell that was attached to the pulling setup, as mentioned before. In contrast, the translation was measured using a string potentiometer near the ground surface. The moment applied at the top of the foundation was calculated by multiplying the horizontal component of the applied force by the distance from the point of application to the ground surface. The responses are shown in Figure 6.1 to Figure 6.4. For each static test performed, the stiffness was calculated using the below formula:

$$k = \frac{P_{0.4\Delta}}{0.4\Delta} \quad (6.1)$$

where k is the stiffness of the pole (kip/inch), $P_{0.4\Delta}$ is the load at 0.4 of the maximum translation (kip), and 0.4Δ is 0.4 times the maximum translation that occurred. The stiffnesses calculated from all static tests are listed in Table 6.1.

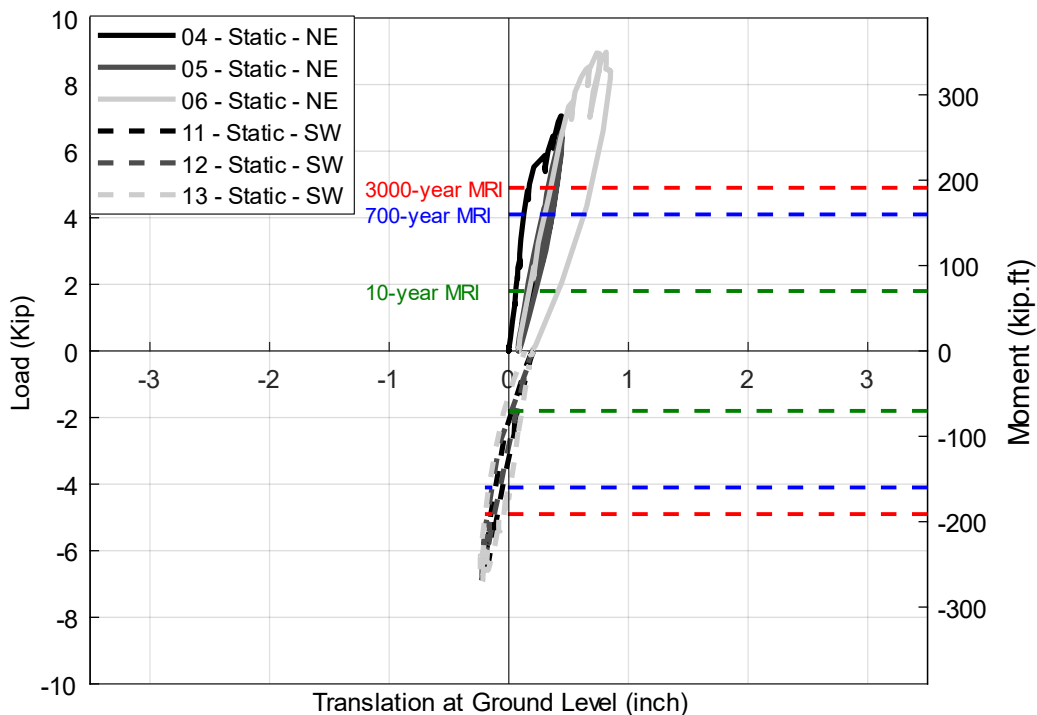


Figure 6.1 The load and moment vs translation at ground level of static tests performed on pole 16-Concrete

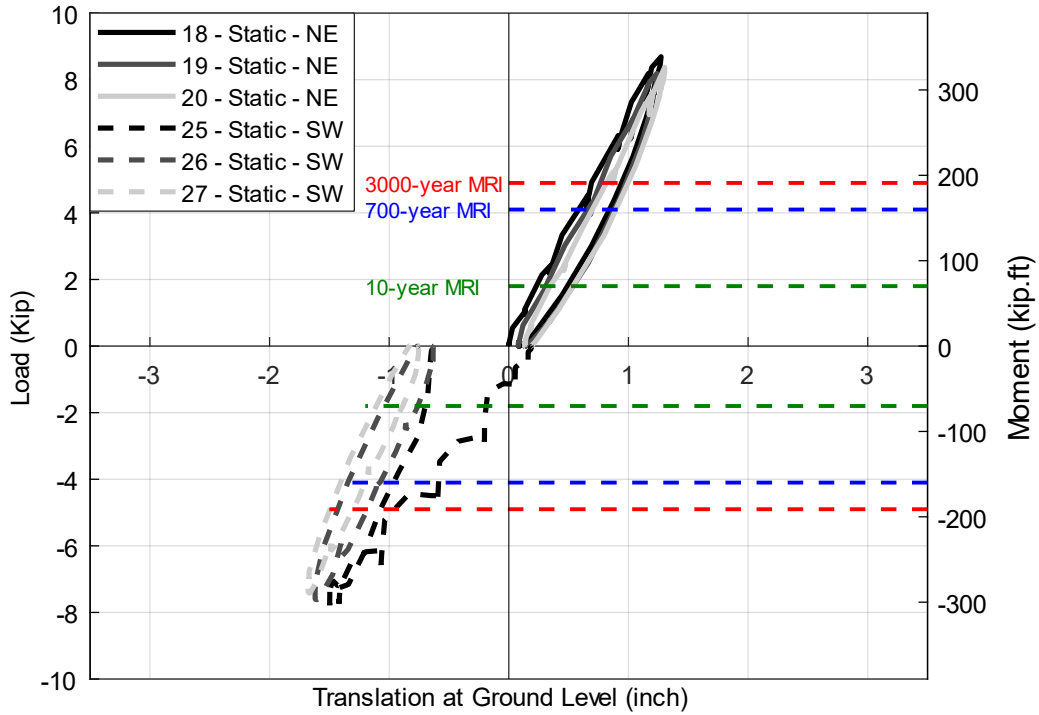


Figure 6.2 The load and moment vs translation at ground level of static tests performed on pole 16-Gravel

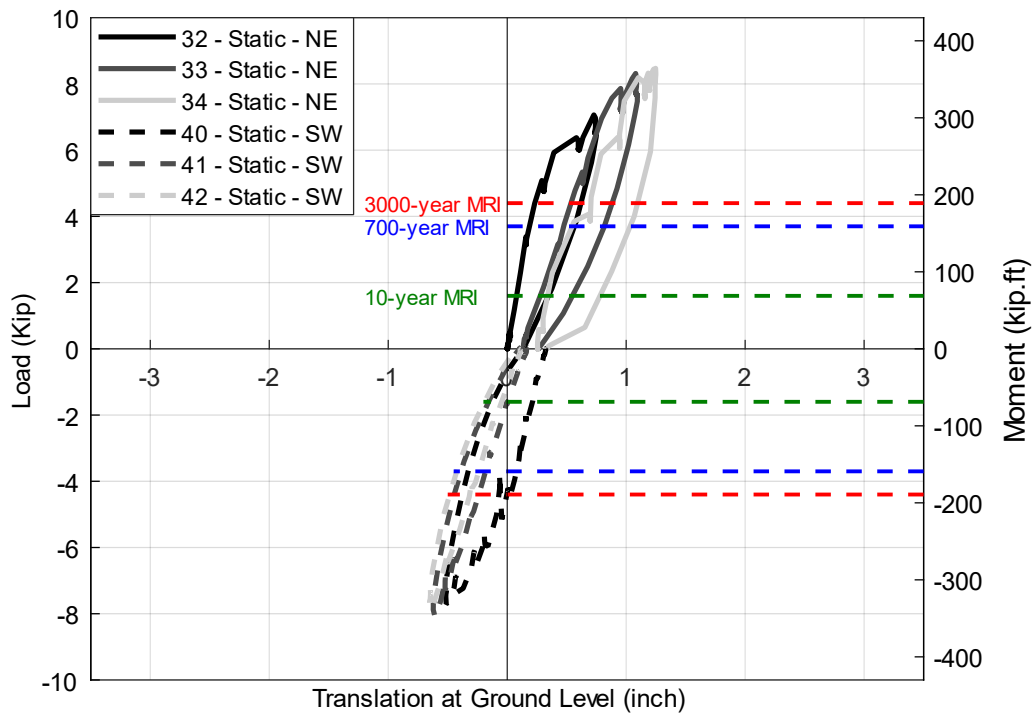


Figure 6.3 The load and moment vs translation at ground level of static tests performed on pole 12-Concrete

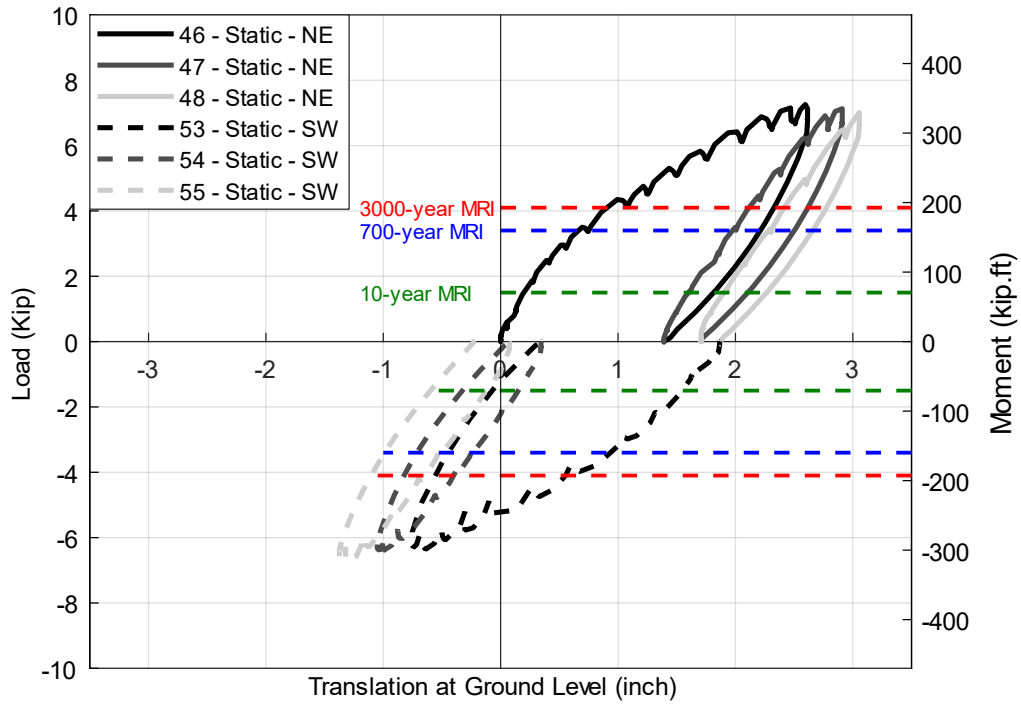


Figure 6.4 The load and moment vs translation at ground level of static tests performed on pole 12-Gravel

Table 6.1 Stiffness calculations for all static tests performed

Pole No.	Direction	Static Test No.	Load at 0.4Δ (lb)	0.4Δ (inch)	K (kip/inch)	K_{avg} (kip/inch)
16 – Concrete	NW	04	5179	0.18	29.13	23.34
		05	3241	0.15	22.13	
		06	5750	0.31	18.76	
	SE	11	3854	0.18	21.88	17.61
		12	2531	0.16	16.18	
		13	2505	0.17	14.76	
16 – Gravel	NE	18	3847	0.51	7.55	7.60
		19	3606	0.46	7.78	
		20	3488	0.47	7.45	
	SW	25	3068	0.67	4.55	8.03
		26	3827	0.39	9.70	
		27	3633	0.37	9.84	
12 – Concrete	NE	32	4942	0.30	16.51	12.62
		33	4249	0.38	11.10	
		34	4077	0.40	10.25	
	SW	39	4612	0.34	13.72	11.58
		40	3333	0.31	10.63	
		41	3171	0.31	10.39	
12 – Gravel	NE	46	4265	1.05	4.08	5.28
		47	3487	0.61	5.73	
		48	3260	0.54	6.05	
	SW	53	3738	1.05	3.57	5.10
		54	3252	0.56	5.83	
		55	3403	0.58	5.87	

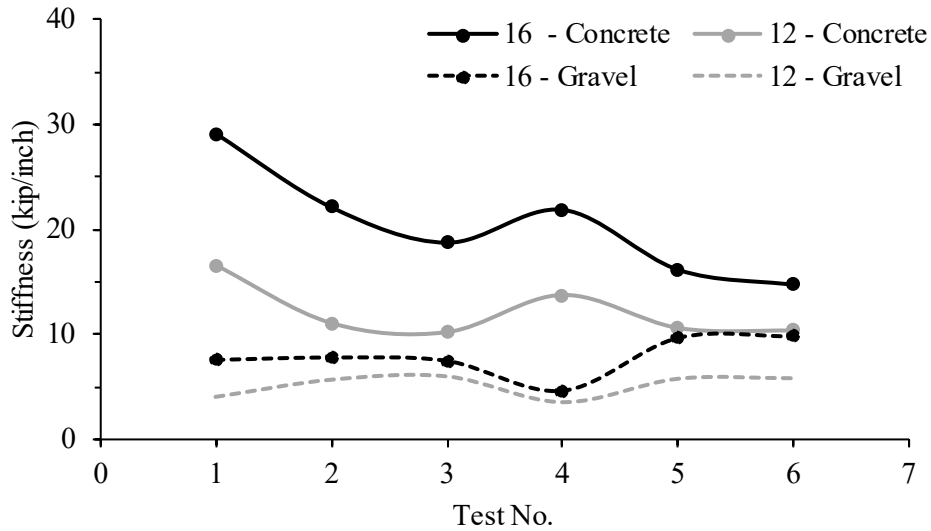


Figure 6.5 Reduction in stiffness for all poles as more static tests performed (tests 1-3 are pulled in one direction, and 4-6 are pulled in the opposite direction)

Load versus Translation Observations

- The results showed that poles with concrete backfill experienced a higher stiffness than poles with gravel backfill; the initial stiffness of 16–Concrete and 12–Concrete poles were almost four times higher than 16–Gravel and 12–Gravel poles, respectively.
- Poles with concrete backfill experienced a significant reduction in stiffness as more static tests were performed, as shown in Figure 6.5. The initial stiffness of the 16–Concrete pole decreased from 29.13 kip/inch to 18.76 kip/inch in the NW direction and from 21.90 to 14.76 kip/inch in the SE direction.
- The same behavior was observed for the 12–Concrete pole; the stiffness decreased from 16.51 to 10.25 kip/inch in the NE direction and from 13.72 to 10.39 kip/inch in the SW direction.

- For the 16–Gravel pole, the stiffness remains almost constant at around 7.50 kip/inch in the NE direction and does not follow a clear pattern in the other direction. The same behavior was observed on the 12–Gravel pole.
- In Figure 6.1, the shaft was loaded to approximately two times the 700-yr MRI design load to create a translation of about 0.3-0.4 in.
- Figure 6.2 also demonstrates consistent hysteric behavior with 700-yr MRI design load translations of about 0.75 inches.
- In Figure 6.2, when the direction of loading was reversed, a shift in translation was observed. This shift is due to large loads being applied in the first direction, the backside opens a void approximately equal to the translation toward the pull. Once this void closed, the hysteric behavior was stable.
- The stable observations indicate the possible self-healing behavior of the gravel backfill.
- In Figure 6.3, the 12-Concrete pole exhibited stable hysteretic behavior. The translations were approximately 0.5 in. at design loads.
- In Figure 6.4, the 12-Gravel illustrated the lowest stiffness, as expected. Interestingly, there is a large translation in the first cycle that then stabilizes. As noted above, this creates a void on the backside, which closes (a significant shift in the translation with load is reversed). Again, the hysteric behavior becomes stable with subsequent cycles. 12-Concrete is the least conservative case, and yet it demonstrated the toughness of these foundations. Practically, a significant wind in one direction might shift the pole; however, it could be re-backfilled during replumbing. Given the large loads applied in these tests, this occurrence is

expected to be infrequent. Also, note that should large-amplitude galloping events occur, effects can be mitigated with more damping, an extremely ductile load translation/rotation curve, and the possibility that the foundation acts as a fuse that can be repaired.

6.1.2 Rotation versus Depth and Loads Results

The rotation of the directly embedded foundation during the static test was measured using an inclinometer; the rotation of each inclinometer sensor vs. load and moment applied at the top of the directly embedded foundation is shown in Appendix C. These data are used to calculate the deflection of the foundation. Moreover, the inclination of the inclinometer vs depth of each static test at three levels of loading are shown in Appendix D. These data were used to determine the deflection profile during each static test.

6.1.3 Translation versus Depth Results

The translation profile for each static test was calculated from the rotation data obtained from the inclinometer sensors by multiplying the length of each sensor by the rotation. Then the translation was calculated by taking the sum of the translation of each sensor as follows:

$$\begin{aligned}
 D_1 &= L_1 \sin \theta_1 + L_2 \sin \theta_2 + L_3 \sin \theta_3 + L_4 \sin \theta_4 \\
 D_2 &= L_2 \sin \theta_2 + L_3 \sin \theta_3 + L_4 \sin \theta_4 \\
 D_3 &= L_3 \sin \theta_3 + L_4 \sin \theta_4 \\
 D_4 &= L_4 \sin \theta_4
 \end{aligned}
 \tag{6.2}$$

where D_i is the translation of the sensor i , L_i is the length of the sensors, which is five feet for all sensors, and θ_i is the rotation of the sensor i in radians. The translation profile for each static test at maximum load, 0.5 of the maximum load, and unloading is shown in Figure 6.6 to Figure 6.12.

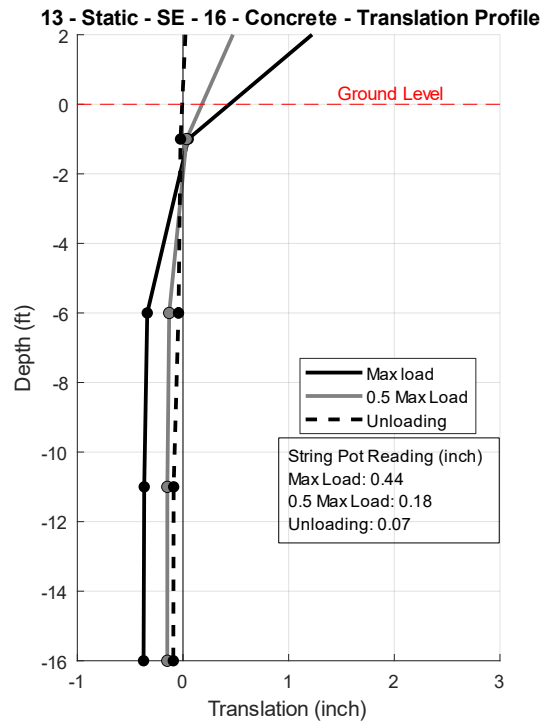
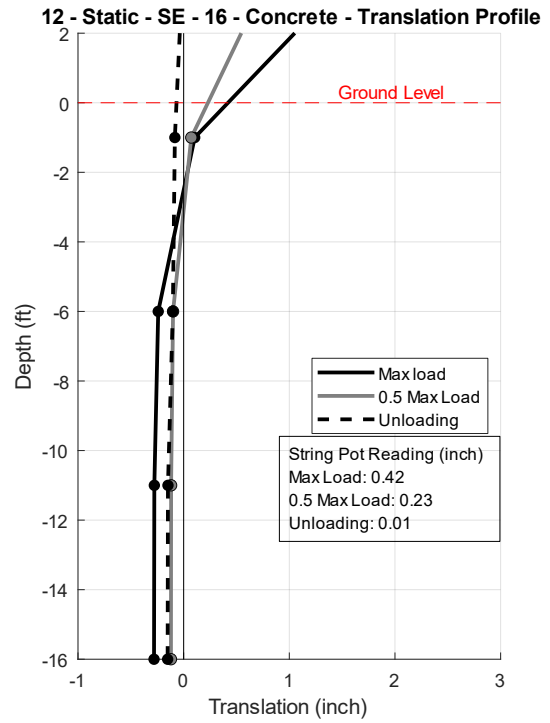
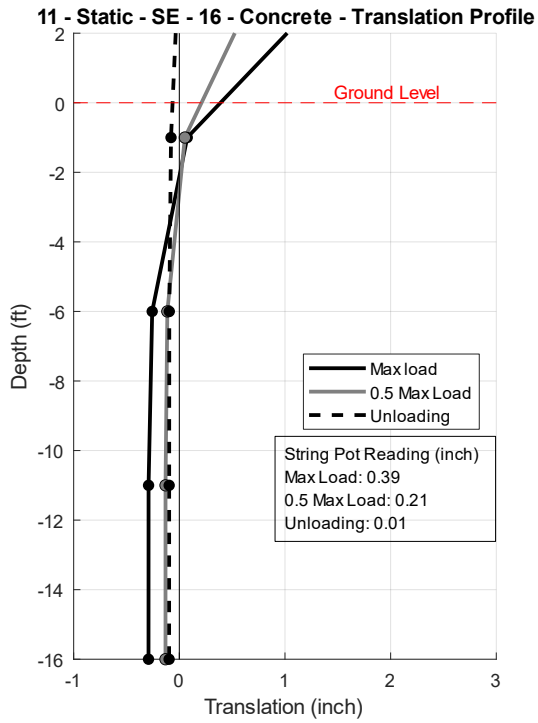


Figure 6.6 Translation vs depth of static tests on SE direction performed on pole 16 – Concrete, the 700-yr design load is approximately 0.5 of the maximum load

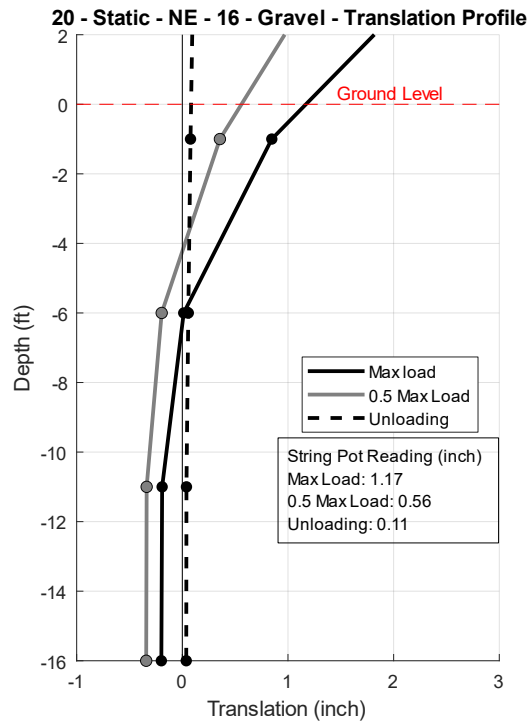
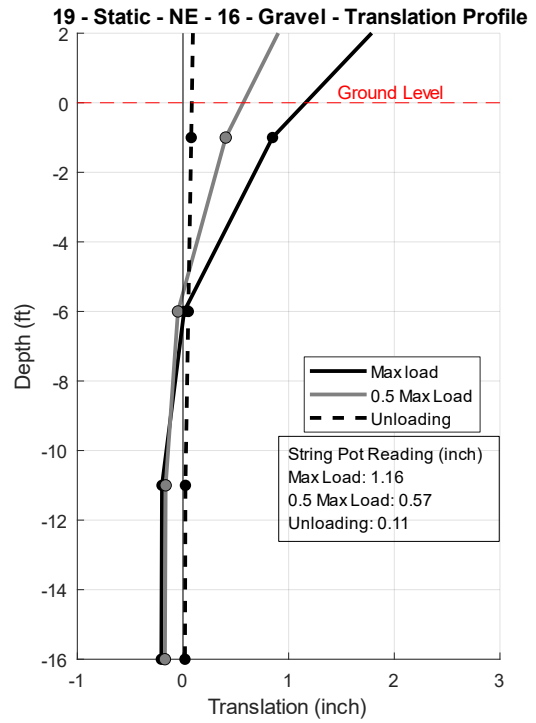
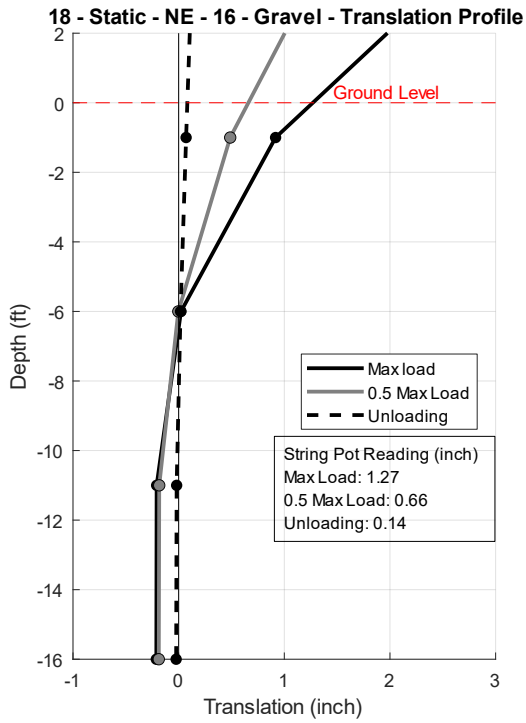


Figure 6.7 Translation vs depth of static tests on NE direction performed on pole 16 – Gravel, the 700-yr design load is approximately 0.5 of the maximum load

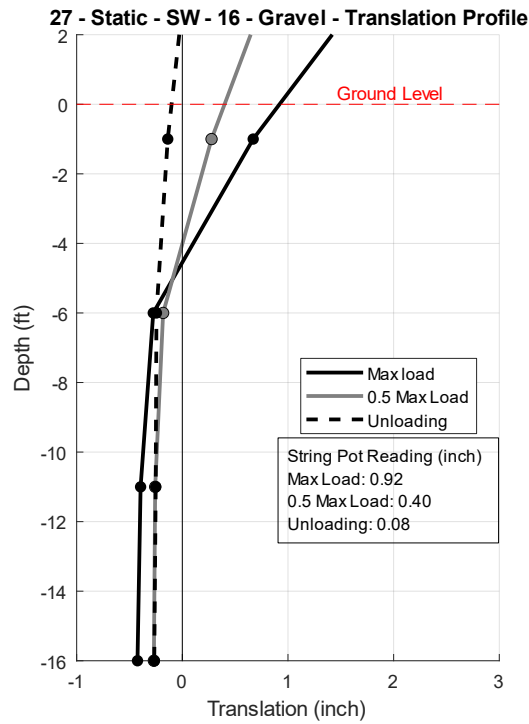
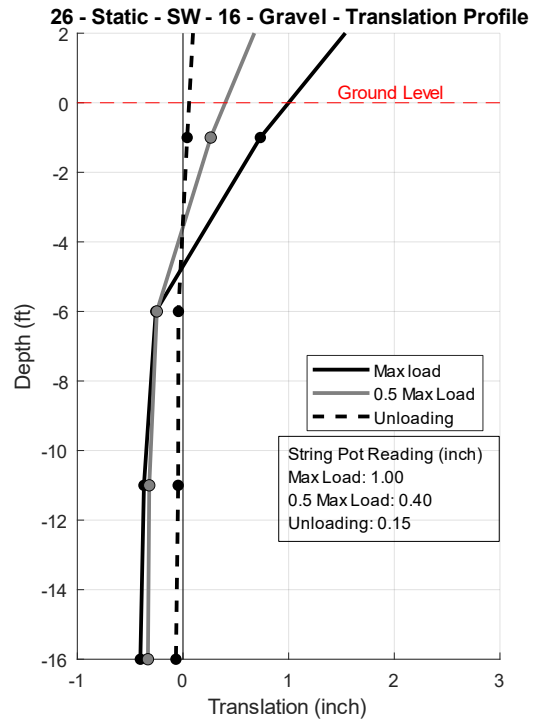
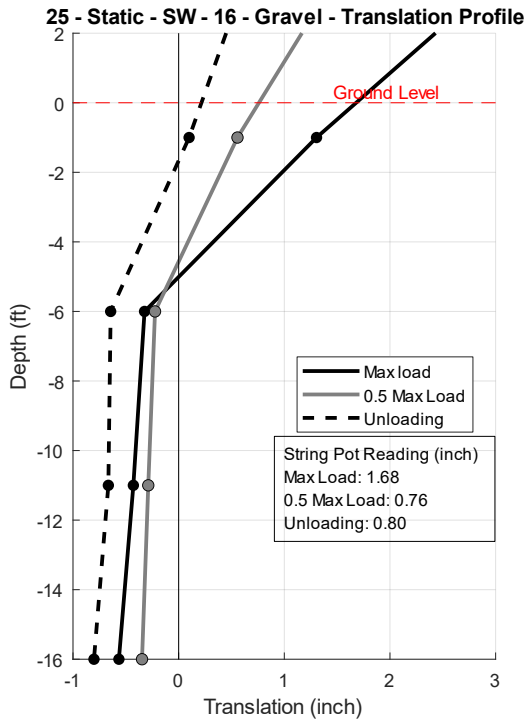
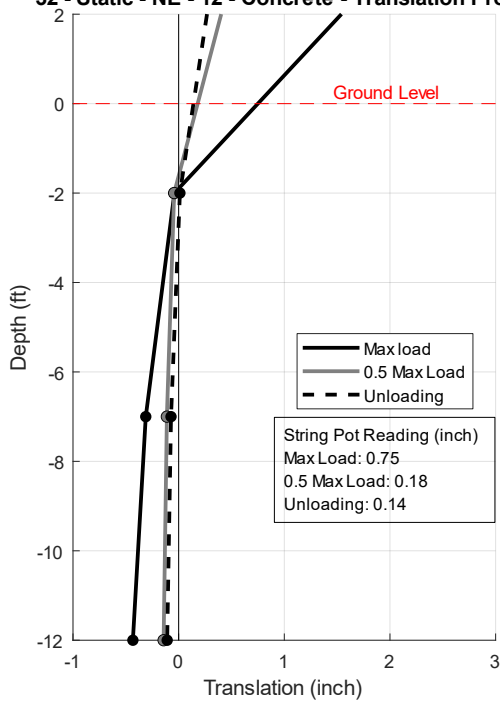
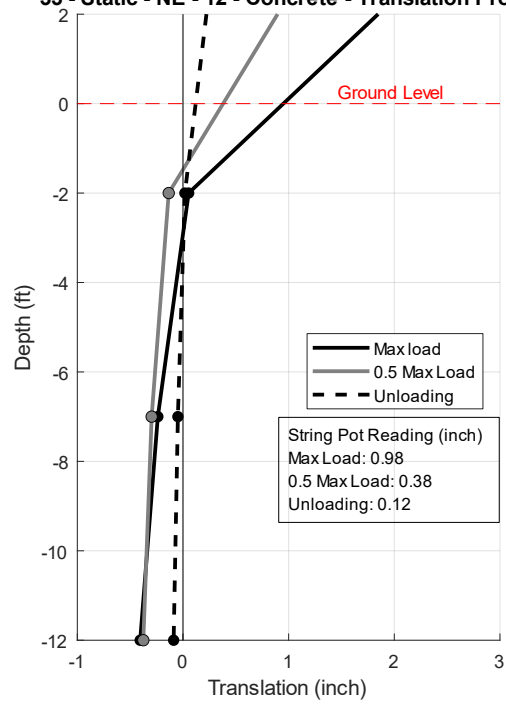


Figure 6.8 Translation vs depth of static tests on SW direction performed on pole 16–Gravel, the 700-yr design load is approximately 0.5 of the maximum load

32 - Static - NE - 12 - Concrete - Translation Profile



33 - Static - NE - 12 - Concrete - Translation Profile



34 - Static - NE - 12 - Concrete - Translation Profile

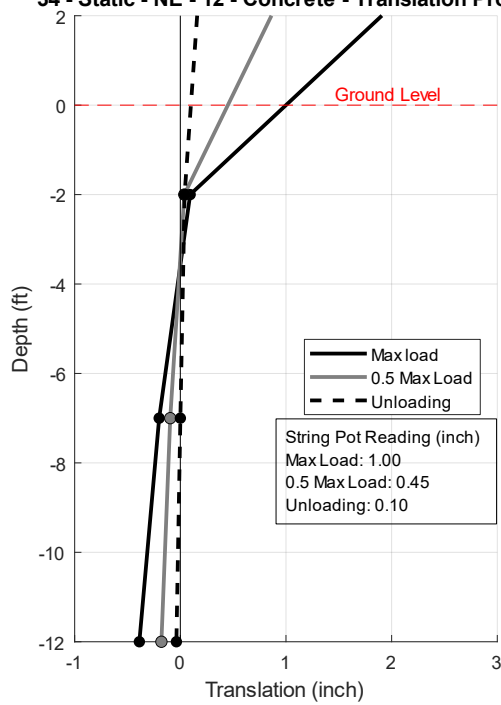


Figure 6.9 Translation vs depth of static tests on NE direction performed on pole 12–Concrete, the 700-yr design load is approximately 0.5 of the maximum load

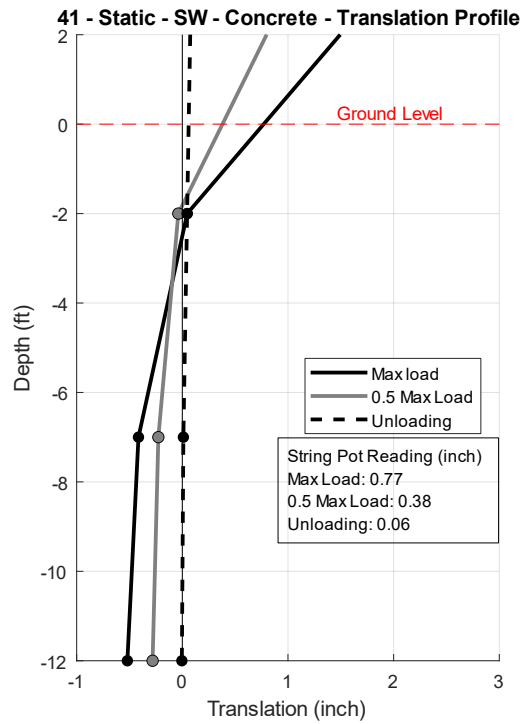
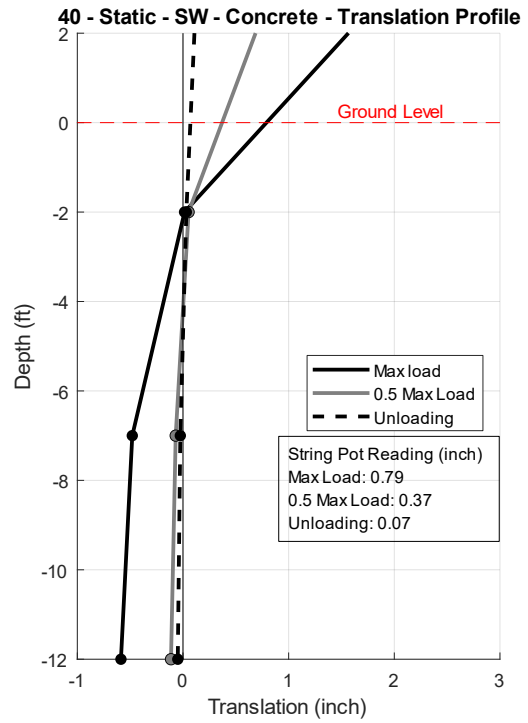
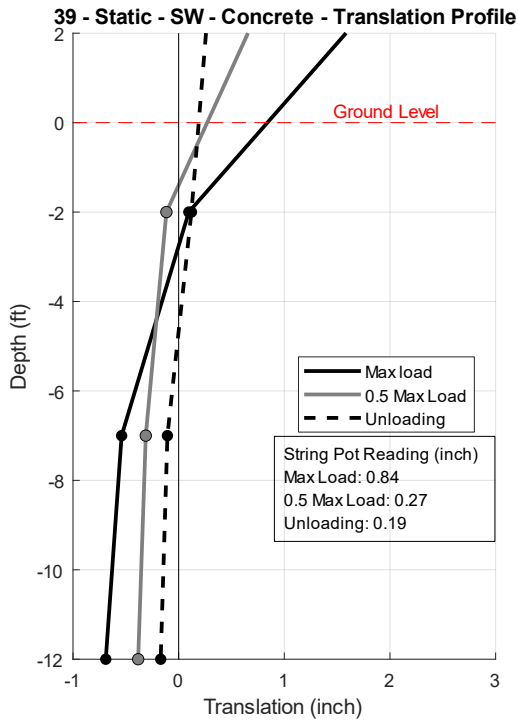


Figure 6.10 Translation vs depth of static tests on SW direction performed on pole 12–Concrete, the 700-yr design load is approximately 0.5 of the maximum load

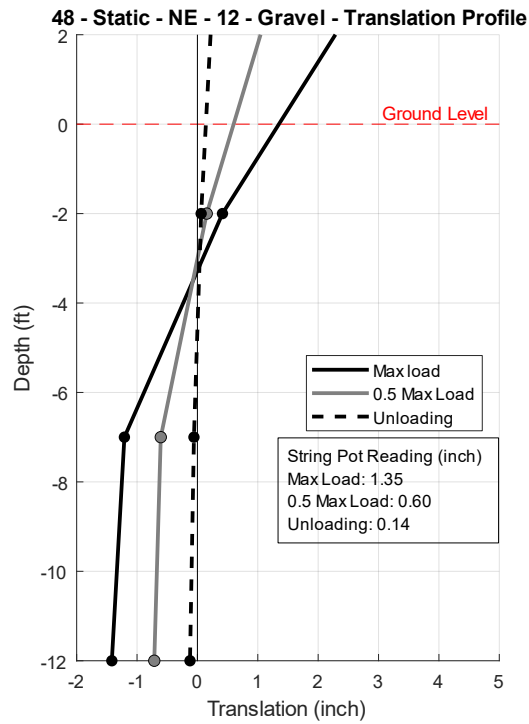
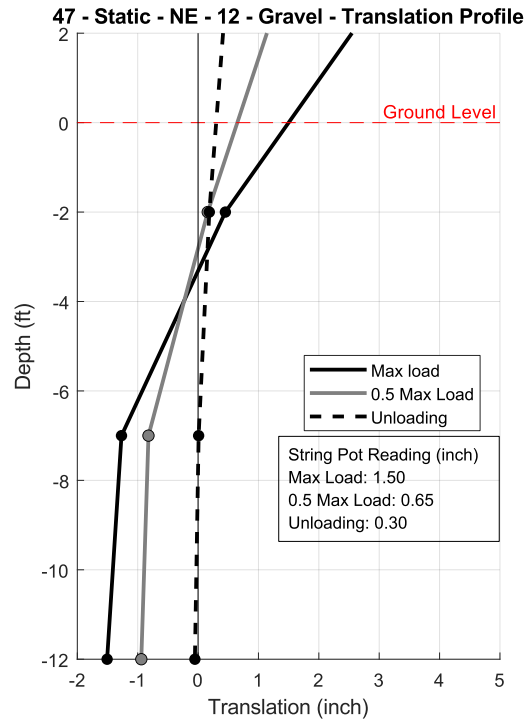
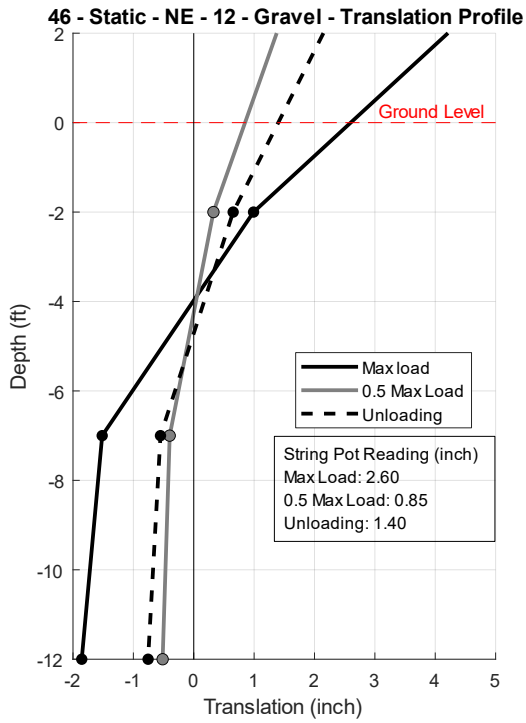


Figure 6.11 Translation vs depth of static tests on NE direction performed on pole 12–Gravel, the 700-yr design load is approximately 0.5 of the maximum load

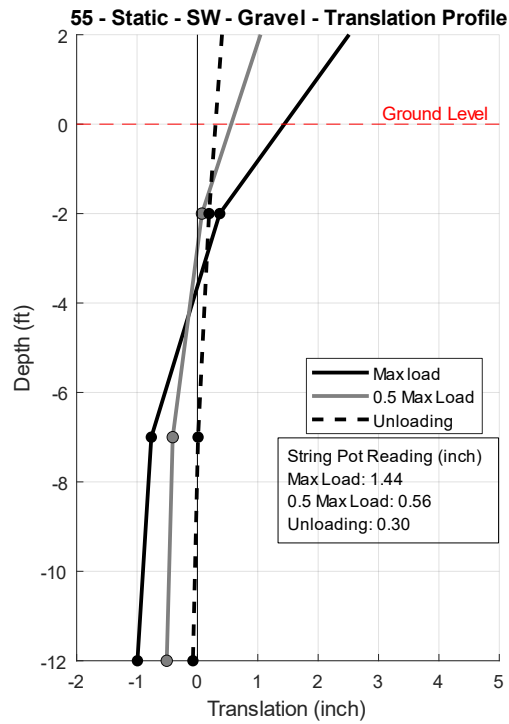
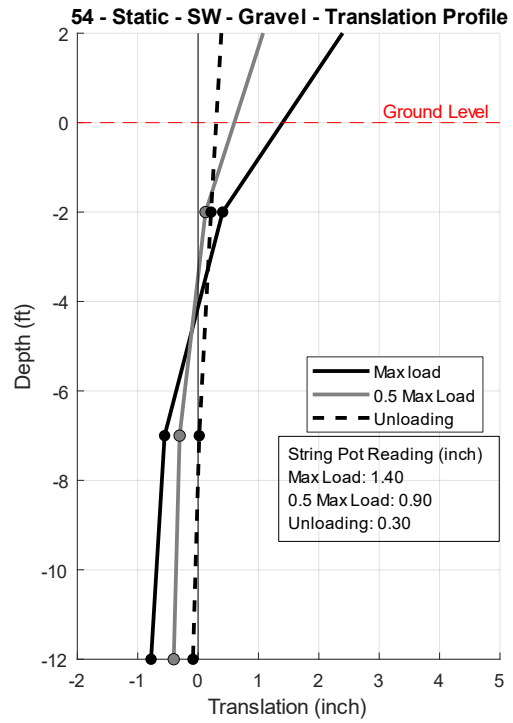
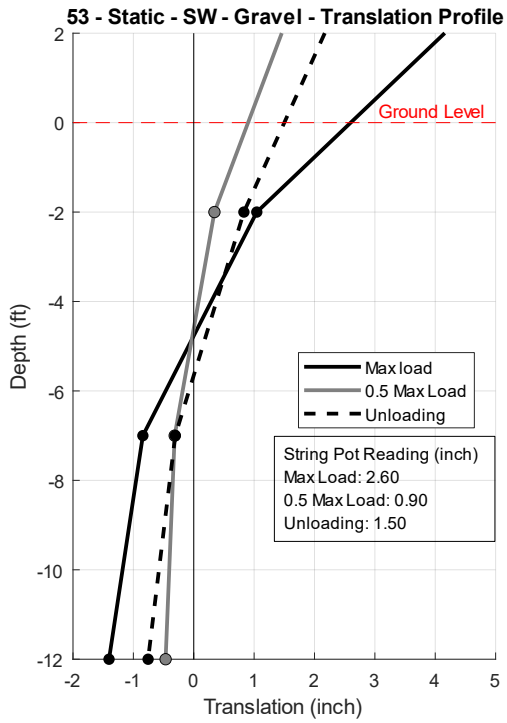


Figure 6.12 Translation vs depth of static tests on SW direction performed on pole 12–Gravel, the 700-yr design load is approximately 0.5 of the maximum load

Translation versus Depth Observations

- The translation vs depth followed the expected curve/behavior.
- At unloading, the translation at ground level returned to near zero.
- Near the top of the shaft, zero translation occurred around two to three feet. This is consistent with a typical assumption that the topsoil layer does not contribute significantly to stiffness.
- For the 16 –Concrete pole, the translation profile was consistent for all three static tests performed in the SE direction, as shown in Table 6.6. The translation at the ground level at all load levels was close; for example, it ranged between 0.39 to 0.44 inches and 0.18 to 0.23 inches for maximum load and half of the maximum load, respectively. The design-level load is about 0.5 of the max load. In all cases, the groundline translations were reasonable.
- The deflected shape demonstrated the flexibility of the shaft relative to the soil/gravel.
- The translation and rotation for the 12-ft shafts at the bottom were typically non zero, indicating that a deeper shaft would be necessary to push that back to zero translation and slope.
- The translations for the 16-ft shafts were typically lower than the 12-ft, and the bottom slope is close to zero. This indicated that a deeper foundation for the same diameter and loads would not improve performance.
- The quality of the data is good and can be used to compare with numerical computations. Observations were found for all other poles, as shown in Figure 6.7 to Figure 6.12.

6.2 Pluck Test Results

As mentioned, six pluck tests in two opposite directions were performed on each pole. The free vibration response for each test was recorded using accelerometers positioned along the poles. The time vs. acceleration response of all pluck tests performed in one direction of each pole is shown in Figure 6.13 to Figure 6.20. The log-decrement method was used to calculate the damping ratio by taking the average results of three trials. Then, the damping ratio of each pole in one direction was calculated, and the averages are reported in Table 6.2. The reduction in the damping ratio with amplitude during pluck tests was observed, as shown in Figure 6.22 and Figure 6.23 for 16-Gravel and 12-Gravel poles. This observation suggests the presence of nonlinear damping effects in the system; the damping mechanisms are less effective at small translations and become more significant as the translation increases, as shown in Figure 6.24.

Table 6.2 Results of the pluck tests performed on the poles showing the damping ratio in each direction

Pole No.	Direction	Pluck test No.	Damping ratio	Average Damping Ratio	
16 – Concrete	NW	01	0.0089	0.0086	
		02	0.0081		
		03	0.0089		
	SE	08	0.0081		0.0105
		09	0.0109		
		10	0.0125		
16 – Gravel	NE	15	0.0417	0.0422	
		16	0.0399		
		17	0.0449		
	SW	22	0.0269		0.0273
		23	0.0287		
		24	0.0261		
12 – Concrete	NE	29	0.0112	0.0125	
		30	0.0114		
		31	0.0149		
	SW	36	0.0191		0.0192
		37	0.0206		
		38	0.0179		
12 - Gravel	NE	43	0.0298	0.0336	
		44	0.0350		
		45	0.03612		
	SW	50	0.0366		0.0355
		51	0.0333		
		52	0.0364		

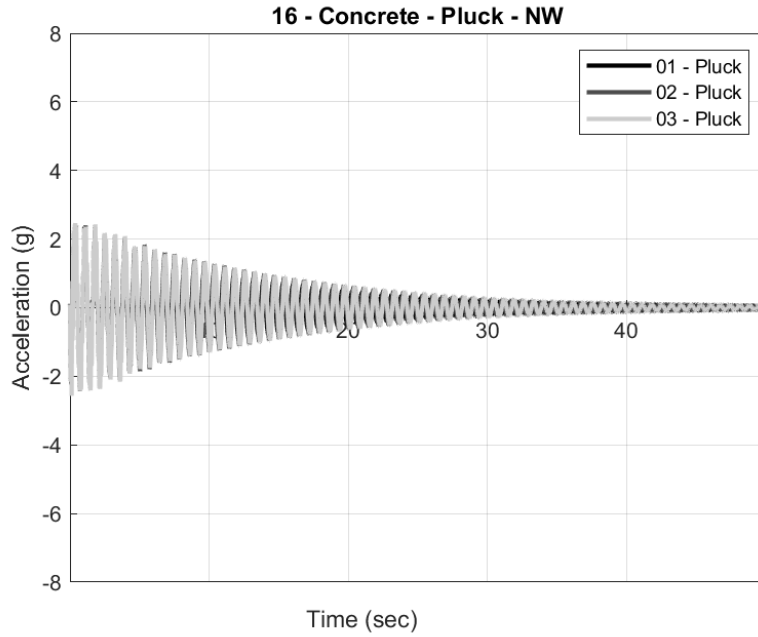


Figure 6.13 Time vs acceleration response of the pluck tests performed in the NW direction for pole 16–Concrete

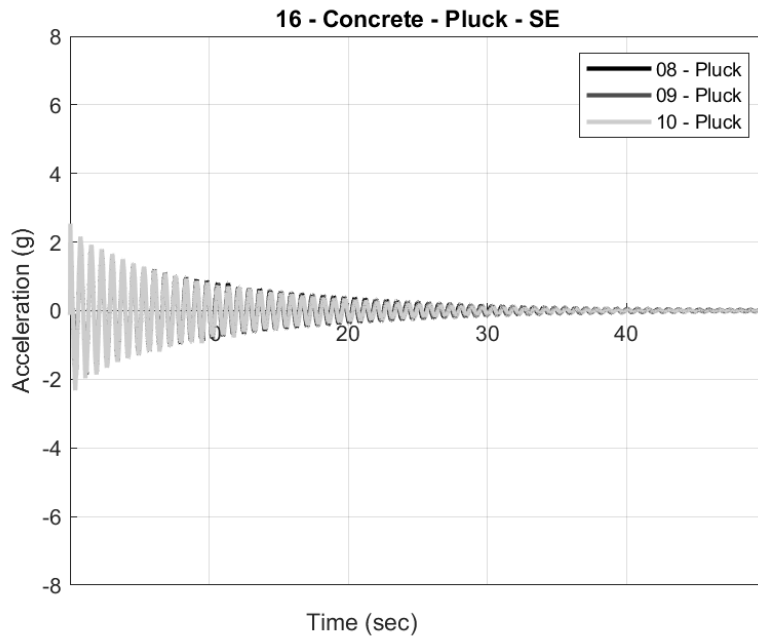


Figure 6.14 Time vs acceleration response of the pluck tests performed in the SE direction for pole 16–Concrete

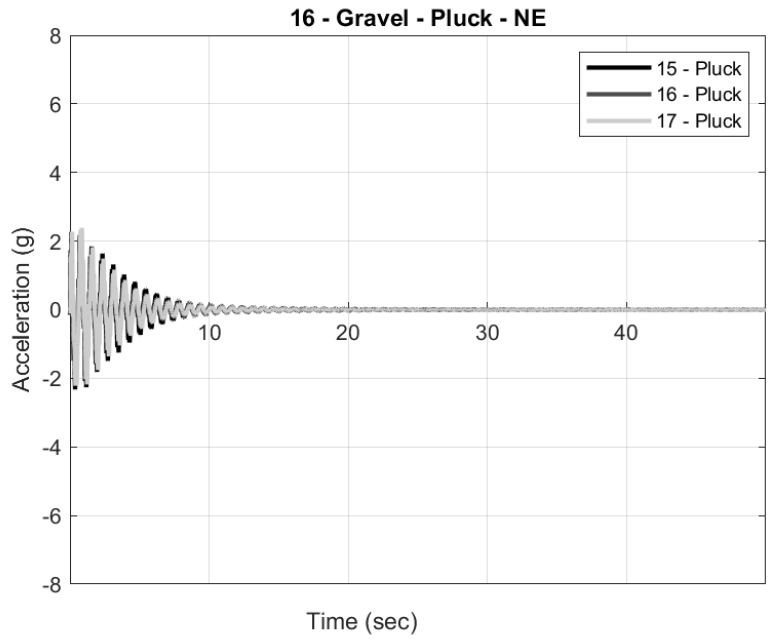


Figure 6.15 Time vs acceleration response of the pluck tests performed in the NE direction for pole 16–Gravel

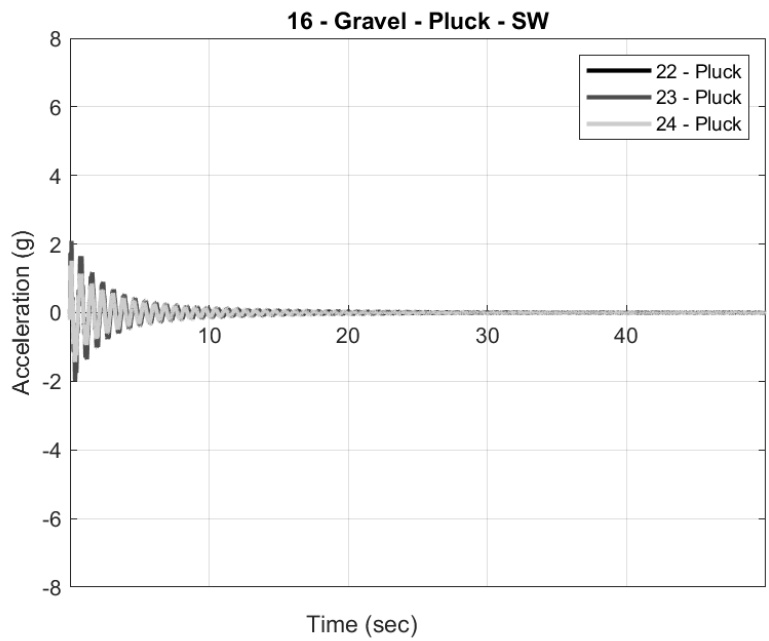


Figure 6.16 The time vs acceleration response of the pluck tests performed in the SW direction for pole 16-Gravel

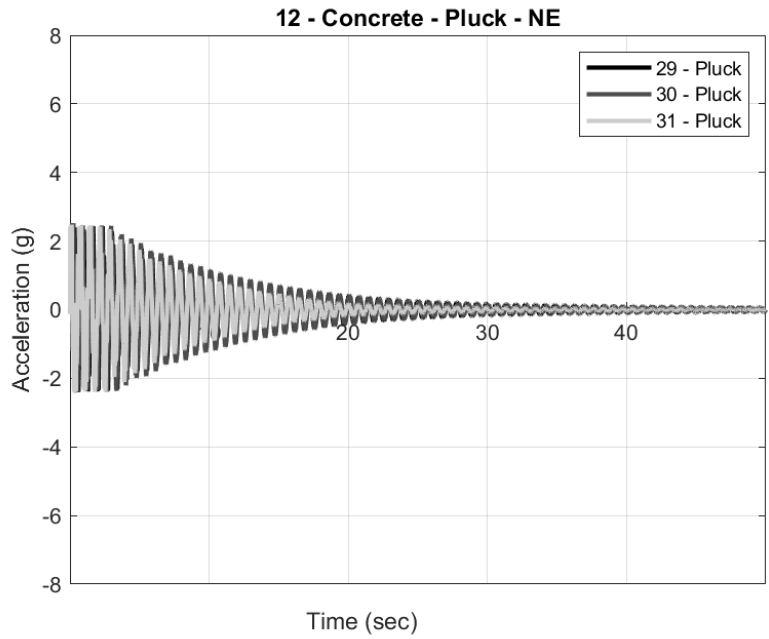


Figure 6.17 Time vs acceleration response of the pluck tests performed in the NE direction for pole 12–Concrete

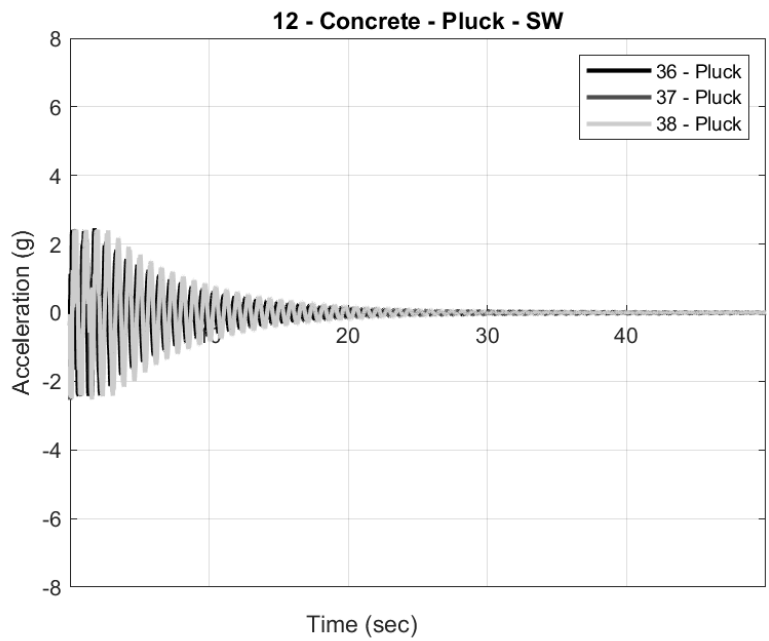


Figure 6.18 Time vs acceleration response of the pluck tests performed in the SW direction for pole 12–Concrete

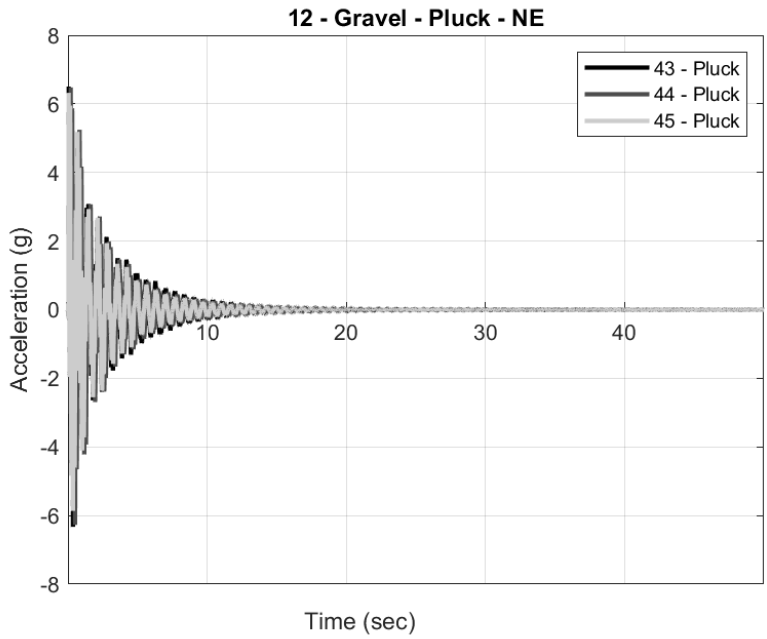


Figure 6.19 Time vs acceleration response of the pluck tests performed in the NE direction for pole 12-Gravel

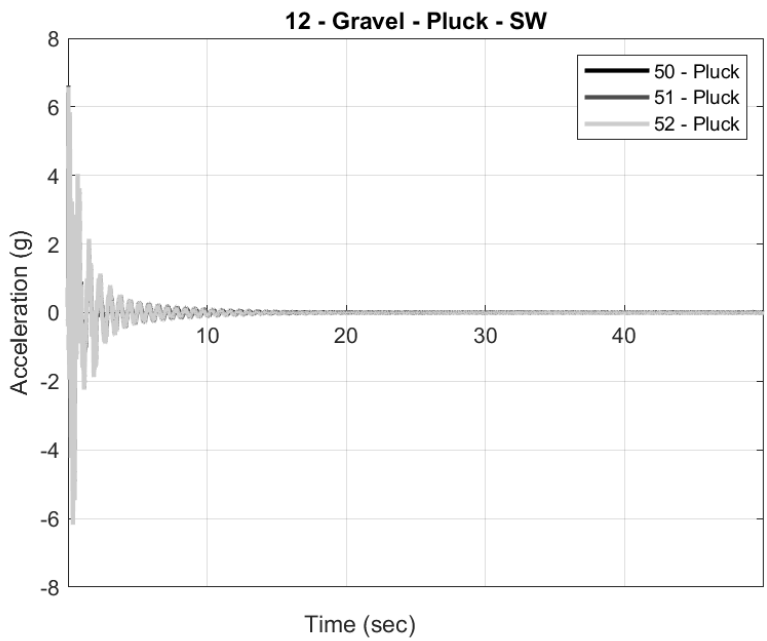


Figure 6.20 Time vs acceleration response of the pluck tests performed in the SW direction for pole 12-Gravel

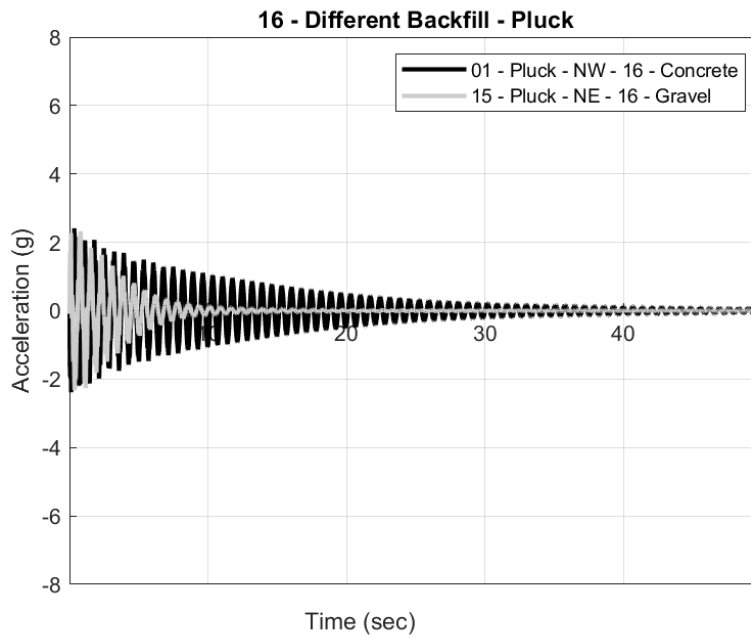
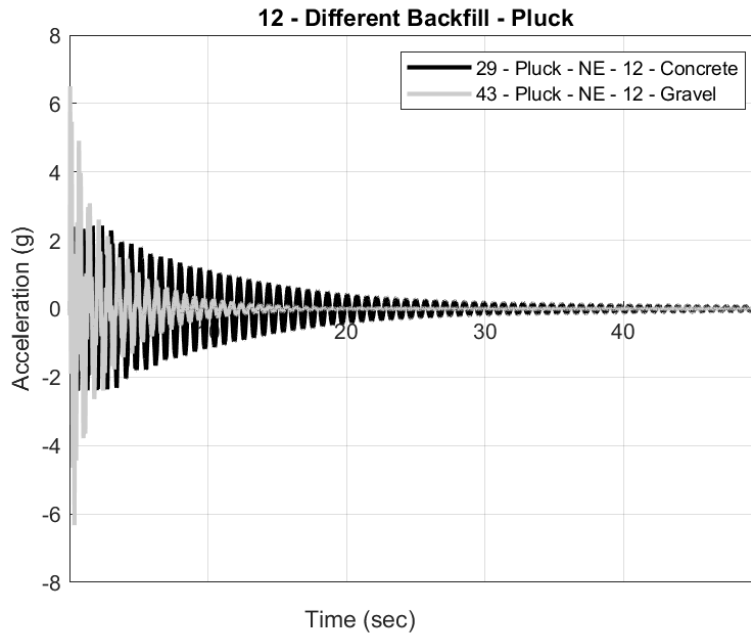


Figure 6.21 Comparison between the damping performance for poles with different backfill material

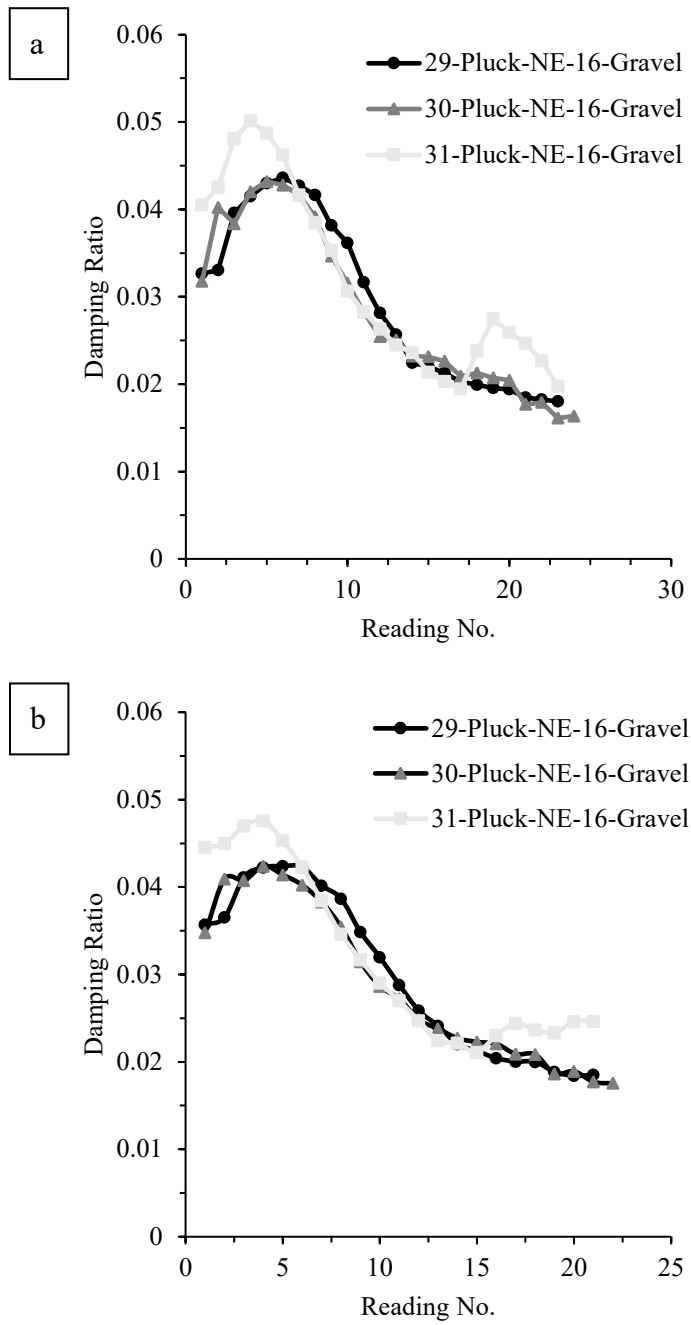


Figure 6.22 The reduction in damping ratio with time for 16-Gravel pole (a) 5-cycle running, and (b) 7-cycle running

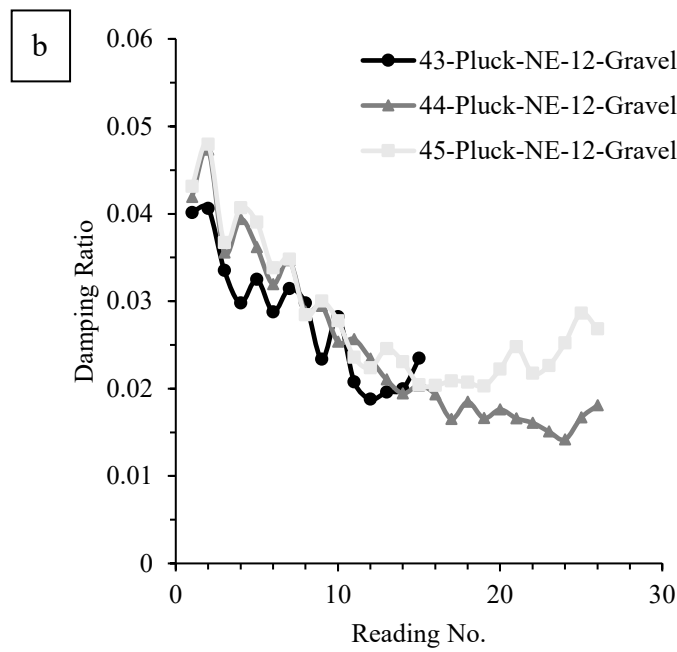
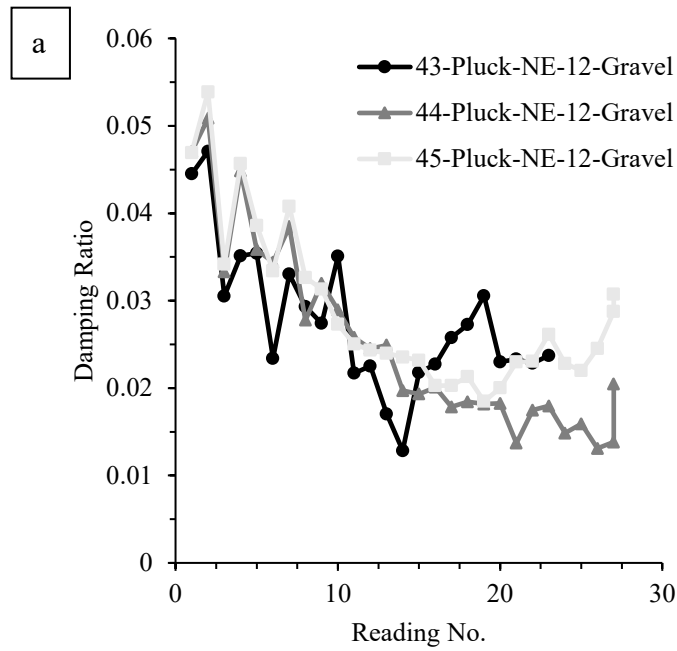


Figure 6.23 The reduction in damping ratio with time for 12-Gravel pole (a) 5-cycle running, and (b) 7-cycle running

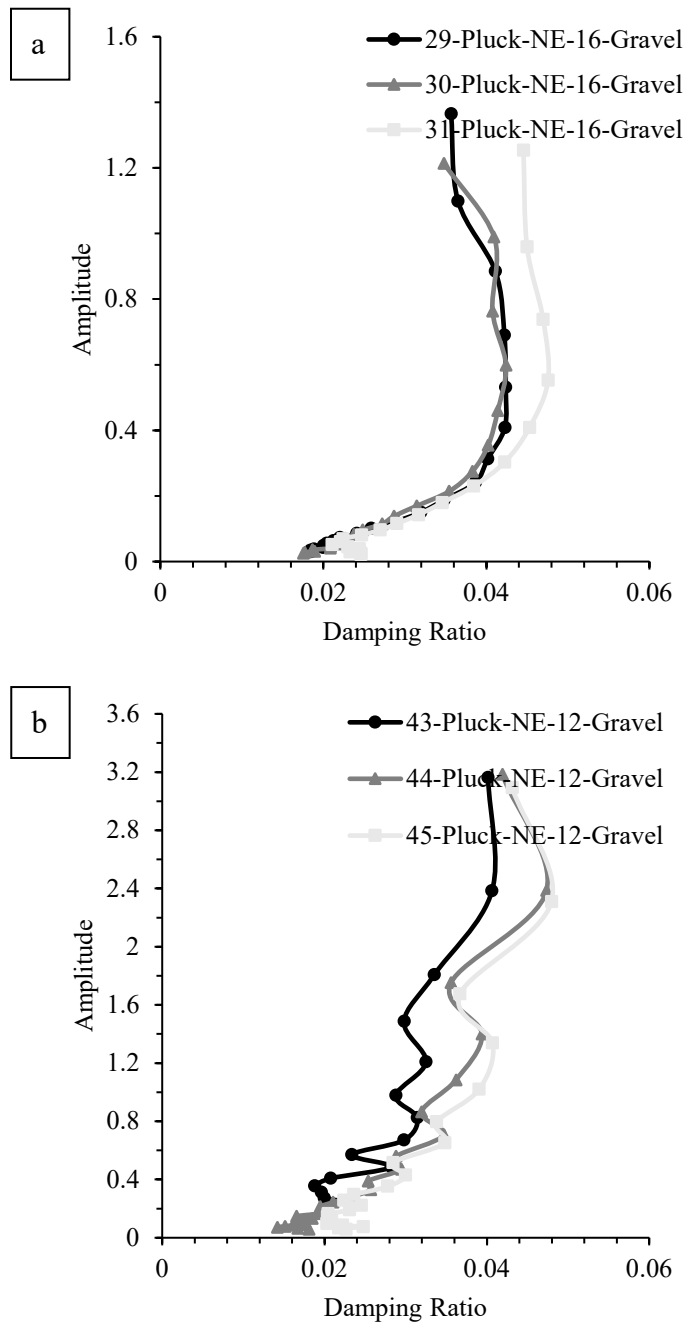


Figure 6.24 The change in damping ratio with amplitude for (a) 16-Gravel pole, and (b) 12-Gravel pole

Pluck Test Observations

- The backfill material had a significant impact on the free-vibration performance. Poles with gravel backfill obtained a higher damping ratio than poles with the same embedment depth and had a concrete backfill, as shown in Figure 6.21.
- The damping ratios for pole 16–Gravel in both directions were 0.042 and 0.027, which were higher than the damping observed for pole 16–Concrete pole, as the damping ratios were 0.009 and 0.011.
- The same behavior was observed for poles with a direct embedment depth of 12 feet; the damping ratios of the 12–Gravel pole in both directions were 0.034 and 0.036, while for the 12–Concrete pole, the damping ratios were 0.013 and 0.019 in both directions, respectively.
- The effect of embedment depth on the damping performance did not show a clear trend; for example, the damping ratio increased from 0.009 to 0.013 as the embedment depth decreased from 16 to 12 feet for concrete backfill. Alternatively, it decreased for gravel backfill from 0.042 to 0.034 as the embedment depth decreased from 16 to 12 feet.
- The inherent damping of a typical pole with a baseplate and anchor rods is small – often less than 0.005. In general, all installations exhibited increases over the typical case. Any value approaching 0.01 is considered large for these structures. The implications are significant and are discussed below.
- Non-linear damping was observed from the log-decrement predictions. Lower amplitude vibrations resulted in lower damping. This will help explain the damping observed in the forced vibration testing results.

6.3 Forced-Vibration Test Results

Two forced-vibration tests were performed in two opposite directions for each pole. The primary reason was to determine the natural frequencies and evaluate the effect of the backfill material used and the depth of the directly embedded foundation. A Fast Fourier Transform (FFT) was performed with the accelerometer data acquired from the forced-vibration test to determine the first three natural frequencies. The results of the FFT are shown in Appendix B. Table 6.3 shows the natural frequencies computed for each pole in both directions. Table 6.5 shows the damping ratios calculated using Half-Power Band Width.

Table 6.3 The natural frequencies determined from the FFT analysis

Pole No.	Direction	Test No.	First Natural Freq. (Hz)	Second Natural Freq. (Hz)	Third Natural Freq. (Hz)
16 - Concrete	NW	07	1.33	10.56	25.77
	SE	14	1.30	8.39	21.41
16 - Gravel	NE	21	1.38	10.37	23.66
	SW	28	1.35	10.30	24.98
12 - Concrete	NE	35	1.30	8.39	21.72
	SW	42	1.18	7.51	19.31
12 - Gravel	NE	49	1.36	6.64	17.7
	SW	56	1.32	6.57	17.6

Table 6.4 Percent reduction observed in the natural frequencies

Pole No.	% reduction f_{n1}	% reduction f_{n2}	% reduction f_{n3}
16 - Concrete	2.25	20.54	16.91
16 - Gravel	2.17	0.67	-5.57
12 - Concrete	9.23	10.48	11.11
12 - Gravel	2.94	1.05	0.56

Table 6.5 Damping ratios calculated using Half-Power Band Width

Pole No.	Direction	Test No.	Damping Ratio		
			Mode 1	Mode 2	Mode 3
16 - Concrete	NW	07	-	0.0005	0.0007
	SE	14	0.0048	0.0005	0.0003
16 - Gravel	NE	21	0.0026	0.0009	0.0005
	SW	28	0.0044	0.0007	0.0006
12 - Concrete	NE	35	0.0046	0.0004	0.0015
	SW	42	0.0031	0.0010	0.0006
12 - Gravel	NE	49	0.0068	0.0005	0.0006
	SW	56	0.0023	0.0005	0.0008

Forced-Vibration Test Observations

- The reduction in the natural frequencies was significant for poles with concrete backfill. For example, for 16–Concrete pole, the reduction was 2.25, 20.54, and 16.91 % in the first, second, and third natural frequencies, respectively. For the 16–Gravel pole, the maximum reduction observed was 2.17%. The percentage reduction values are listed in Table 6.4.
- Poles with a 16-ft embedment depth experienced a higher natural frequency than poles with 12-ft embedment depth. This demonstrates that a deeper embedment depth increases the stiffness of the system, thereby increasing its natural frequency.
- There was a difference in the damping ratios determined from the log-decrement method and the half-power bandwidth. This can be explained by the significant difference in the amplitude of vibration between the pluck and forced vibration tests. The translation due to the pull during the pluck test was a couple of feet, as shown in the previous chapter, while the translation caused by the forced vibration test was less than 1 inch.

6.4 Finite Element Analysis Results

6.4.1 Natural frequencies

The mode shapes and the natural frequencies obtained from SAP2000™ for each case are shown in Figure 6.25 to Figure 6.30. Table 6.6 compares the natural frequencies obtained from the experimental testing and the finite element analysis results.

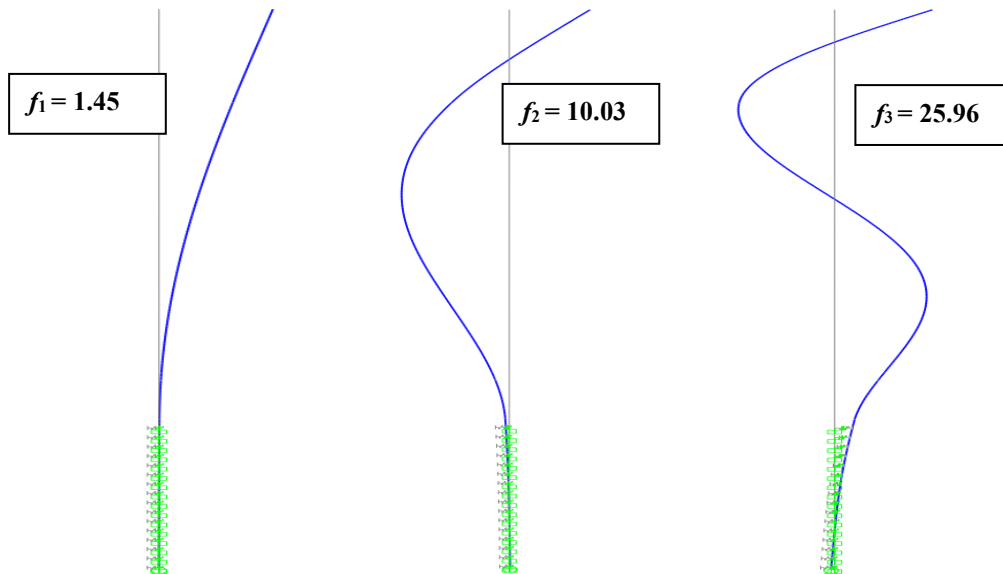


Figure 6.25 Mode shapes and natural frequencies obtained from FEA for Case 1

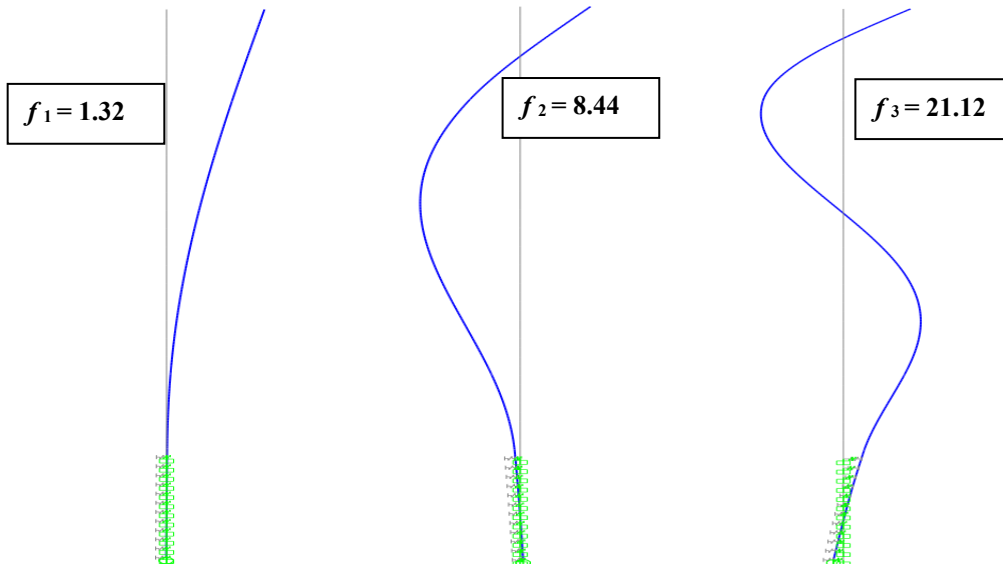


Figure 6.26 Mode shapes and natural frequencies obtained from FEA for Case 2

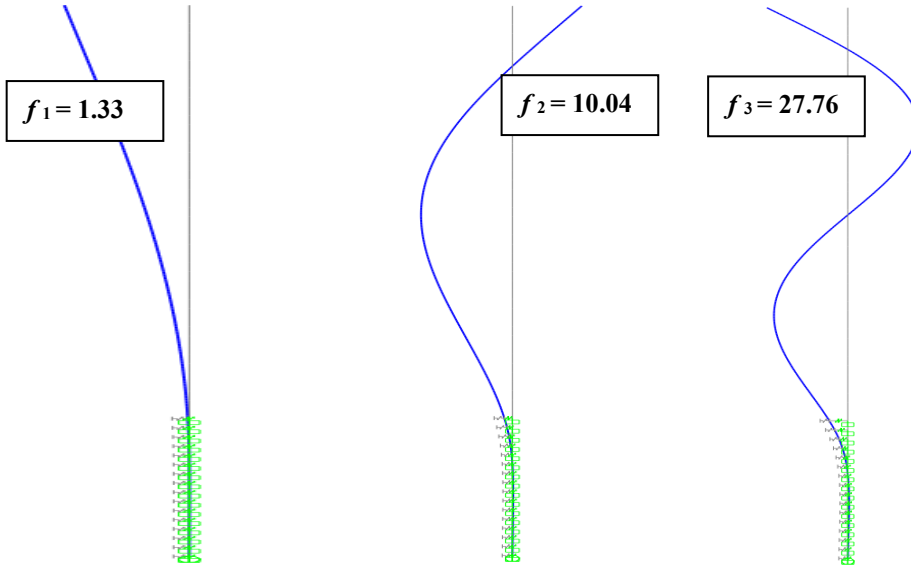


Figure 6.27 Mode shapes and natural frequencies obtained from FEA for Case 3

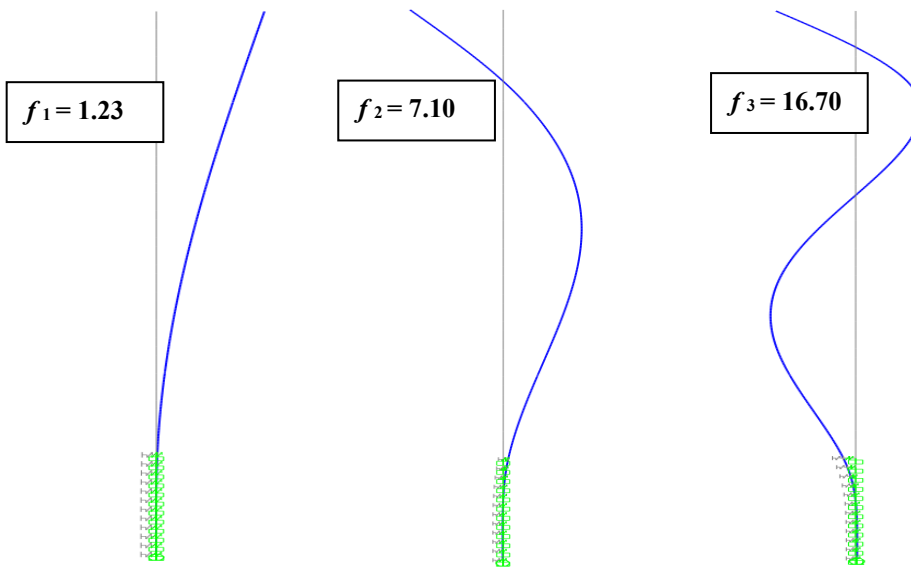


Figure 6.28 Mode shapes and natural frequencies obtained from FEA for Case 4

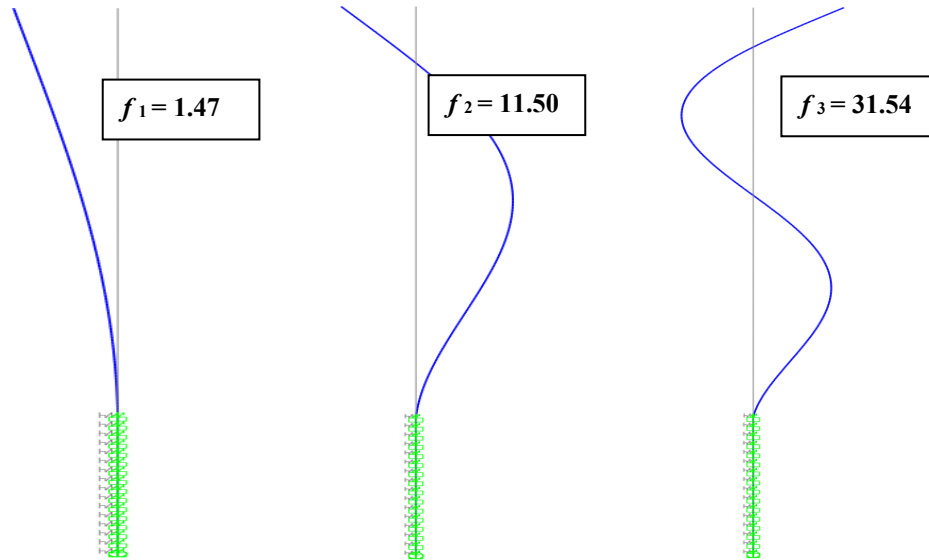


Figure 6.29 Mode shapes and natural frequencies obtained from FEA for Case 5

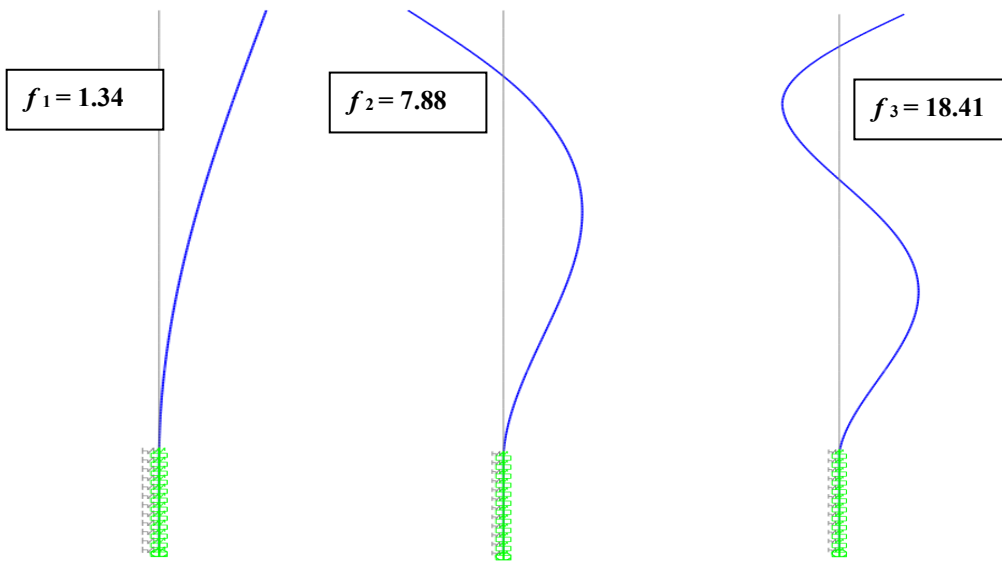


Figure 6.30 Mode shapes and natural frequencies obtained from FEA for Case 6

Table 6.6 Comparison between the natural frequencies obtained from the experimental results and the FEA results

FEA Case	Exp. Pole	Mode Shape	Test	FEA	%
Case 1	16 - Concrete	1	1.33	1.45	9.02
		2	10.56	10.03	5.02
		3	25.77	25.96	0.74

FEA Case	Exp. Pole	Mode Shape	Test	FEA	%
Case 2	12 - Concrete	1	1.30	1.32	1.54
		2	8.39	8.44	0.60
		3	21.72	21.12	2.76
Case 3	16 - Gravel	1	1.38	1.33	3.62
		2	10.37	10.04	3.18
		3	23.66	27.76	17.33
Case 4	12 - Gravel	1	1.36	1.23	9.56
		2	6.64	7.1	6.93
		3	17.7	16.7	5.65
Case 5	16 - Gravel	1	1.38	1.47	6.52
		2	10.37	11.5	10.90
		3	23.66	31.54	33.31
Case 6	12 - Gravel	1	1.36	1.34	1.47
		2	6.64	7.88	18.67
		3	17.7	18.41	4.01

Finite Element Analysis Observation

- For poles with concrete backfill, the difference between the experimental and FEA results was less than 10%; thus, using Round Shaft with Casing and Core/insert for the foundation, as mentioned in Cases 1 and 2, provided a good estimation for the natural frequencies.
- For poles with gravel backfill, two cases were analyzed for each embedment depth as the LPILE cannot change the properties of the soil in the radial direction. The main difference was the medium surrounding the foundation; soil was the medium for Cases 3 and 4, while gravel was the medium for Cases 5 and 6. Cases 3 and 4 better predict the natural frequencies than Cases 5 and 6, as shown in Table 6.6. The maximum difference was less than 10% and 17% for Case 3 and Case 4, respectively, for Case 5 and Case 6, it was 34% and 19%, respectively. As the mass was predictable, stiffness was the primary variable in the computation of

natural frequencies. These results illustrate that LPILE and FEA using boring report data provided reasonable estimates of the foundation stiffness.

6.4.2 Translation Profile

The translation profiles measured from the experimental test results were compared to the LPILE analyses of Cases 3 through 6 to determine the better configuration for studying poles with gravel backfill.

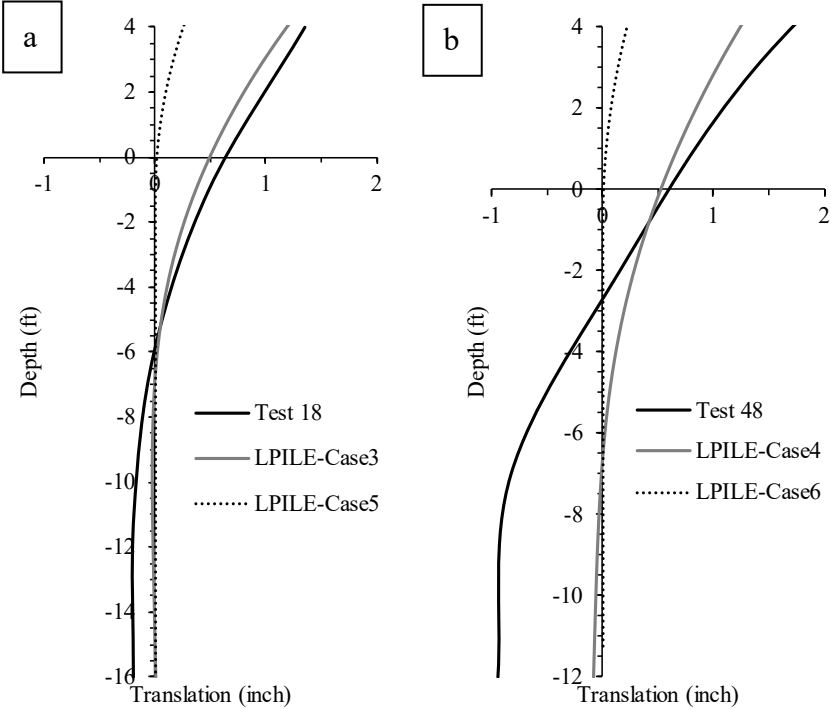


Figure 6.31 Comparison between LPILE cases for gravel backfill (a) 16-foot gravel backfilled pole, and (b) 12-foot backfilled pole

Finite Element Analysis Observation

- Figure 6.31 (a) compares the translation profile from a static test on the 16-Gravel backfilled pole to the translation profiles obtained from LPILE Case 3 and Case 5. The results indicate that Case 3 provides a more accurate translation estimate than Case 5. The translation profile of Case 5 was nearly zero below the ground surface and exhibited minimal movement above it.

- A similar behavior was observed in Figure 6.31 (b) for the 12-foot gravel backfilled pole, where Case 5 provided a better estimate than Case 6. Therefore, it is recommended to use Case 3 and Case 4 for analyzing poles with gravel backfill in LPILE, or other p-y analysis software.

6.5 Observed Damage and Failure Modes

These poles were loaded well above the 700-yr MRI, the design load for the NDOT standard pole. Even under severe loading, the observed damage was minimal. Figure 6.32 illustrates that the permanent translation between the shaft and the soil was about 0.25 – 0.375 in. The concrete shaft is unreinforced and expected to crack. Also shown is a radial crack of similar size. Note that the alternative design was gravel backfill, so concrete cracks would not be of significant concern. Regarding esthetic concerns, typically the top of the shaft was covered with a top-soil layer and the top few feet were not considered in the resistance computations.



Figure 6.32 Observed damage in poles with concrete backfill after static tests

Figure 6.33 shows the gravel backfill after the severe loading where 2-inch voids were created. Again, typically this was covered by topsoil and vegetation. This picture illustrates the toughness of directly embedded shafts. The translations were large, especially on 12-Gravel; however, the pole hysteretic behavior was stable. If damage was observed, noting that the pole itself is undamaged, maintenance would then have the opportunity to plumb the pole and backfill it with additional gravel. Essentially, this method provides a structural fuse that is fixable.



Figure 6.33 Observed damage in poles with gravel backfill after static tests

Chapter 7 Discussion

This section discusses the results from the experiments and modeling in the context of design. The experimental program can address two main design considerations. The first is the static load-carrying performance for the poles. The second is the impacts of the damping observed on the long-term performance of high-mast towers.

7.1 Load performance of the foundation

7.1.1 Experiment to Experiment Comparison

To evaluate the effects of the depth of the foundation and the type of backfill used, a comparison was made between the experimental results shown in Figure 7.1.

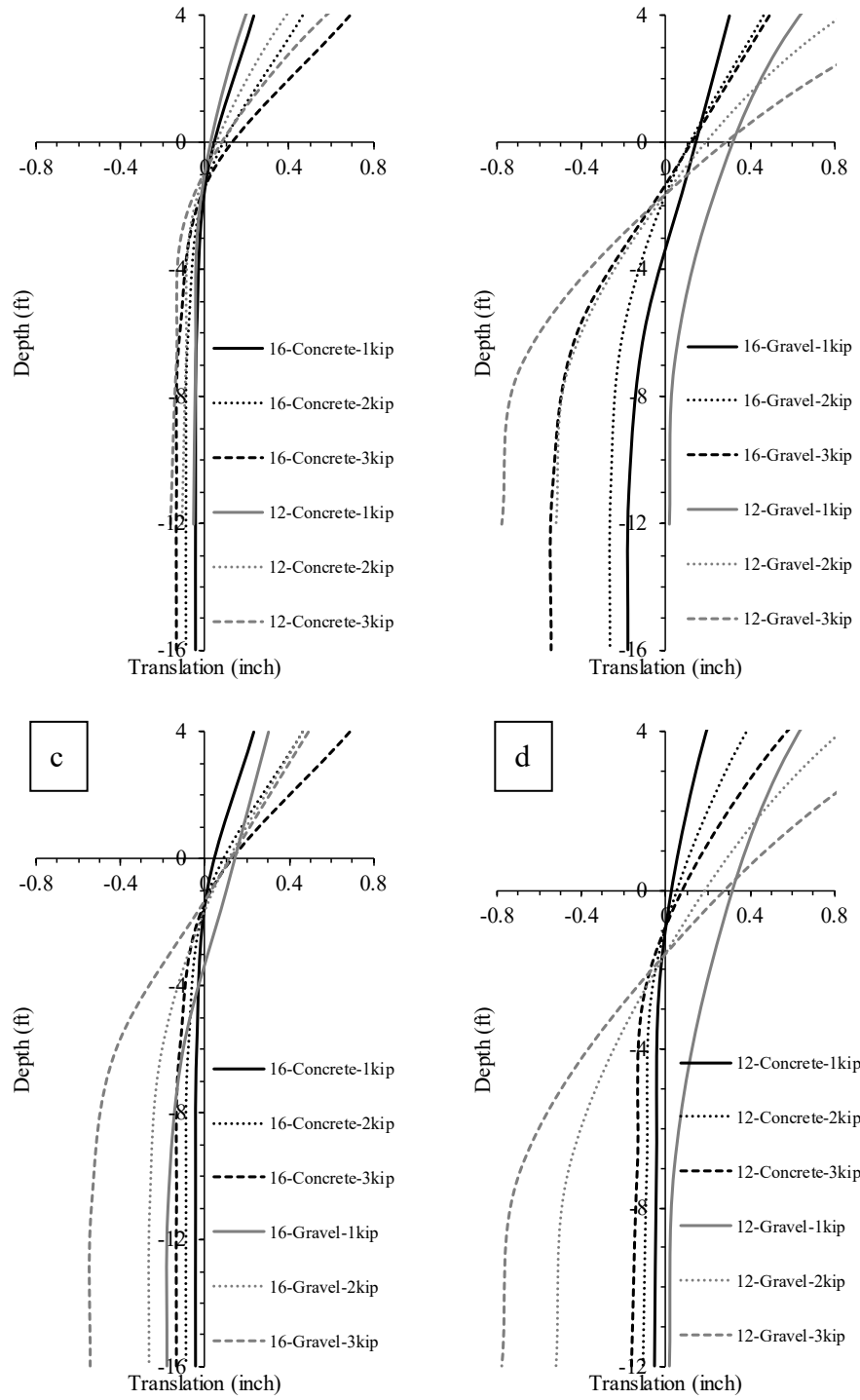


Figure 7.1 Comparison between translation profiles obtained from experimental results for poles with different backfill and embedment depths at various loads (a) pole with concrete backfill and different 16-ft embedment, (b) pole with gravel backfill and different embedment depths, (c) pole with 16-ft embedment depth and concrete backfill, and (d) poles with 12-ft embedment depth and gravel backfill

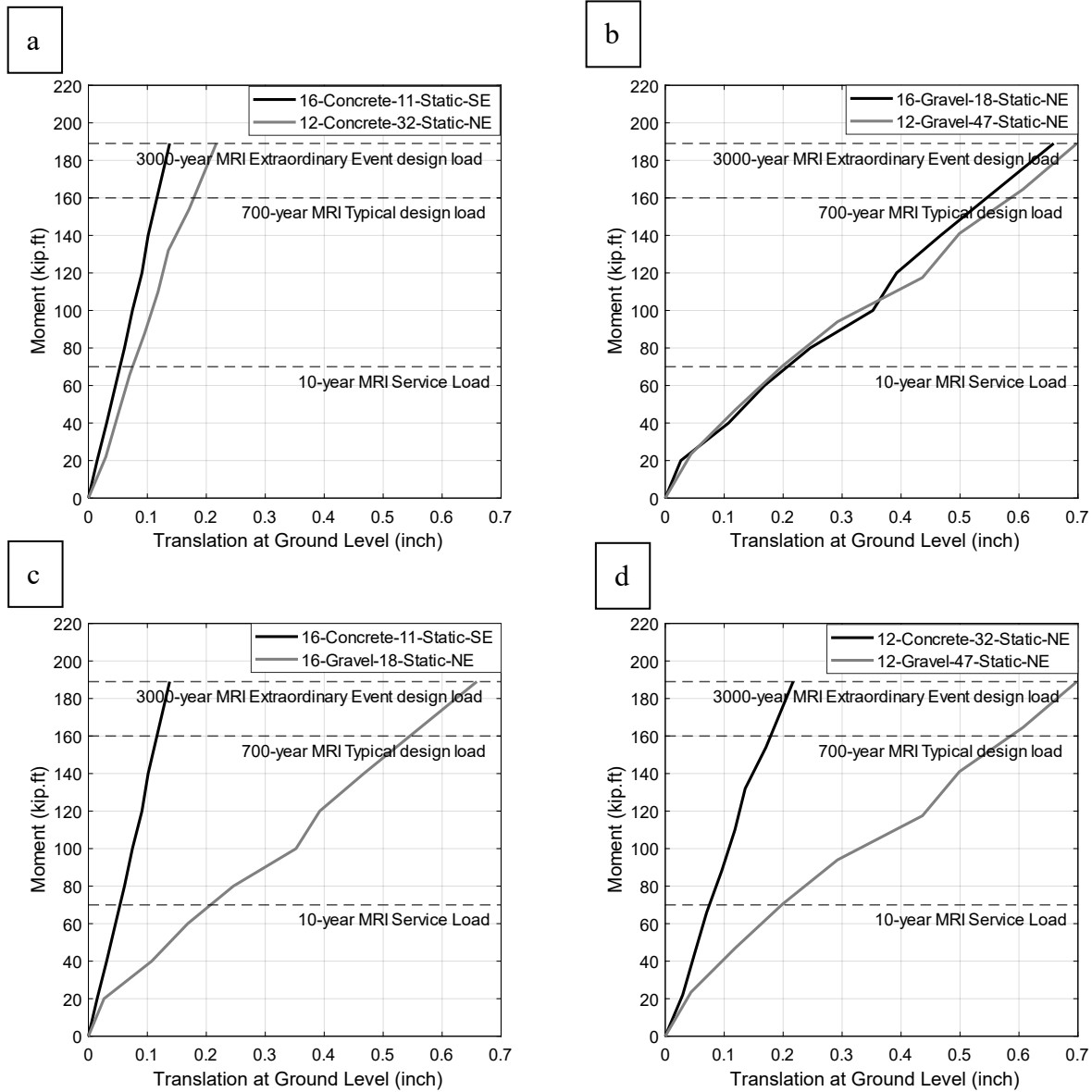


Figure 7.2 Comparison between translation at ground level obtained from experimental results for poles with different backfill and embedment depths (a) poles with concrete backfill and different embedment depths, (b) poles with gravel backfill and different embedment depths, (c) poles with 16-ft embedment depth and different backfill, and (d) poles with 12-ft embedment depth and different backfill

Experimental to Experimental Comparison Observations

- The translation of the pole with a 16-foot embedment depth was close to the 12-foot embedment depth; this means that concrete backfill can significantly reduce the translation, whether the embedment depth is 16 or 12 feet.
- On the other hand, the translation decreases as the embedment depth increases from 12 to 16 feet, as shown in Figure 7.1 (b).
- In cases where the poles had the same embedment depths but different backfills, as shown in Figure 7.1 (c) and (d), the concrete backfills experienced less translation compared to the gravel backfills; the higher stiffness and rigidity of the concrete can explain this.
- Figure 7.2 shows the translation at the ground level obtained from the string potentiometer during static tests. The results are consistent with the transition profile, as the poles with concrete backfill experienced less translation than those with gravel backfill.
- Moreover, the embedment depth neglected the translation at ground level for poles with concrete backfill, as shown in Figure 7.2 (a). The translation decreased as the embedment depth increased from 12 feet to 16 feet, as shown in Figure 7.2 (b).
- The maximum groundline translation was 0.2 and 0.7 inches for the concrete and gravel backfills, respectively for 3000-year loads. The performance for both backfills was within reasonable limits.

7.1.2 Experimental to LPILE Comparison

Experimental results were compared to the LPILE analysis, as shown in Figure 7.3. The results show that LPILE predicts a lower translation profile, especially for poles with gravel backfill. The results of Case 1 and Case 2, which contained concrete backfill, were close to the experimental results but predicted a lower translation profile, as shown in Figure 7.3 (a) and (b). On the other hand, the difference increased for poles with gravel backfill.

Experimental to LPILE Comparison Observations

- Figure 7.4 compares the translation at ground level obtained from static tests to the LPILE analysis. The results show that LPILE provides good estimates for the translation at ground level, especially for poles with concrete backfill.

7.1.3 LPILE to LPILE Comparison

The behavior in previous analyses was also observed when comparing various LPILE cases for translation at the groundline and translation profile of the foundation at various loads, as illustrated in Figure 7.5 and Figure 7.6.

LPILE to LPILE Comparison Observations

- LPILE cases with an embedment depth of 16 feet (Case 1 and Case 3) exhibited a reduced translation profile and lower translation at the ground surface than cases with a 12-foot embedment depth (Case 2 and Case 4).
- Furthermore, when comparing poles with identical embedment depths but different backfill materials, poles with concrete backfill demonstrated a smaller translation profile and lower translation at ground level than poles with gravel backfill. These findings align with the experimental results.

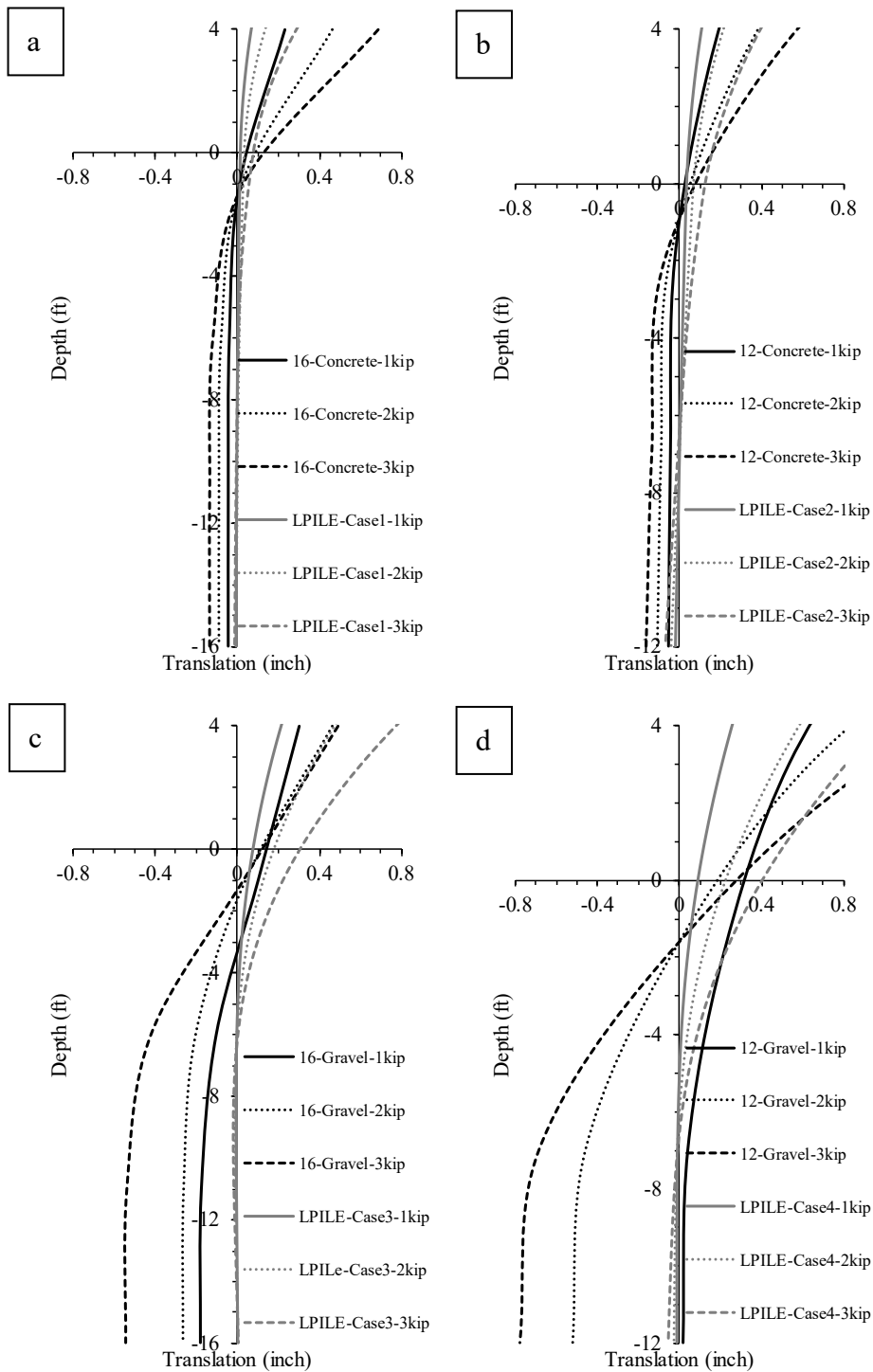


Figure 7.3 Comparison between the translation profile obtained from experimental results and LPILE for poles with different backfill and embedment depths at various loads (a) pole with concrete backfill and 16-ft embedment depths, (b) pole with concrete backfill and 12-ft embedment depths, (c) pole with gravel backfill and 16-ft embedment depths, and (d) pole with gravel backfill and 12-ft embedment depths

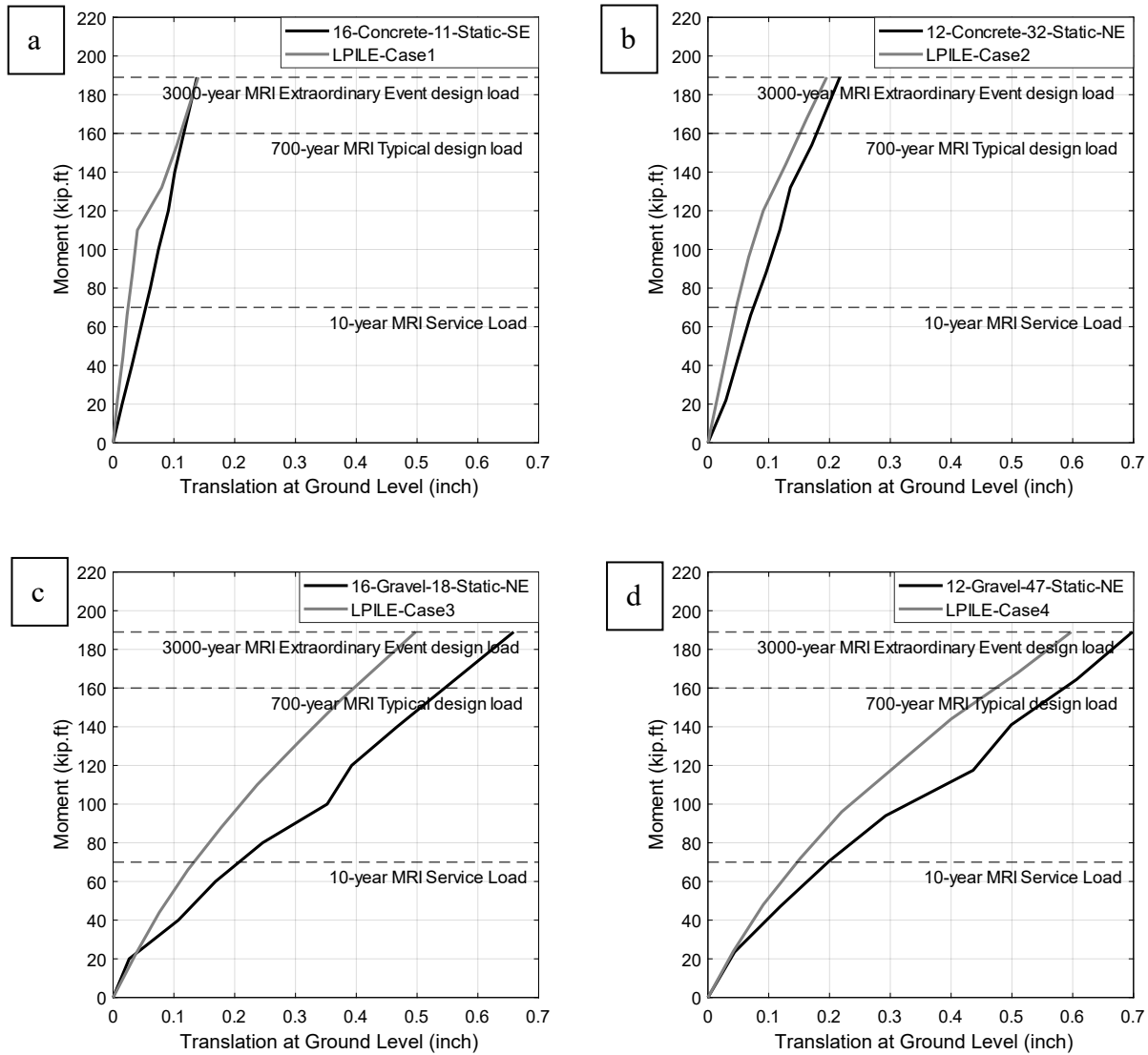


Figure 7.4 Comparison between translation at ground level obtained from experimental results and LPILE for poles with different backfill and embedment depths (a) pole with concrete backfill and 16-ft embedment depths, (b) pole with concrete backfill and 12-ft embedment depths, (c) pole with gravel backfill and 16-ft embedment depths, and (d) pole with gravel backfill and 12-ft embedment depths

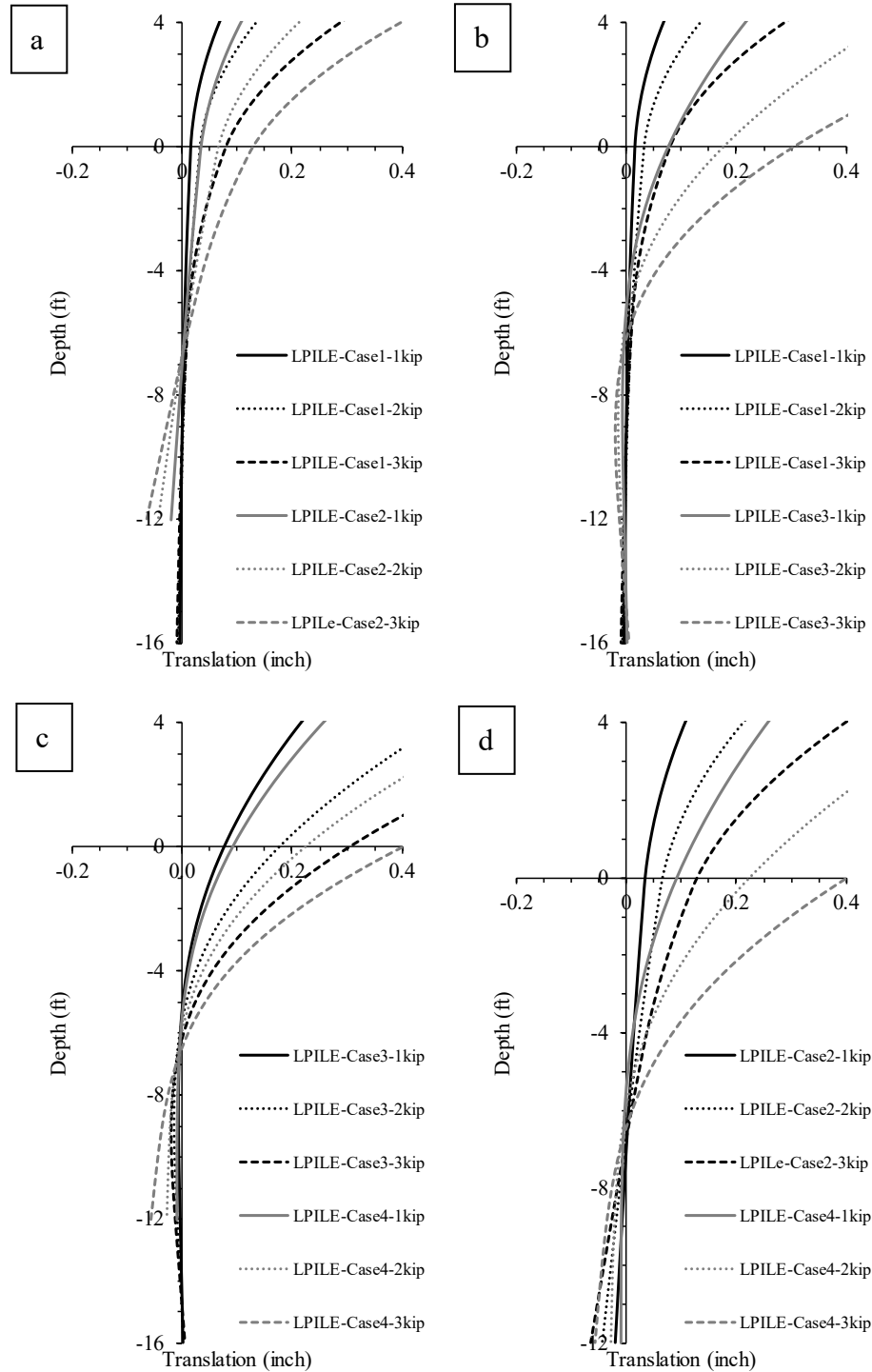


Figure 7.5 Comparison between translation profiles obtained from LPILE for cases with different backfill and embedment depths at various loads (a) cases with concrete backfill and different embedment depths, (b) cases with different backfill and 16-ft embedment depths, (c) cases with gravel backfill and different embedment depths, and (d) cases with different backfill and 12-ft embedment depths

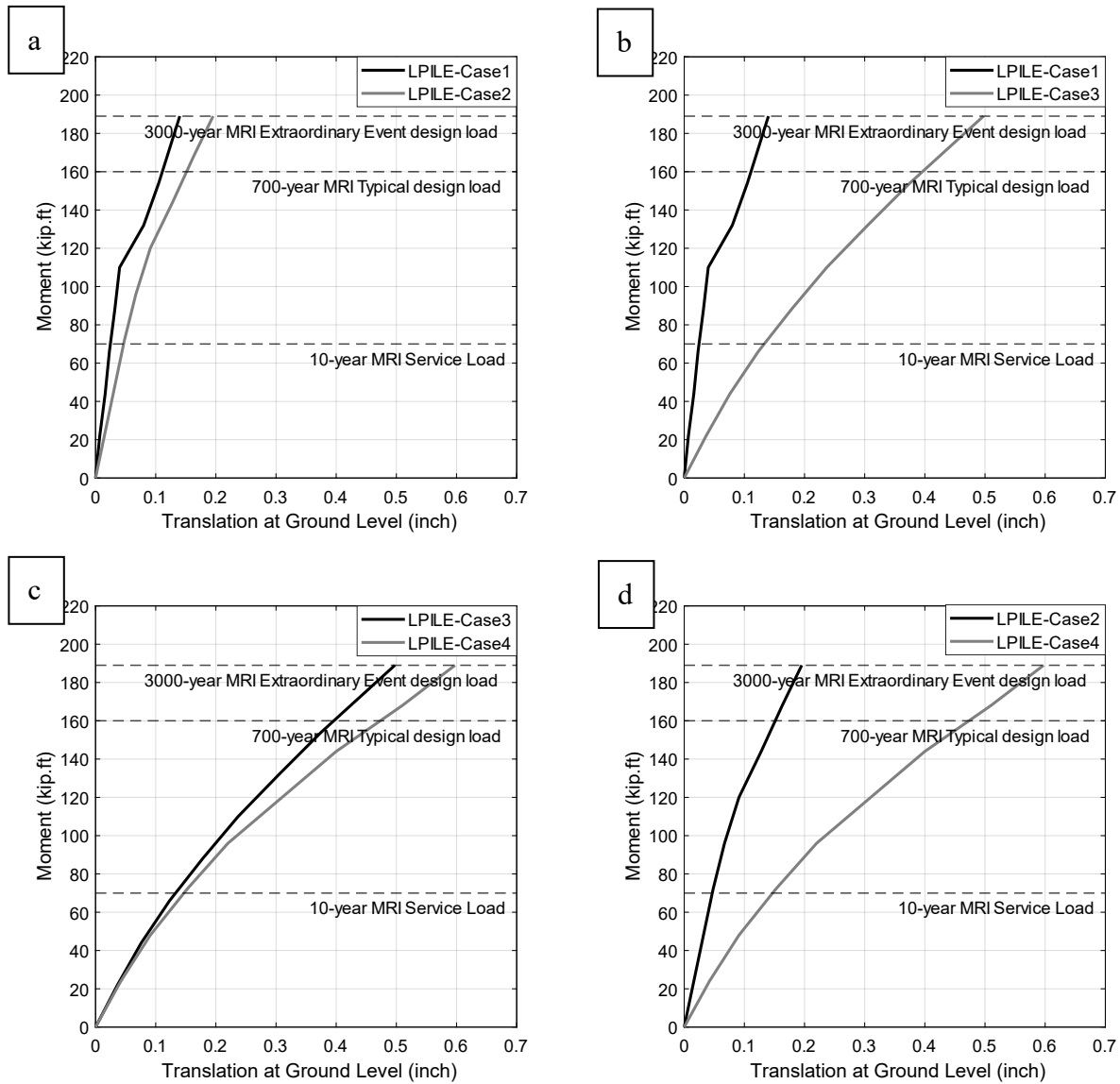


Figure 7.6 A comparison between translation at ground level obtained from LPILE for poles with different backfill and embedment depths (a) cases with concrete backfill and different embedment depths, (b) cases with different backfill and 16 ft embedment depths, (c) cases with gravel backfill and different embedment depths, and (d) cases with different backfill and 12-ft embedment depths

7.2 Effect of damping on design

7.2.1 Fatigue

The damping was measured for each pole, and the results are provided in the previous section. Damping positively affects the number of load cycles a pole may experience in its lifetime as energy from the wind is dissipated. This will lower the stress on fatigue-prone details and the number of cycles. From the AASHTO LTS-LRFD (American Association of State Highway and Transportation Officials, 2015), the load effects are compared to the resistance available with the limit state equation shown below (2024 interims).

$$\gamma \frac{(\Delta f)_n}{R} \leq \phi(\Delta F)_n \quad (7.1)$$

where:

1. $(\Delta f)_n$ = wind-induced nominal stress range defined in LTS-LRFD Article 11.9.2.
2. $(\Delta F)_n$ = the nominal fatigue resistance specified in LTS-LRFD Article 11.9.3 for the various detail classes identified in Article 11.9.1.
3. R = response modification factor to account for the effect of a vibration mitigation device (VMD) for a specific wind loading, defined below ($R = 1.0$ if no vibration-mitigation device is used).
4. γ = the load factor per the Fatigue I limit state defined in LTS-LRFD Table 3.4-1.
5. ϕ = the resistance factor equal to 1.0.

For galloping, natural wind gusts, truck-induced gusts, and high-mast wind-induced vibrations:

$$R = \begin{cases} 0.6 \frac{\zeta_c}{\zeta_u} & \text{for } R > 3 \\ 1 & \text{otherwise} \end{cases} \quad (7.2)$$

where:

1. ζ_c = damping ratio of the structure including the VMD.
2. ζ_u = damping ratio of the structure without the VMD.

ζ_c shall be determined as described in the damping device product documentation, consistent with the procedures described in LTS-LRFD Appendix E (2024 Interims). The ζ_c value used for each wind load type shall be consistent with the direction of vibration that the wind load induces.

The procedures used in the present work parallel those in Appendix E. ζ_u shall be equal to 0.2% unless experimentally determined values for the specific structure type being examined are available.

Although a mitigation device was not used in the present work, the directly embedded foundation exhibited significantly more damping than a typical pole supported by a baseplate, anchor bolts, and a reinforced drilled shaft. Table 7.1 provides R for various damping ratios in the ranges observed in the present work. A pole designed with a directly embedded foundation could see a decrease in stresses between 67% and 92% based on this work, and the base plate fatigue detail could be deleted.

Table 7.1 Effect of damping on fatigue loads

	Damping Ratio	R	Percent decrease in stresses
Typical structure	0.002	1	-
	0.01	3	67
Direct-embed tests	0.02	6	83
	0.03	9	89
	0.04	12	92

Although a significant advantage of the direct-embed foundation is that the most fatigue-prone details are eliminated, some will remain. For example, if a full-size handhole (access for the luminaire winch mechanism) is required, then it must be designed for fatigue. Alternatively, light fixture manufacturers are providing winch solutions that require only two small holes instead of one large hole. Typically, these are five in. by 7 in. and may or may not require reinforcement depending on the pole thickness. This hole size is much more fatigue resistant due to the decrease in the effective area.



Figure 7.7 Two 5"x7" unreinforced access holes (courtesy of WYDOT)

The damping R-factor is applied to this much-improved detail to reduce the propensity of fatigue cracking further. Note that the consideration of damping during the design could have resulted in the omission of reinforcement around the access hole and increased economy and performance. These two effects likely ensure outstanding fatigue performance for low-cycle fatigue. A similar detail is expected and required for wiring access and this hole is typically located below the groundline.

7.2.2 Large-amplitude Wind Events

The LTS-LRFD does not address wind events that create large-amplitude motions due to galloping. Many failures have occurred in recent decades due to these relatively rare events. Unlike the fatigue behavior, these events create large stresses, often exceeding yield. Failures typically occur due to cracking near the welds. Figure 7.8 illustrates one of several poles located along I-15 in Utah. Similar cases have occurred in Nebraska, Kansas, Iowa, and elsewhere. Note that the 30-ft tip translation was scaled from video movement, given the known pole height and luminaire circle diameter.



Figure 7.8 Pole translation in a galloping event (courtesy Utah DOT)

DOTs have recently upsized their pole thicknesses and downsized the pole heights to address this phenomenon. For example, NDOT, Kansas DOT, and Wyoming DOT use 80-ft poles for their standards. Kansas and Wyoming use thicknesses of 0.5, 0.375, and 0.3125 in. for the three pole sections. Although prudent, these geometric improvements theoretically do not address the case of galloping, where resonance occurs between the loads applied and the natural frequency of the pole.

Figure 7.9 illustrates the translation of a 16-sided pole in a wind tunnel. Note that at low velocity, the sections move with traditional vortex-induced shedding; however, the movements are small relative to the galloping resonance behavior that occurs at a much higher velocity, in this case, approximately 33 mph (15 m/s). This is typical of in-service pole failure observed, i.e., the winds are strong but not close to the design wind speeds for strength.

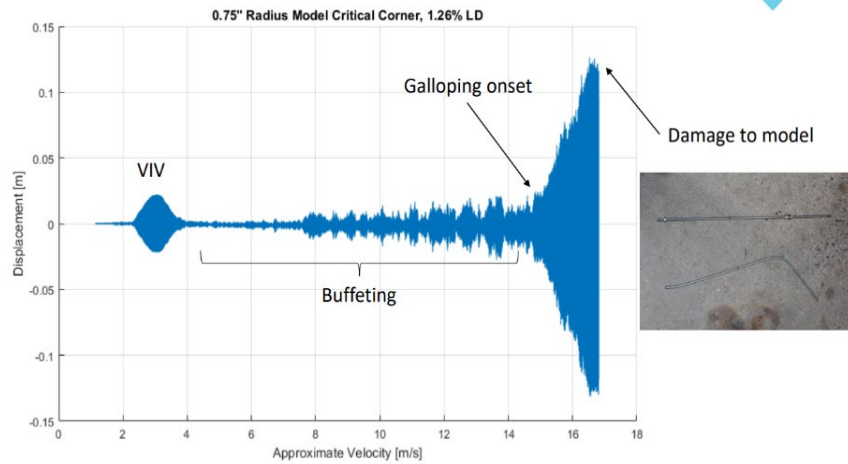


Figure 7.9 Wind-tunnel testing of a multisided pole section (courtesy of WYDOT)

It is possible to compute the onset velocity where the pole will begin large movements, called the onset critical velocity (European Committee for Standardization, 2005).

$$V_{crit} = \frac{2S_c f_n b}{a_G} \quad (7.3)$$

where S_c is the Scouton number, a_G is a factor for galloping instability = 1.0 for a cylinder, b is a characteristic section width, typically diameter, and f_n is the structure's natural frequency, in the first mode. The Scouton number is

$$S_c = \frac{2\delta m_e}{\rho b^2} \quad (7.4)$$

where δ is the log-dec damping ratio = $2\pi\zeta$, m_e , the equivalent model mass (a structural property), and ρ is the air density.

Note that damping is in the numerator, so an increase in damping proportionally increases the onset velocity. Thus, if damping can be increased to a level where the onset velocity is large, i.e., rare, the galloping phenomenon can be less likely. Damping can be improved with a VMD, or in the present work, damping that is inherent in the direct-embed foundation provides a significant increase in damping over past high-mast towers. This is one reason the directly embedded foundations are important – they could address the large amplitude vibration problems with a simple cost-effective solution.

For example, based on the observed damping for the gravel backfill foundations shown here ($\zeta = 0.01$, the lower observations of the concrete foundation), this foundation structure would result in an increase in the galloping onset velocity by 200% compared to experimentally observed damping in traditional foundation structures ($\zeta = 0.005$).

Chapter 8 Conclusions

8.1 Summary

This study investigated an alternative design method to eliminate the fatigue issues in high-mast luminaire supports used in the US transportation sector. Traditional high-mast luminaire towers are designed with a base plate detail connected with anchor bolts to a reinforced concrete foundation. This detail is known to cause various problems (cost, installation, bolt tightening/loosening, stress concentrations, etc.) that may result in fatigue cracking. The research team has investigated an alternative method that involves directly installing the pole into a foundation shaft and backfilling with concrete or gravel.

In this investigation, four poles were designed, constructed, and tested. Two foundations with concrete backfill and two with gravel backfill were investigated. Based on the design investigations, the pole depth for the site conditions was selected such that a 12-ft deep shaft would likely be insufficient to provide fixity at design loads, and a 16-ft shaft would be sufficient. These selections were intended to obtain relevant information from the two conditions for future designs. All shaft diameters were 36 in.

The testing program consisted of static and dynamic tests executed in two opposite directions to observe potential hysteresis. Three dynamic pluck tests were conducted in one direction, followed by three static tests near the 3000-year design moment. Damping information, static load testing information, and hysteretic behavior were observed. Additionally, forced vibration was used to excite the pole over a range of frequencies at the beginning and end of the load tests. The first three modes of vibration were observed. The load direction was then moved to the opposite direction, and all tests were repeated. LPILE and SAP2000TM analyses were performed to investigate the design process and predict their performance.

Design recommendations are outlined, including Brom's method and p-y curve analysis. Service I limit state will not control. Extreme I load should be checked against the soil resistances, and the groundline translation should be limited to 0.75 inches.

Appendix F provides installation instructions, and this appendix is intended to become a standalone document with the final draft written by NDOT.

8.2 Conclusions

The following conclusions were made based on the static load testing and subsequent modeling:

- The static load test indicated that poles with concrete backfill initially exhibited significantly higher stiffness compared to those with gravel backfill. For example, the 16-Concrete pole decreased from 29.13 kip/in. to 18.76 kip/in. in the NW direction, and from 21.90 kip/in. to 14.76 kip/in. in the SE direction. The 12-Concrete pole had stiffness reduced from 16.51 kip/in to 10.25 kip/in. in the NE direction and from 13.72 kip/in to 10.39 kip/in. in the SW direction.

- While the concrete backfill poles experienced a considerable reduction in stiffness with repeated static testing, the gravel backfill poles maintained relatively constant stiffness and demonstrated potential self-healing behavior. For example, the stiffness of the 16-Gravel pole remained almost constant at around 7.50 kip/in. in the NE direction and was similar in the other direction. The same behavior was observed on the 12-Gravel pole. This highlights the importance of considering backfill material in the design of pole foundations, particularly in terms of long-term performance and stability under varying load conditions.
- The robustness and load-carrying capacity of the foundations were shown to exceed design requirements as all shafts were loaded above the expected 3000-year MRI moment.
- The hysteretic behavior of each pole illustrated relative stability with large load-carrying capacity in both directions and significant ductility without brittle or catastrophic failure.
- The study showed that the translation vs. depth behavior aligned with expectations and was similar to the LPILE analyses. It also showed that safe designs are possible using the methods presented herein.
- The 12-ft shafts had non-zero translation and rotation at the bottom of the shaft, indicating a need for deeper shafts to achieve zero translation and slope and are thus not recommended.
- The 16-ft shafts showed lower translations and nearly zero slopes at the bottom, suggesting that increasing embedment depth beyond 16 feet for the same diameter and loads would not significantly improve performance.

The following conclusions were made from the free vibration (pluck) tests:

- The backfill material significantly affected the free-vibration performance of poles, with gravel backfill resulting in higher damping ratios (average of 0.035) compared to concrete backfill (average of 0.013).
- The effect of embedment depth on damping performance was not consistent with the log-decrement damping. For example, the 16-Concrete had less damping than the 12-Concrete (compare the averages of 0.010 to 0.016, respectively) while the 16-Gravel had similar damping to the 12-Gravel (compare average of 0.0345 to 0.035, respectively).
- Damping was observed to be non-linear with respect to the amplitude of vibrations. However, for lower amplitude vibrations, the damping was larger than would be expected for a typical baseplate structure.
- All installations showed increased log-decrement damping compared to typical baseplate structures from the literature, often less than 0.005.

The following conclusions were made from the forced vibration tests and finite element modeling:

- Poles with concrete backfill experienced significant reductions in natural frequencies compared to gravel-backfilled poles. For example, for the 16–Concrete pole, the reduction was 2.25%, 20.54%, and 16.91% in the first, second, and third natural frequencies, respectively. While for the 16–Gravel pole, the maximum reduction observed was 2.17%.
- Deeper embedment depths generally resulted in higher natural frequencies due to increased system stiffness.

- For poles with concrete backfill, the difference between the experimental and FEA results was less than 10%; thus, using a round shaft with casing and core/insert for the foundation provided a good estimation of the natural frequencies.
- For poles with gravel backfill, two soil medium models were analyzed for each embedment depth as the LPILE cannot change the properties of the soil in the radial direction. Cases 3 and 4, where soil was the medium, showed the best predictions where the the maximum difference between the model and experiment was less than 10% and 17%, respectively. Based on these results, modeling with LPILE and FEA using boring report data for the interfacial medium provided reasonable foundation stiffness and natural frequencies estimates.

The above-listed conclusions indicated that the direct embed method can be designed for static loads in excess of the LTS-LRFD. However, other design concerns were the transient loads that induced fatigue or resonance problems. The following conclusions were based on the analysis of the findings related to increased damping:

- Due to the increased damping values measured, a pole could see a decrease in wind-induced fatigue stresses between 67% and 92% based on this work and remove the base plate fatigue detail completely.
- Combining the suggested handhold access holes with the direct embed system can eliminate fatigue issues at the base of high-mast towers.
- While the LTS-LRFD specification does not address large amplitude wind events due to galloping, using the process presented, an engineer could expect an increase in galloping onset velocity by 200%, greatly reducing the frequency of highly damaging galloping events.

References

- American Association of State Highway and Transportation Officials. (2015). *"LRFD Specifications for Structural Supports for Highway Signs, Luminaires, and Traffic Signals."* AASHTO.
- ASCE/SEI 72-21 (2021). *"Design of Steel Lighting Poles Structures,"* American Society of Civil Engineers, Reston, VA.
- Brown, D. A., Turner, J. P., Castelli, R. J., & Loehr, E. (2018). *"Drilled Shafts: Construction Procedures and Design Methods"*. NHI Course No. 132014. FHWA NHI-18-024. <https://rosap.ntl.bts.gov/view/dot/73033>
- Connor, R. J., Callahan, G., Koob, M. J., Hodgson, I. C., & Brakke, B. L. (2007). *"Field and Laboratory Studies on High-Mast Lighting Towers in Iowa"*. The 2007 Mid-Continent Transportation Research Symposium.
- CSI. (2024). *"SAP2000 Integrated Software for Structural Analysis and Design"*. Computers and Structures Inc.
- Ensoft Inc. (2022). *"LPILE"*.
- European Committee for Standardization. (2005). *"Eurocode 1: Actions on structures - Part 1-4: General actions - Wind actions"*. <https://doi.org/https://doi.org/10.3403/03252196U>
- Frymoyer, M., & Berman, J. (2010). *"Remaining life assessment of in-service luminaire support structures"*. <https://rosap.ntl.bts.gov/view/dot/17555>
- Nasouri, R., Nguyen, K., Montoya, A., Matamoros, A., Bennett, C., & Li, J. (2019). *"Simulating the hot dip galvanizing process of high mast illumination poles. Part I: Finite element model development"*. Journal of Constructional Steel Research, 162, 105705. <https://doi.org/10.1016/j.jcsr.2019.105705>
- Puckett, J., & Ahearn, E. B. (2010). *"Reduction of Wind-Induced Vibrations in High-Mast Light Poles"*.
- Sherman, R. J., & Connor, R. J. (2019). *"Development of a Fatigue Design Load for High-Mast Lighting Towers"*. Journal of Structural Engineering, 145(1). [https://doi.org/10.1061/\(ASCE\)ST.1943-541X.0002236](https://doi.org/10.1061/(ASCE)ST.1943-541X.0002236)
- Warpinski, M. K., Connor, R. J., & Hodgson, I. C. (2010). *"Influence of Flexibility on the Fatigue Performance of the Base Plate Connection in High-Mast Lighting Towers"*. Journal of Structural Engineering, 136(3), 324–329. [https://doi.org/10.1061/\(ASCE\)ST.1943-541X.114](https://doi.org/10.1061/(ASCE)ST.1943-541X.114)

Appendix A Early Design Computations (prior to establishing the shaft diameter and depths)

A.1 Problem Statement

This example outlines how the design calculations were approached prior to finalizing the shaft diameter and depths.

A.2 Concrete and Gravel Backfills

The first step for shaft design is obtaining a borehole report and the layered material properties required for P-Y analysis using LPILE. For this report, a borehole report was obtained for a depth of 25 ft below the ground surface showing the material description and classification, N-value, thickness, and depth for each layer as shown in Figure A.1 and Table A.1. These properties are necessary to run P-Y analysis. Moreover, additional properties are needed based on the material type such as effective unit weight, cohesion for clay soil and friction angle for sandy soil.

In this study, four poles were investigated with different backfill materials and embedment depths, the properties of these poles at ground level were almost the same. The poles and shaft properties at the top of each shaft are shown in Table A.3. The NDOT's new standard 80-ft pole, extreme limit state, and service limit state reactions are shown in Table A.4.

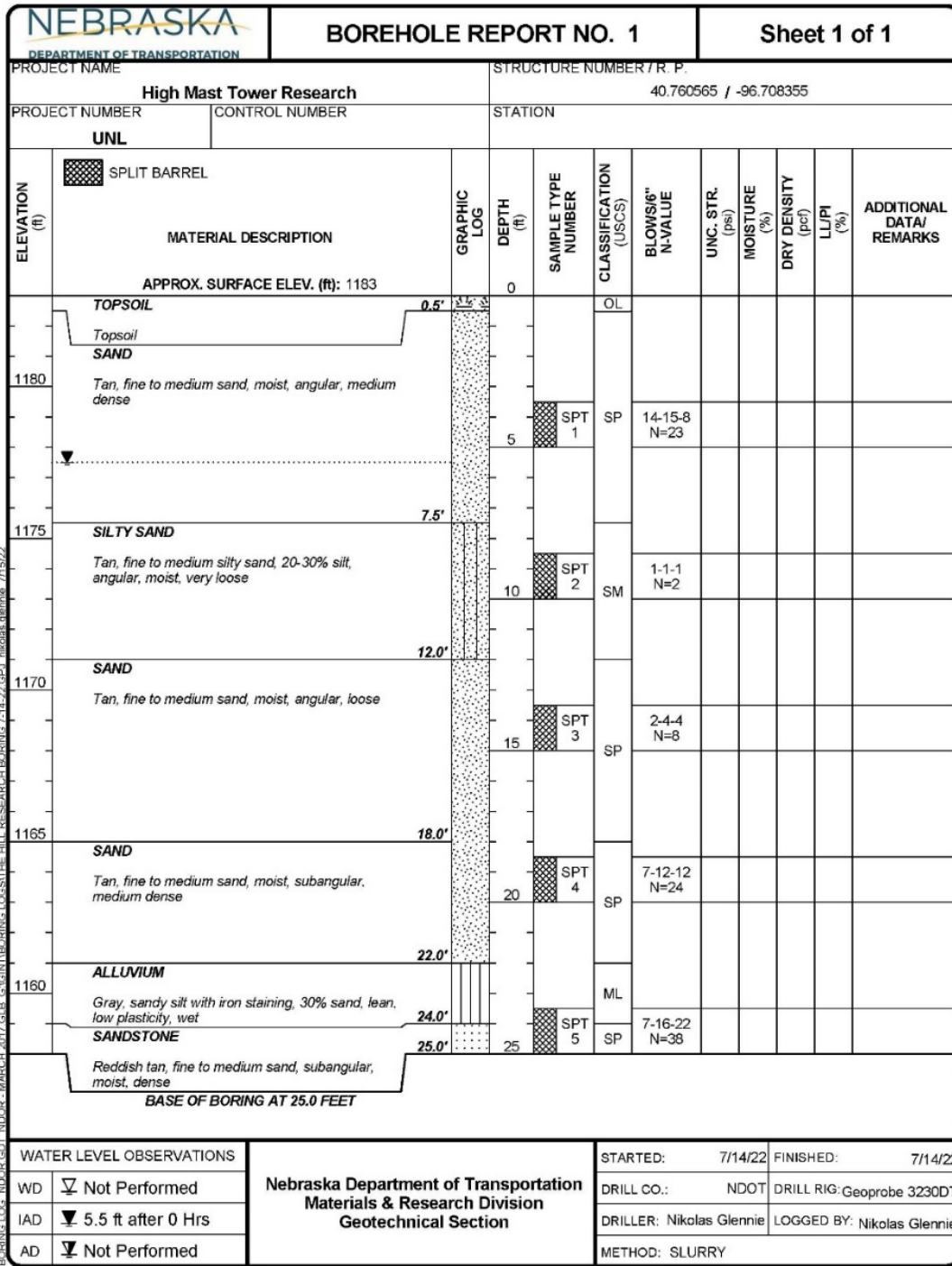


Figure A.1 Borehole report

Table A.1 Summary of geomaterial layer thicknesses and types

Layer No.	Elevation at the top of the layer (ft)	Elevation at the bottom of the layer (ft)	Thickness (ft)	Geomaterial type
1	0	7.5	7.5	Cohesionless soil
2	7.5	12	4.5	Cohesionless soil
3	12	18	6	Cohesionless soil
4	18	22	4	Cohesionless soil
5	22	24	2	Cohesionless soil
6	24	25	1	Cohesionless soil

Table A.2 Soil layers with N-value data

Layer No.	Unit weight (pcf)	N-value	Depth at N (ft)
1	124	23	4
2	130	2	9
3	124	8	14
4	124	24	19
5	124	38	24
6	124	38	24

Table A.3 The poles and shafts properties at the top of each shaft

Pole	Dia. (in)	Thickness (in)	Elastic Modulus (ksi)	Embedment length (ft)	Backfill material	Shaft Dia. (in)
16 – Concrete	16.4	0.26	29000	16	Concrete	36
16 – Gravel	18.9	0.26	29000	16	Gravel	36
12 – Concrete	17.2	0.28	29000	12	Concrete	36
12 – Gravel	15.8	0.25	29000	12	Gravel	36

Table A.4 Summary of factored load demands (700-yr MRI)

Load	Service I	Extreme I
Axial (kips)	4.18	4.18
Shear (kips)	1.73	3.07
Moment (ft-kips)	89.8	159.6

A.3 Concrete Backfill Shaft Design

The design aims to determine the shaft diameter and depth to satisfy the design requirements according to the NDOT's new standard 80-ft pole mentioned previously. For that purpose the diameter of the shaft was assumed to be 3 ft with a concrete backfill and was checked to make sure it could achieve the axial load demand.

A.3.1 Side resistance

The nominal side resistance for all geomaterial layers through which the trial shaft extends is calculated. The following calculations show the procedure to find the factored side resistance for layer No.1, the same procedure was repeated for all layers. All the results are shown in Table A.5.

1. *The effective vertical stress, $\sigma_v = \text{Unit weight} * \text{Depth of } N = 124 * 4 = 496 \text{ psf}$*
2. *The corrected $N - \text{value}, (N_1)_{60} = N_{60} \left(\frac{P_a}{\sigma_v}\right)^{0.5} = 23 * \left(\frac{2088}{496}\right)^{0.5} = 47.2$*
3. *Angle of friction, $\phi' = 27.5 + 9.2 * \log((N_1)_{60}) = 27.5 + 9.2 * \log(47.2) = 42.9 \text{ degrees, assume } 40 \text{ degree}$*
4. *Preconsolidation stress, $\sigma_p = P_a * 0.47 * N_{60}^{0.6} = 2088 * 0.47 * 23^{0.6} = 6439.7 \text{ psf}$*
5. *Over consolidation ratio, $OCR = \frac{\sigma_p}{\sigma_v} = \frac{6439.7}{496} = 13$*
6. *$k_0 = (1 - \sin\phi) * OCR^{\sin\phi} = (1 - \sin 40) * 13^{\sin 40} = 1.9$*
7. *$k_p = \left(\tan\left(45 + \frac{\phi}{2}\right)\right)^2 = \tan^2\left(45 + \frac{40}{2}\right) = 4.6$*
8. *First check: $k_0 < k_p$ Good*
9. *$\beta = k_0 * \tan\phi = 1.9 * \tan 40 = 1.6$*
10. *Nominal unit side resistance, $f_{SN} = \beta * \sigma_v = 1.6 * 496 = 772.5 \text{ lb}$*
11. *Nominal side resistance factor, $R_{SN} = f_{SN} * \pi * B * \Delta = 772.5 * 3.14 * 3 * 7.5 = 54576.2 \text{ lb}$*
12. *$\phi R_{SN} = 0.55 * 54576.2 = 30016.9 \text{ lb}$*

Table A.5 Calculations for axial compressive resistance - Side resistance

Layer No.	1	2	3	4	5	6
σ_v (psf)	496	906.5	1232.3	1540.6	1848.6	1848.6
$(N_1)_{60}$	47.2	3.0	10.4	27.9	40.4	40.4
ϕ'	40	31.9	36.9	40.8	42.3	42.3
σ_p (psf)	6439.7	1487.5	3417.3	6606.3	8703.6	8703.6
OCR	13.0	1.6	2.8	4.3	4.7	4.7
k_0	1.9	0.6	0.7	0.9	0.9	0.9
k_p	4.6	3.2	4.0	4.8	5.1	5.1
$k_0 < k_p$	Yes	Yes	Yes	Yes	Yes	Yes
β	1.6	0.4	0.6	0.8	0.8	0.8
f_{SN} (Ib)	772.5	345.9	681.7	1193.3	1559.8	1559.8
R_{SN} (Ib)	54576.2	14660.9	38527.5	44965.2	29386.6	14693.3
ϕR_{SN} (Ib)	30016.9	8063.5	21190.1	24730.9	16162.6	8081.3

A.3.2 Base resistance

Base resistance was calculated for all layers. The following calculations show the procedure to find the factored base resistance for layer No.1, same procedure was followed for all layers. All the results are shown in Table A.6.

- 1) Nominal unit base resistance, $q_{BN} = 0.6 * N_{60} = 0.6 * 23 = 13.8 \text{ tsf} = 27.6 \text{ k/ft}^2$
- 2) Nominal base resistance, $R_{BN} = \frac{\pi}{4} * B^2 * q_{BN} = \frac{3.14}{4} * 3^2 * 27.6 = 195 \text{ kips}$
- 3) Factored base resistance, $\phi R_{BN} = 0.5 * 195 = 97.5 \text{ kips}$

Table A.6 Calculations for axial compressive resistance - Base resistance

Layer	N-value	R _{BN} (kips)	Factored R _{BN} (kips)
1.0	23.0	195.0	97.5
2.0	2.0	17.0	8.5
3.0	8.0	67.8	33.9
4.0	24.0	203.5	101.7
5.0	38.0	322.2	161.1
6.0	38.0	322.2	161.1

A.3.3 Factored resistance

Now the trial embedment depths were 12 and 16 ft. The sum of factored resistances computed in Appendix A is found for each depth; these results are shown in Table A.7. The results show that the sum of resistance for each depth is much larger than the factored axial load applied at the pile. Therefore, all the depths satisfy the requirements for geotechnical axial compression.

Table A.7 Factored resistance calculations for shafts with concrete backfill

Embedment depth case (ft)	Sum of resistance (kips)	Factored axial load	Safe
12	71.98	4.18	Yes
16	86.1	4.18	Yes

A.3.4 Settlement check

The tolerable settlement of 1 inch is assumed. This check was found for each embedment depth as shown in Table A.8. The fill material was assumed to be concrete with a unit weight of 145 lb/ft³. The resistance corresponding to a downward translation of 1 inch for 12-ft embedment depth can be estimated as follows:

1. *Failure threshold* = $R_{SN} + R_{BN} = \frac{54576.2+14660.8+67.8*1000}{1000} = 137 \text{ kips}$
2. *Normalized displacement* = $\frac{\Delta}{B} * 100\% = \frac{1}{3*12} * 100\% = 2.8\%$
3. *Normalized test load from Figure 1* = 85% approximate
4. *Test load* = $\frac{85}{100} * 137 = 116.5 \text{ kips}$
5. *Area of steel* = $\frac{3.14}{4} * (20^2 - 19.73^2) = 8.4 \text{ in}^2$ "approximate"
6. *Weight of steel* = $\frac{8.4*(0.283-0.0361)*5*12+8.4*0.283*(12-5)*12}{1000} = 0.3 \text{ kips}$ approximate
7. *Area of filled area* = $\frac{3.14}{4} * (36^2 - 20^2) = 703.4 \text{ in}^2$
8. *Fill weight* = $\frac{(703.4*(12-5)*\frac{145-62.4}{12^2})+(703.4*5*\frac{145}{12^2})}{1000} = 6.4 \text{ kips}$
9. *Total weight* = $6.4 + 0.3 = 6.7 \text{ kips}$
10. $R_{service} = \text{Test load} - \text{Total weight} = 116.5 - 6.7 = 109.8 \text{ kips}$
11. $R_{service} > \text{Factored axial load, Good}$

Table A.8 Failure threshold calculations for all trial depths for shafts with concrete backfill

Embedment Depth Case (ft)	12	16
Failure threshold (kip)	137	162.7
Normalized translation	2.8	2.8
Normalized test load %	85	85
Test load (kip)	116.5	138.3
Steel area (in ²)	8.4	8.4
Steel weight (kip)	0.3	0.4
Fill area (in ²)	703.4	703.4
Fill weight (kip)	6.4	8.0
Total weight (kip)	6.7	8.3
R	109.8	130.0
Safe	Yes	Yes

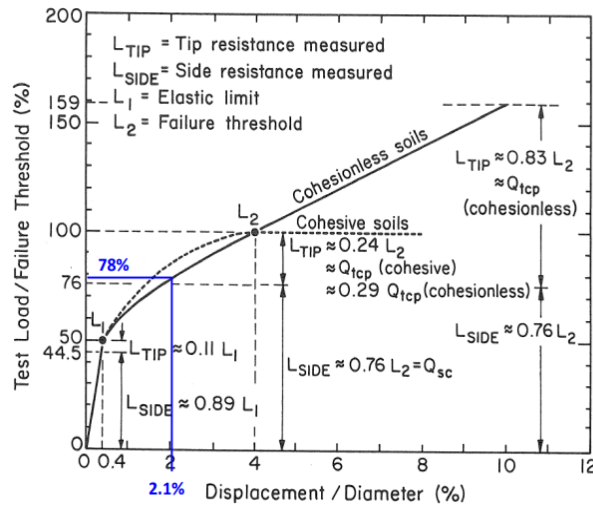


Figure A.2 Normalized load-translation curve

The results showed that the assumed shaft diameter with either 12- or 16-ft embedment depths were safe with respect to axial strength and settlement check, as the factored axial resistance was larger than the factored axial load demand for both cases.

A.3.5 P-Y Analysis

LPILE was used to perform a p-y analysis to identify the soil-structure interaction to predict the behavior of the soil-structure interaction under different loading conditions. To do so, different cases were established, considering embedment length, backfill type, and the medium around the foundation; these cases are shown in Table A.9.

Table A.9 Investigated cases using LPILE for shafts with concrete backfill

Case	Embedment Depth, ft	Foundation Properties	Medium Around the Foundation
1	16	Round Shaft with Casing and Core/insert	Soil
2	12	Round Shaft with Casing and Core/insert	Soil

Case 1 and Case 2 simulated the pole foundation with concrete backfill. The casing's outside diameter was set to 36 inches with a 0-inch thickness, and it was assumed to be filled with concrete. The concrete compressive strength was 4000 psi, and it was not filled inside the core as the concrete did not go inside the pole. The core diameter and thickness were the diameter and thickness of the pole, respectively. The elastic modulus was assumed to be 29000 ksi, while the yield stress was 50 ksi. Eight sections were used to simulate the pole's taper, each section was two feet long, and the reduction rate in the diameter was 0.14 inches per foot.

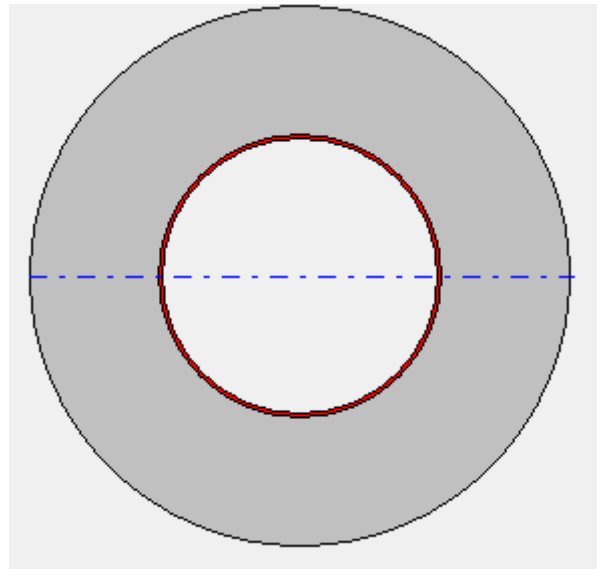


Figure A.3 Round Shaft with Casing and Core/insert

The pushover analysis is conducted by applying shear and moment in increments up to maximum values of $1/\phi$ times the factored demands, where ϕ = resistance factor. $\phi = 0.67$, equivalent to multiplying the factored demands by 1.5. For this analysis, the lateral load and moment were applied in multiples of 0.25 up to 1.5 times the factored values. The actual load

combinations and resulting lateral head translation values from the LPILE output are summarized in Table A.10. The results show that the head translation decreases as the embedment depth increases from 12 ft to 16 ft for both cases, the maximum head translation was 0.25 inch.

To illustrate the minimum shaft depth required to provide adequate pushover stability, additional p - y analyses were conducted with all parameters held constant except shaft depth as shown in Figure A.4. For a shaft depth of 16 ft, the load-translation behavior is still approximately linear, and stable up to 1.5 times the factored force. However, for a depth of 12 ft, the load translation curve shows a nonlinear trend at higher loads, suggesting the onset of instability against overturning.

Table A.10 Loading and computed head deflection translations for round shaft case

12 ft				
Load Increment	Multiple	Shear Force (kips)	Moment (ft-kips)	Head Translation (in)
1	0.25	0.767	39.9	0.026
2	0.5	1.535	79.8	0.054
3	0.75	2.302	119.7	0.082
4	1	3.07	159.6	0.110
5	1.25	3.837	199.5	0.180
6	1.5	4.605	239.4	0.250
16 ft				
1	0.25	0.8	39.9	0.014
2	0.5	1.5	79.8	0.027
3	0.75	2.3	119.7	0.042
4	1	3.1	159.6	0.055
5	1.25	3.8	199.5	0.110
6	1.5	4.6	239.4	0.152

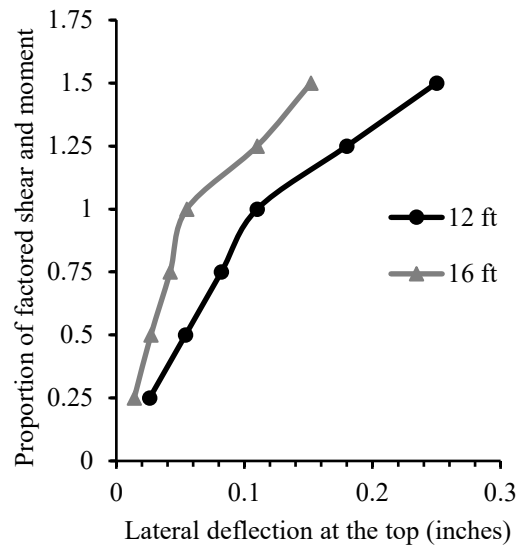


Figure A.4 Lateral translation at the top with loads increments for round shaft case

A.3.6 Comparison between P-Y analysis and Limited Groundline translations

Appendix G contains a discussion on service deflection limits indicating they are not a concern for the current NDOT designs with respect to the drilled shaft foundations. In the testing outlined in the report's body, groundline translations at the ultimate can be calculated using the P-Y analysis. Limiting the design translations to those observed during testing – considering their adequate performance – is a reasonable limit considering the extreme displacements and loads imposed. Observations at the 3000-year load level (first cycle) showed approximately 0.2 in. displacement for concrete shafts and 0.8 in. displacement for the gravel shafts with both undergoing considerable additional cycling. Displacement could be limited to this observed value or approximately 0.75 due to the performance. This selection is a judgment call for the NDOT designer.

A.4 Gravel Backfill Shaft Design

The design aims to determine the shaft diameter and depth to satisfy the design requirements according to the NDOT's new standard 80-ft pole mentioned previously. For that purpose, the diameter of the shaft was assumed to be 3 ft with gravel as backfill material and was checked to make sure it could achieve the axial load demand.

A.4.1 Factored resistance

The same trial embedment depths used in concrete backfill poles were assumed here 12 and 16 ft. The summation of factored resistances computed in the previous section was found for each depth, which is shown in Table A.11. The results show that the sum of resistance for each depth was much larger than the factored axial load applied at the pile. Therefore, all the depths satisfy the requirements for geotechnical axial compression.

Table A.11 Factored resistance calculations for shafts with gravel backfill

Embedment depth case (ft)	Sum of resistance (kips)	Factored axial load	Safe
12	71.98	4.18	Yes
16	86.1	4.18	Yes

A.4.2 Settlement check

A tolerable settlement of 1 inch was assumed. This check was found for each embedment depth, as shown in Table A.12. The fill material was assumed to be aggregate with a unit weight of 160 lb/ft³. The resistance corresponding to a downward translation of 1 inch for 12-ft embedment depth can be estimated as follows:

12. *Failure threshold* = $R_{SN} + R_{BN} = \frac{54576.2+14660.8+67.8*1000}{1000} = 137 \text{ kips}$
13. *Normalized displacement* = $\frac{\Delta}{B} * 100\% = \frac{1}{3*12} * 100\% = 2.8\%$
14. *Normalized test load from Figure 1* = 85% approximate
15. *Test load* = $\frac{85}{100} * 137 = 116.5 \text{ kips}$
16. *Area of steel* = $\frac{3.14}{4} * (20^2 - 19.73^2) = 8.4 \text{ in}^2$ "approximate"
17. *Weight of steel* = $\frac{8.4*(0.283-0.0361)*5*12+8.4*0.283*(12-5)*12}{1000} = 0.3 \text{ kips}$ approximate
18. *Area of filled area* = $\frac{3.14}{4} * (36^2 - 20^2) = 703.4 \text{ in}^2$
19. *Fill weight* = $\frac{(703.4*(10-5)*\frac{160-62.4}{12^2})+(703.4*5*\frac{160}{12^2})}{1000} = 6.3 \text{ kips}$
20. *Total weight* = 6.3 + 0.3 = 6.6 kips
21. $R_{service} = \text{Test load} - \text{Total weight} = 116.48 - 6.6 = 109.9 \text{ kips}$
22. $R_{service} > \text{Factored axial load}$, Good

Table A.12 Failure threshold calculations for all trial depths for shafts with concrete backfill

Embedment Depth Case (ft)	12	16
Failure threshold (kip)	137	162.7
Normalized translation	2.8	2.8
Normalized test load %	85	85
Test load (kip)	116.5	138.3
Steel area (in2)	8.4	8.4
Steel weight (kip)	0.3	0.4
Fill area (in2)	703.4	703.4
Fill weight (kip)	6.3	8.7
Total weight (kip)	6.6	9.1
R	109.9	131.7
Safe	Yes	Yes

The results showed that the assumed shaft diameter with either 12- or 16-ft embedment depths were safe with respect to axial strength and settlement check, as the factored axial resistance was larger than the factored axial load demand for both cases.

A.4.3 P-Analysis

LPILE was used to perform a p-y analysis that identified the soil-structure interaction and predicted the behavior of the soil under different loading conditions. Different cases were established considering embedment length, backfill type, and the medium around the foundation, shown in Table A.13.

Table A.13 Investigated cases using LPILE for shafts with gravel backfill

Case	Embedment Depth, ft	Foundation Properties	Medium Around the Foundation
3	16	Steel Pipe Section	Soil
4	12	Steel Pipe Section	Soil

The LPILE cannot change the properties of the soil in the radial direction; thus, the pole with gravel backfill cannot be simulated directly. Because of that, Case 3 and Case 4 assumed that the medium around the pole foundation was soil.

The pushover analysis was conducted by applying shear and moment increments up to maximum values of $1/\phi$ times the factored demands, where ϕ = resistance factor = 0.67, equivalent to multiplying the factored demands by 1.5. For this analysis, the lateral load and moment were applied in multiples of 0.25 up to 1.5 times the factored values. The actual load combinations and resulting lateral head translation values from the LPILE output are summarized in Table A.14. The results show that the head translation decreased as the embedment depth increased from 12 ft to 16 ft for both cases, the maximum head translation was 0.653.

To illustrate the minimum shaft depth required to provide adequate pushover stability, additional *p-y* analyses were conducted with all parameters held constant except shaft depth, as shown in Figure A. 5. For a shaft depth of 16 ft, the load-translation behavior was approximately linear and stable up to 1.5 times the factored force effects for the steel pipe and drilled shaft cases. However, for a depth of 12 ft, the load translation curve showed a nonlinear trend at higher loads, suggesting the onset of instability against overturning.

Table A.14 Loading and computed head deflection translations for steel pipe case

12 ft				
Load Increment	Multiple	Shear Force (kips)	Moment (ft-kips)	Head Translation (in)
1	0.25	0.7675	39.9	0.060
2	0.5	1.535	79.8	0.134
3	0.75	2.3025	119.7	0.231
4	1	3.07	159.6	0.350
5	1.25	3.8375	199.5	0.490
6	1.5	4.605	239.4	0.653
16 ft				
1	0.25	0.8	39.9	0.057
2	0.5	1.5	79.8	0.125
3	0.75	2.3	119.7	0.210
4	1	3.1	159.6	0.310
5	1.25	3.8	199.5	0.417
6	1.5	4.6	239.4	0.537

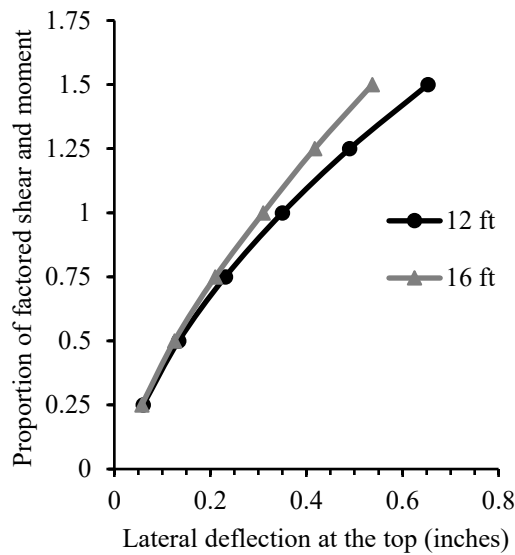


Figure A. 5 Lateral translation at the top with loads increments for steel pipe case

A.4.4 Comparison between P-Y analysis and Limited Groundline translations

Appendix G contains a discussion on service deflection limits indicating they are not a concern for the current NDOT designs with respect to the drilled shaft foundations. In the testing that was reported in the body of the report, groundline translations at ultimate can be calculated using the P-Y analysis. Limiting the design translations to those observed during testing – considering their adequate performance – is a reasonable limit considering the extreme displacements and loads imposed. Observations at the 3000-year load level (first cycle) showed approximately 0.2 in. displacement for concrete shafts and 0.8 in. displacement for the gravel shafts with both undergoing considerable additional cycling. Based on testing and judgment, a conservative groundline translation of 0.75 inch could be used to design the drilled shaft for both concrete or gravel backfills.

Appendix B Force Vibration Response via FFT

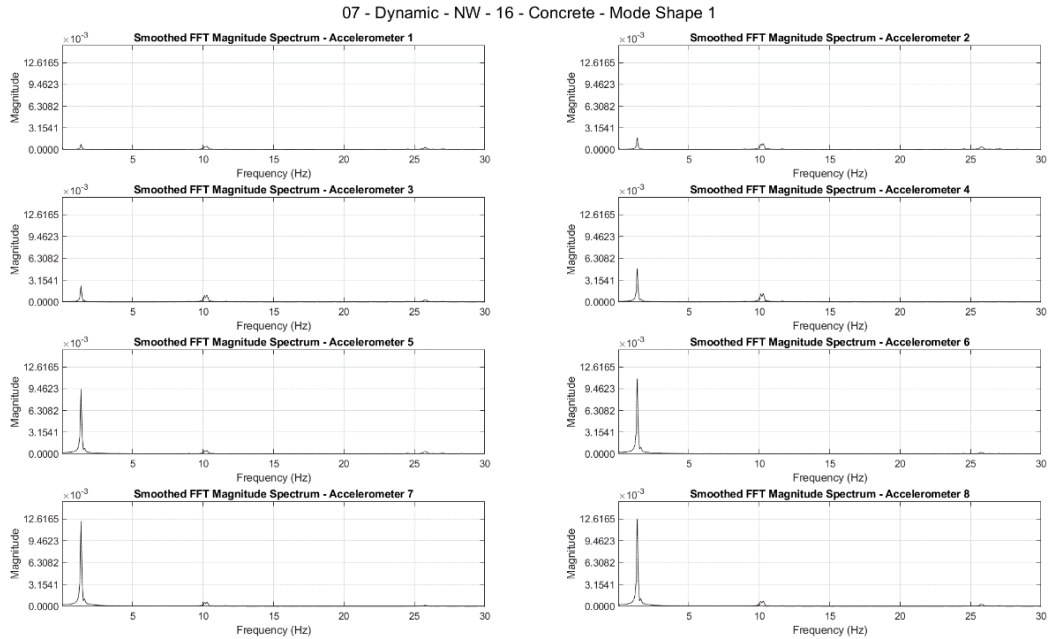


Figure B.1 The results of FFT of the forced vibration test performed on the NW direction on Pole 16-Concrete showing the natural frequency of first mode shape

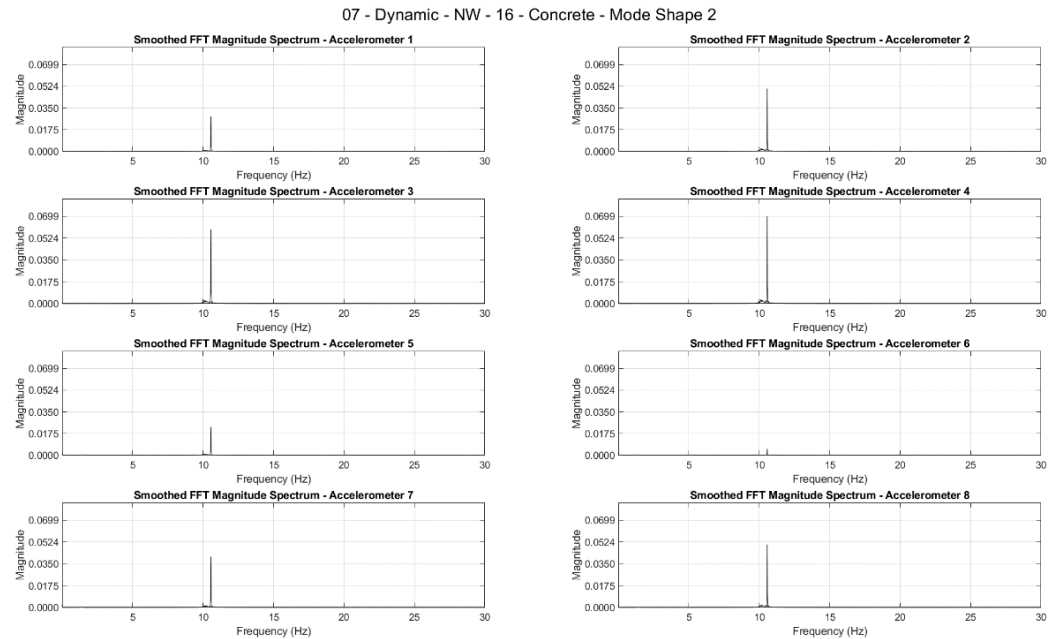


Figure B.2 The results of FFT of the forced vibration test performed in the NW direction on Pole 16-Concrete showing the natural frequency of the second mode shape

07 - Dynamic - NW - 16 - Concrete - Mode Shape 3

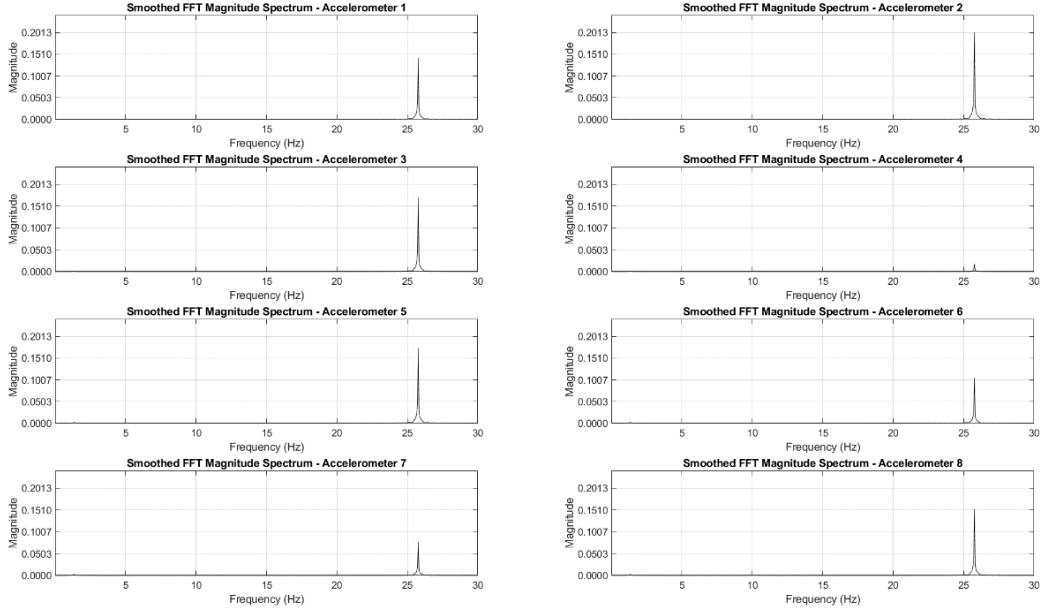


Figure B.3 The results of FFT of the forced vibration test performed in the NW direction on Pole 16-Concrete showing the natural frequency of the third mode shape

14 - Dynamic - SE - 16 - Concrete - Mode Shape 1

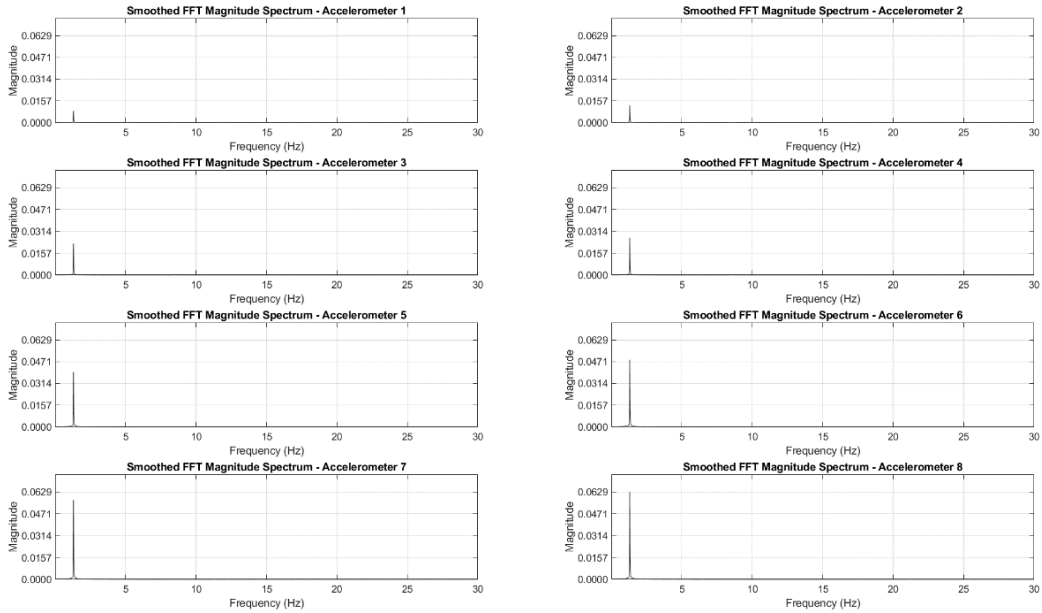


Figure B.4 The results of FFT of the forced vibration test performed in the SE direction on Pole 16-Concrete showing the natural frequency of the first mode shape

14 - Dynamic - SE - 16 - Concrete - Mode Shape 2

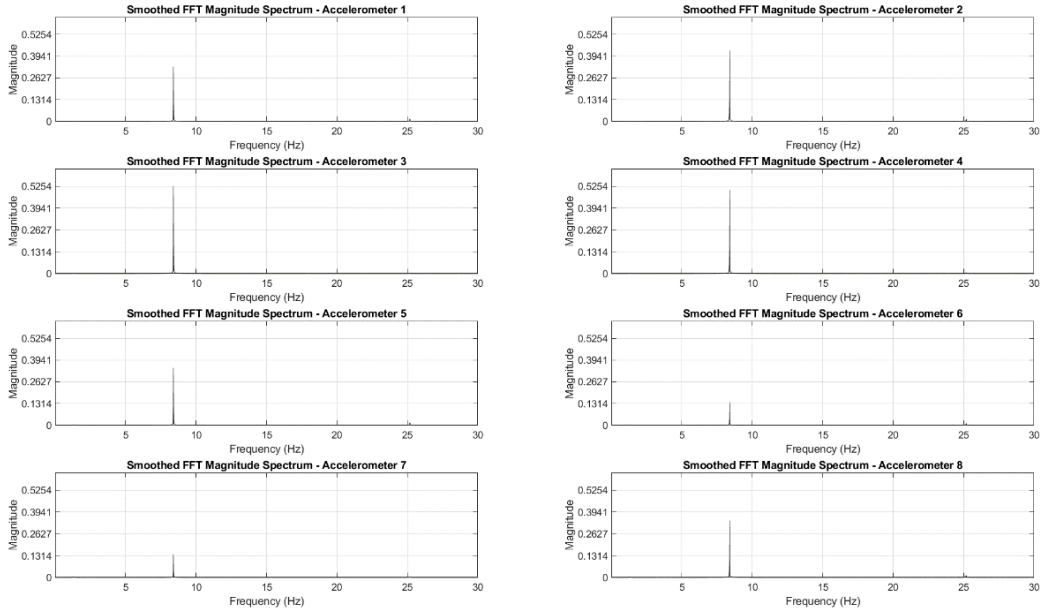


Figure B.5 The results of FFT of the forced vibration test performed on the SE direction in Pole 16-Concrete showing the natural frequency of the second mode shape

14 - Dynamic - SE - 16 - Concrete - Mode Shape 3

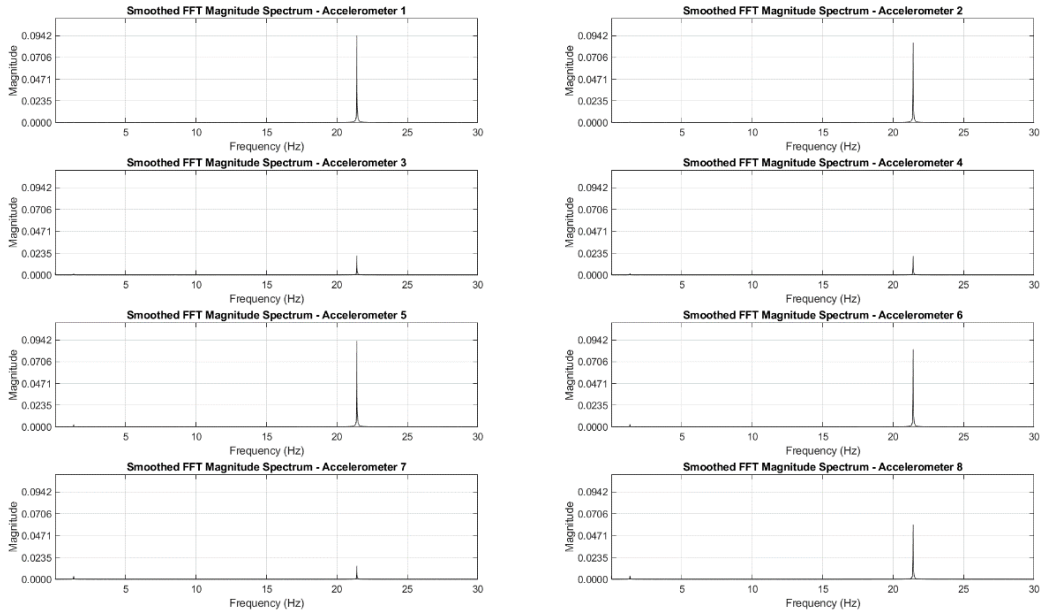


Figure B.6 The results of FFT of the forced vibration test performed on the SE direction in Pole 16-Concrete showing the natural frequency of the third mode shape

21 - Dynamic - NE - 16 - Gravel - Mode Shape 1

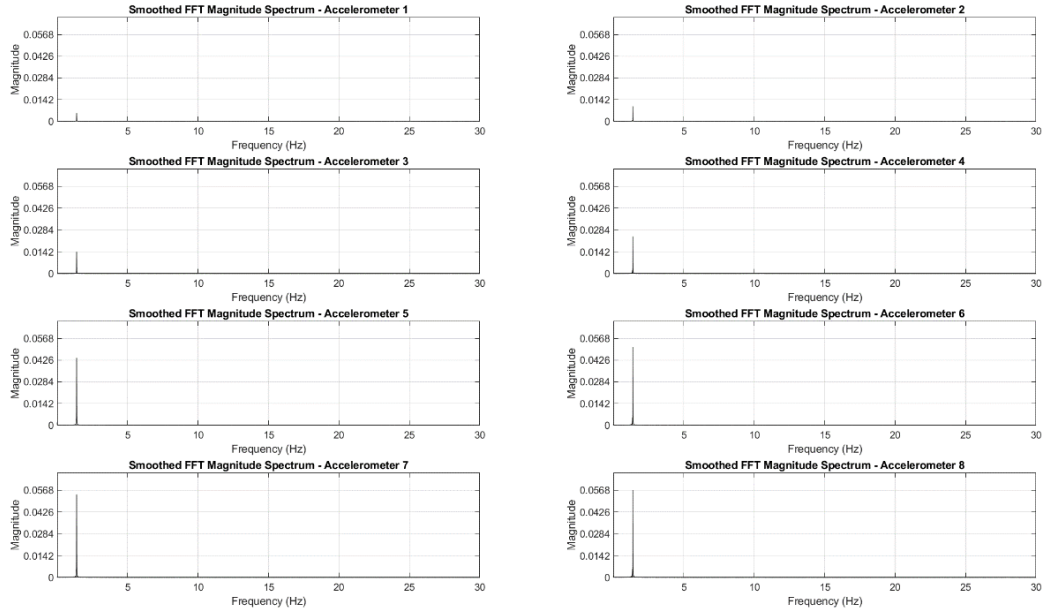


Figure B.7 The results of FFT of the forced vibration test performed on the NE direction on Pole 16-Gravel showing the natural frequency of first mode shape

21 - Dynamic - NE - 16 - Gravel - Mode Shape 2

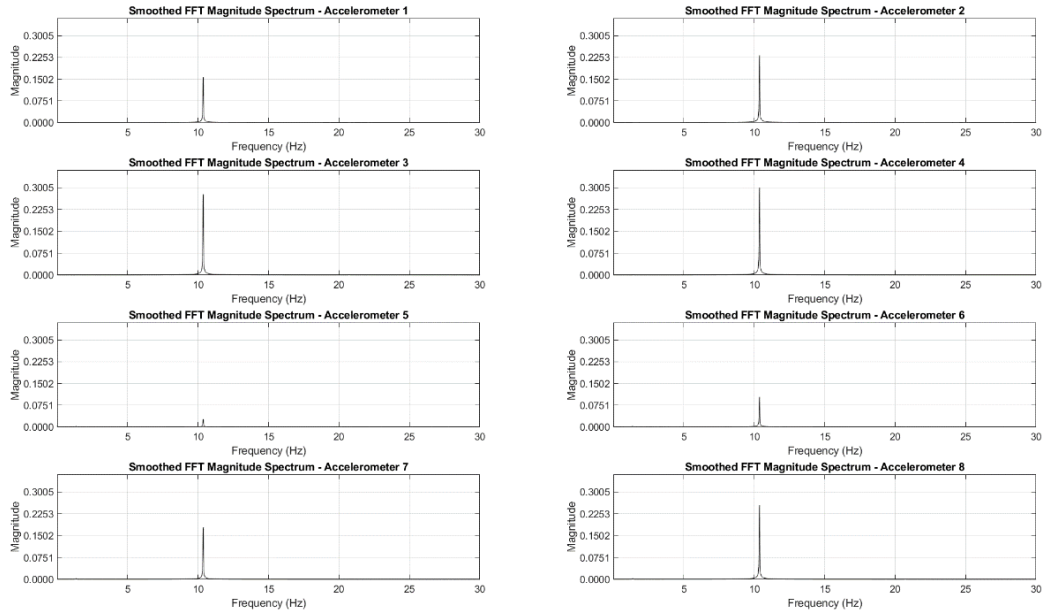


Figure B.8 The results of FFT of the forced vibration test performed in the NE direction on Pole 16-Gravel showing the natural frequency of the second mode shape

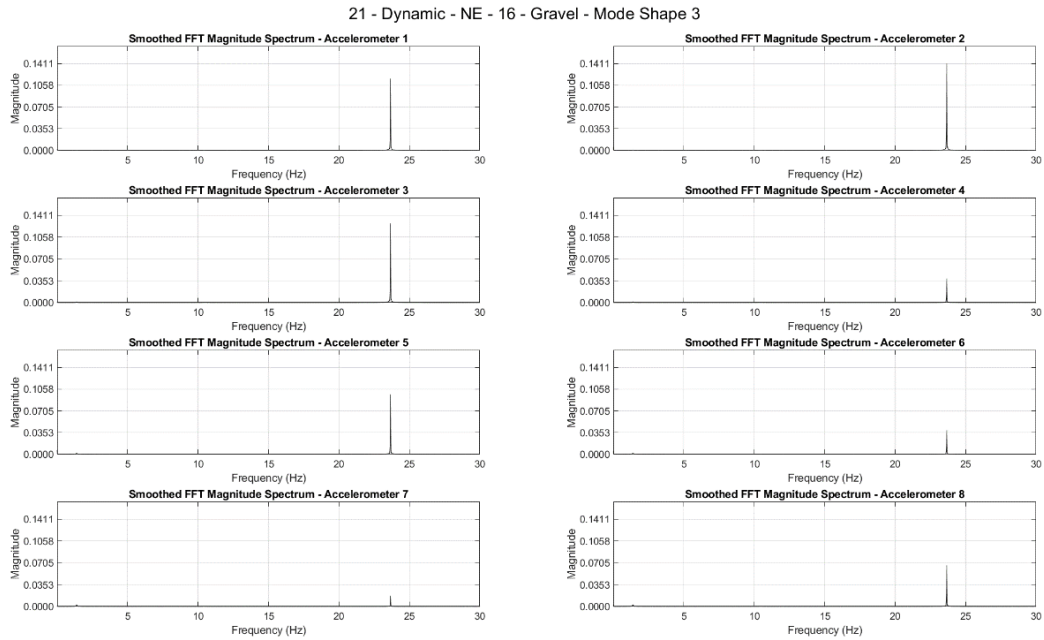


Figure B.9 The results of FFT of the forced vibration test performed in the NE direction on Pole 16-Gravel showing the natural frequency of the third mode shape

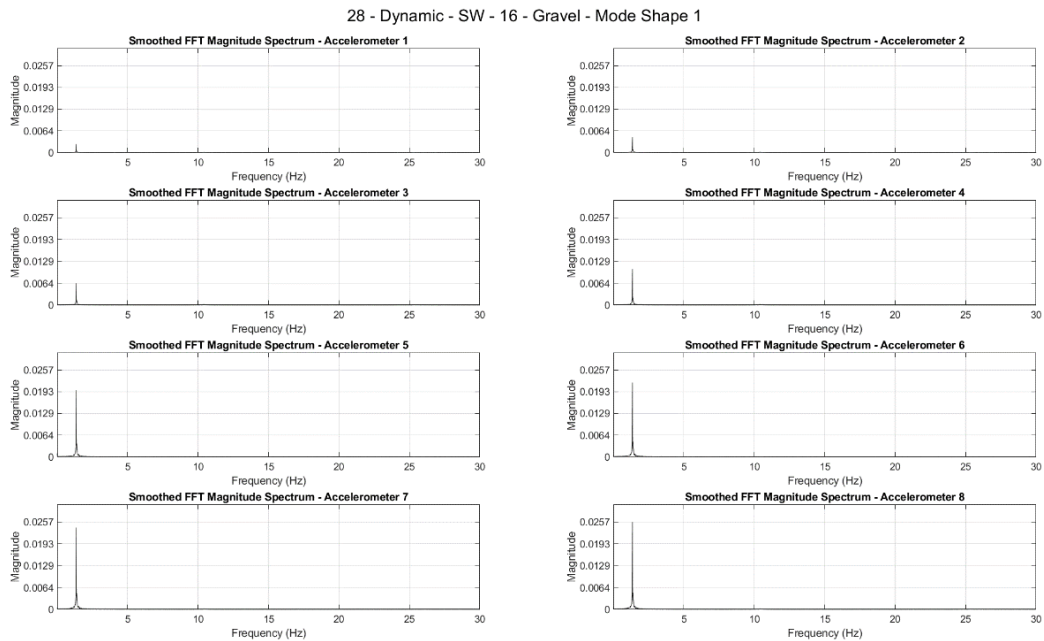


Figure B.10 The results of FFT of the forced vibration test performed in the SW direction on Pole 16-Gravel showing the natural frequency of the first mode shape

28 - Dynamic - SW - 16 - Gravel - Mode Shape 2

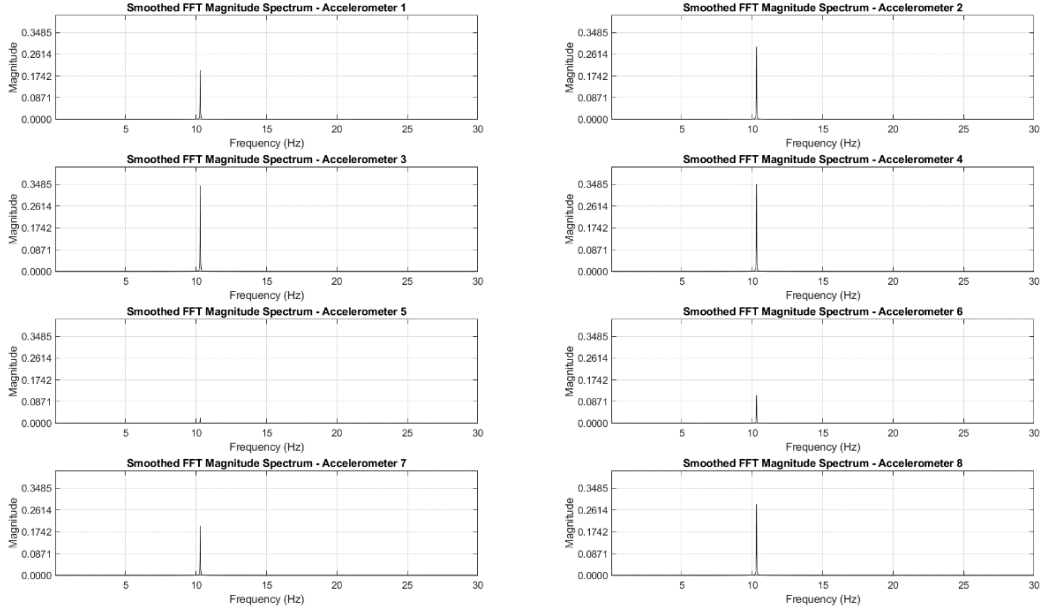


Figure B.11 The results of FFT of the forced vibration test performed on the SW direction in Pole 16-Gravel showing the natural frequency of the second mode shape

28 - Dynamic - SW - 16 - Gravel - Mode Shape 3

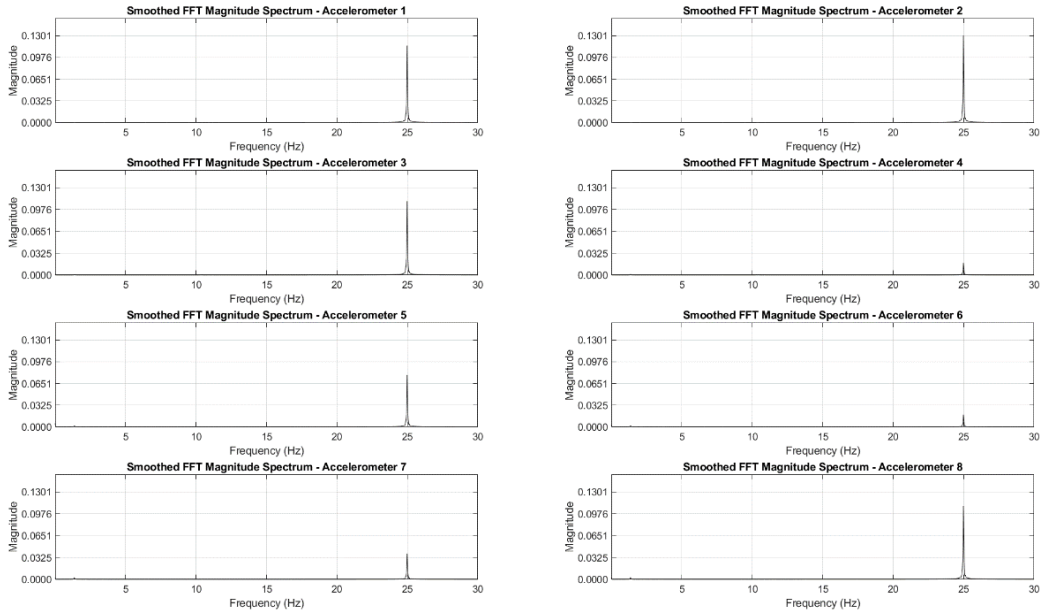


Figure B.12 The results of FFT of the forced vibration test performed on the SW direction on Pole 16-Gravel showing the natural frequency of third mode shape

35 - Dynamic - NE - 12 - Concrete - Mode Shape 1

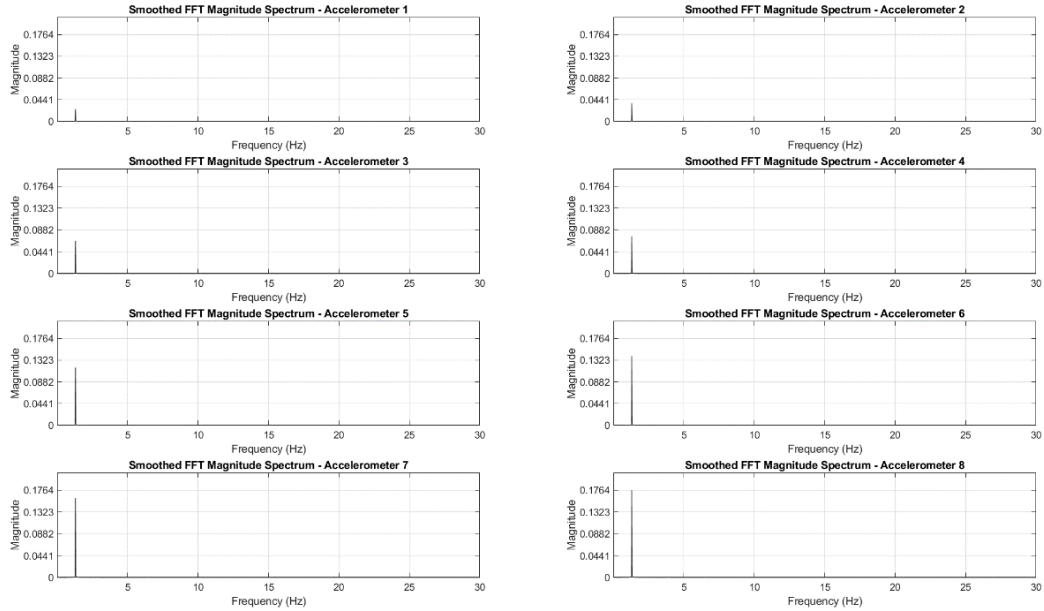


Figure B.13 The results of FFT of the forced vibration test performed in the NE direction on Pole 12-Concrete showing the natural frequency of the first mode shape

35 - Dynamic - NE - 12 - Concrete - Mode Shape 2

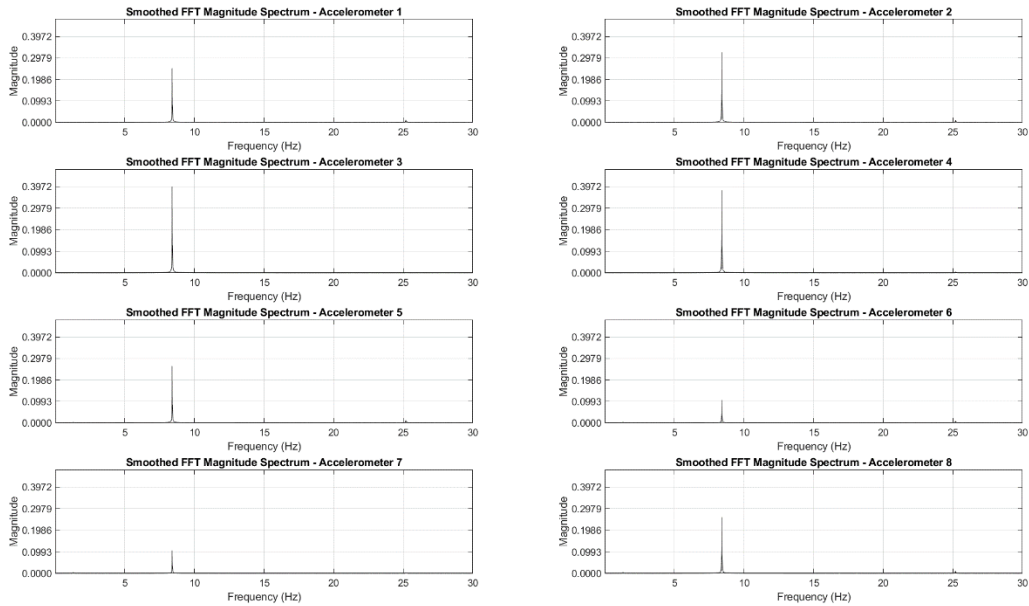


Figure B.14 The results of FFT of the forced vibration test performed on the NE direction on Pole 12-Concrete showing the natural frequency of second mode shape

35 - Dynamic - NE - 12 - Concrete - Mode Shape 3

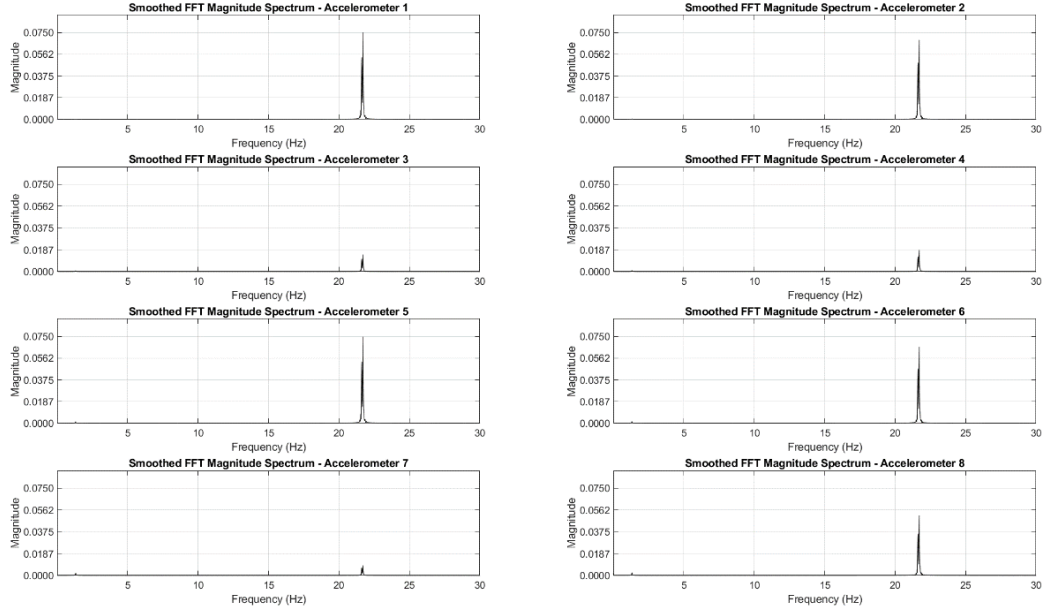


Figure B.15 The results of FFT of the forced vibration test performed in the NE direction on Pole 12-Concrete showing the natural frequency of the third mode shape

42 - Dynamic - SW - 12 - Concrete - Mode Shape 1

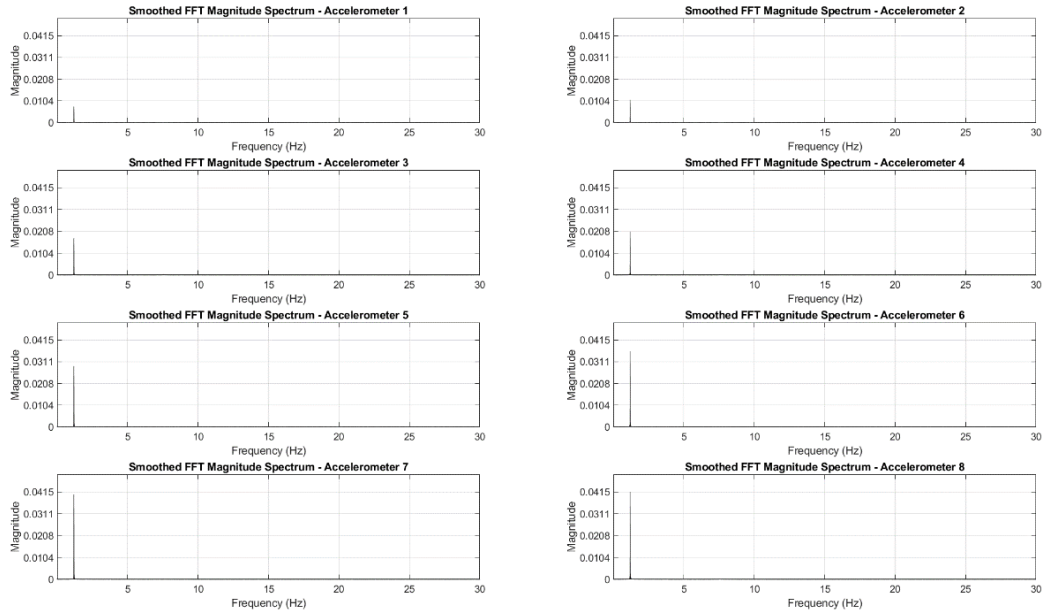


Figure B.16 The results of FFT of the forced vibration test performed in the SW direction on Pole 12-Concrete showing the natural frequency of the first mode shape

42 - Dynamic - SW - 12 - Concrete - Mode Shape 2

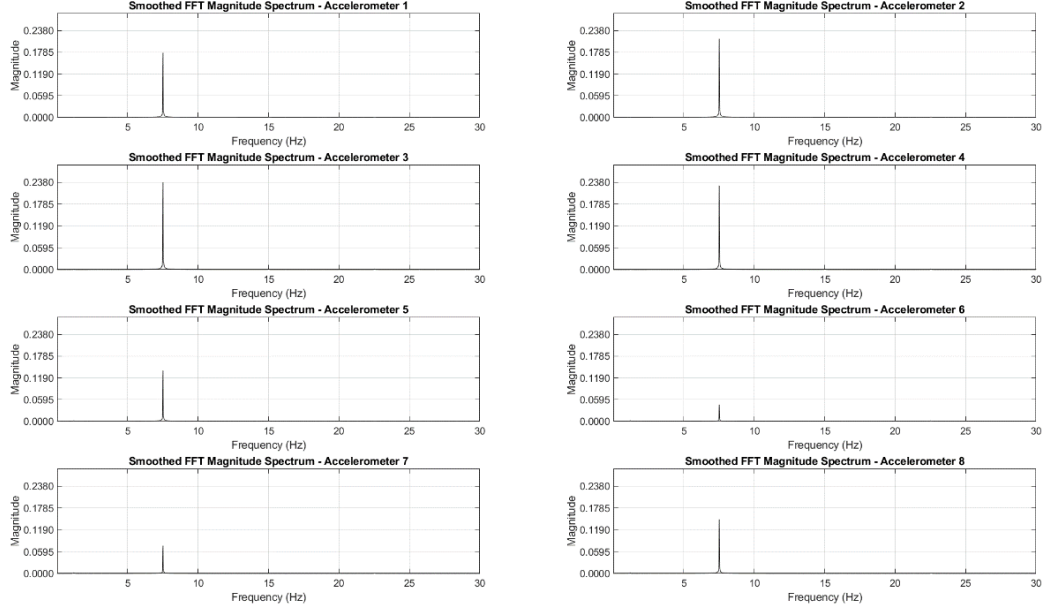


Figure B.17 The results of FFT of the forced vibration test performed on the SW direction on Pole 12-Concrete showing the natural frequency of second mode shape

42 - Dynamic - SW - 12 - Concrete - Mode Shape 3

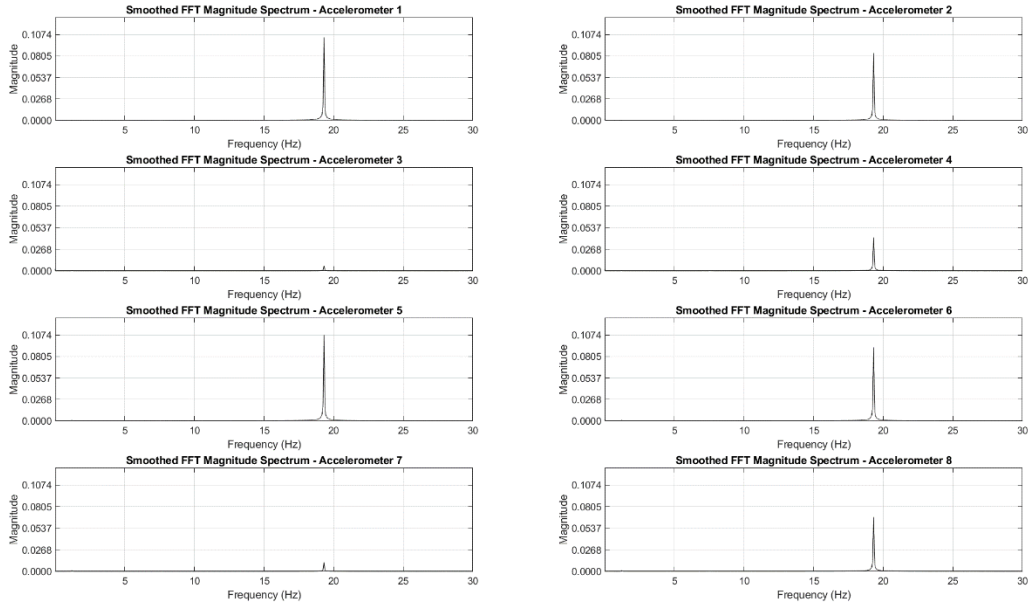


Figure B.18 The results of FFT of the forced vibration test performed in the SW direction on Pole 12-Concrete showing the natural frequency of the third mode shape

49 - Dynamic - NE - 12 - Gravel - Mode Shape 1

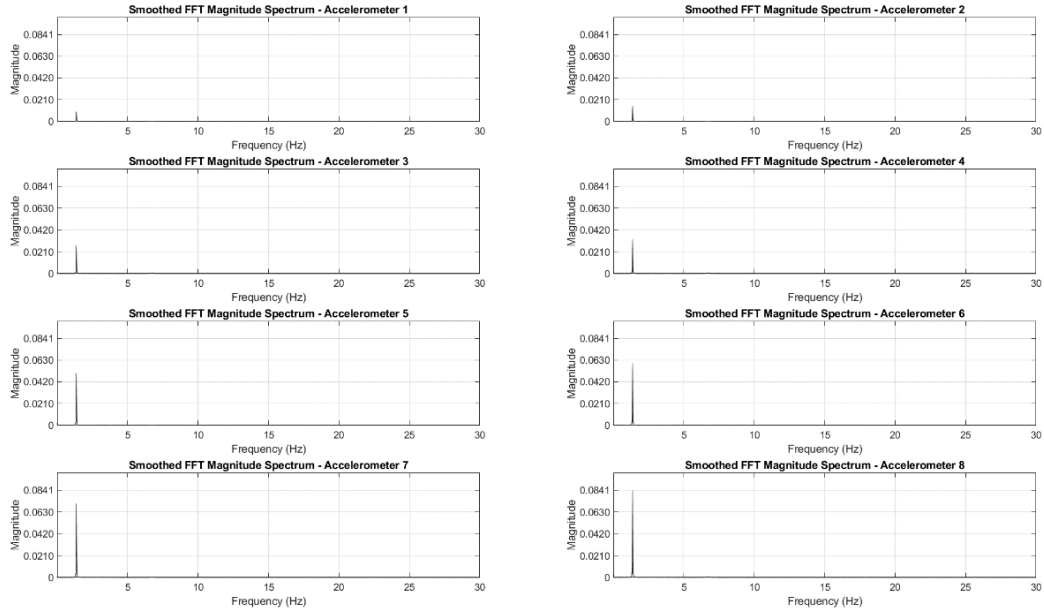


Figure B.19 The results of FFT of the forced vibration test performed in the NE direction on Pole 12-Gravel showing the natural frequency of the first mode shape

49 - Dynamic - NE - 12 - Gravel - Mode Shape 2

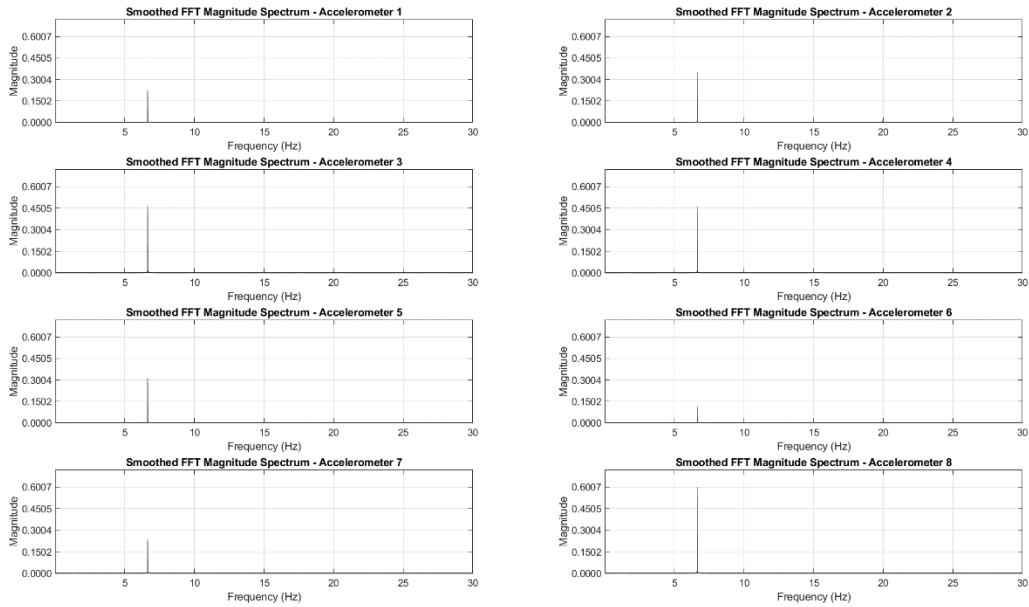


Figure B.20 The results of FFT of the forced vibration test performed in the NE direction on Pole 12-Gravel showing the natural frequency of the second mode shape

49 - Dynamic - NE - 12 - Gravel - Mode Shape 3

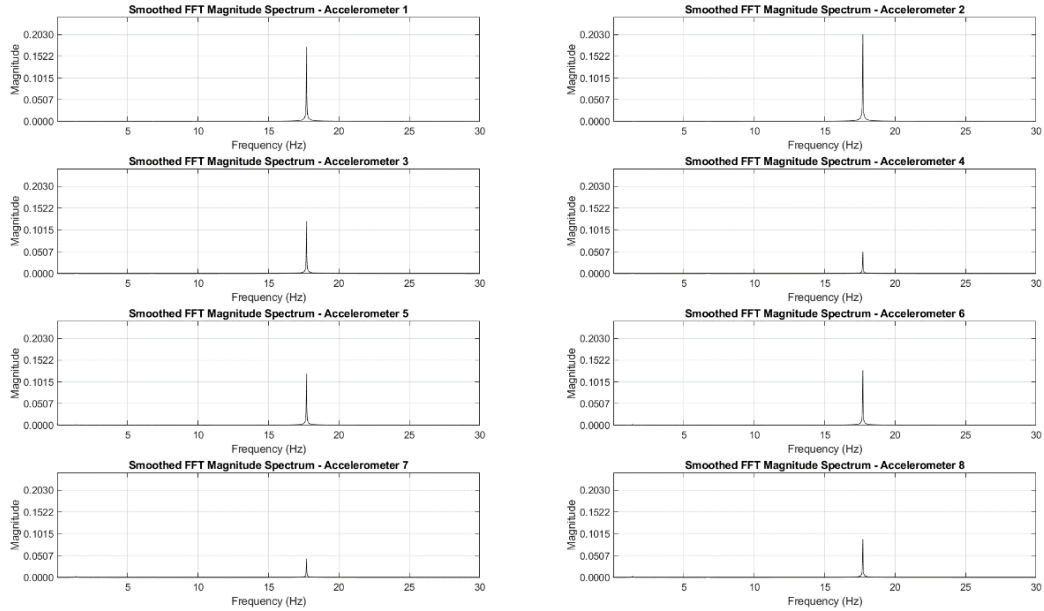


Figure B.21 The results of FFT of the forced vibration test performed in the NE direction on Pole 12-Gravel showing the natural frequency of the third mode shape

56 - Dynamic - SW - 12 - Gravel - Mode Shape 1

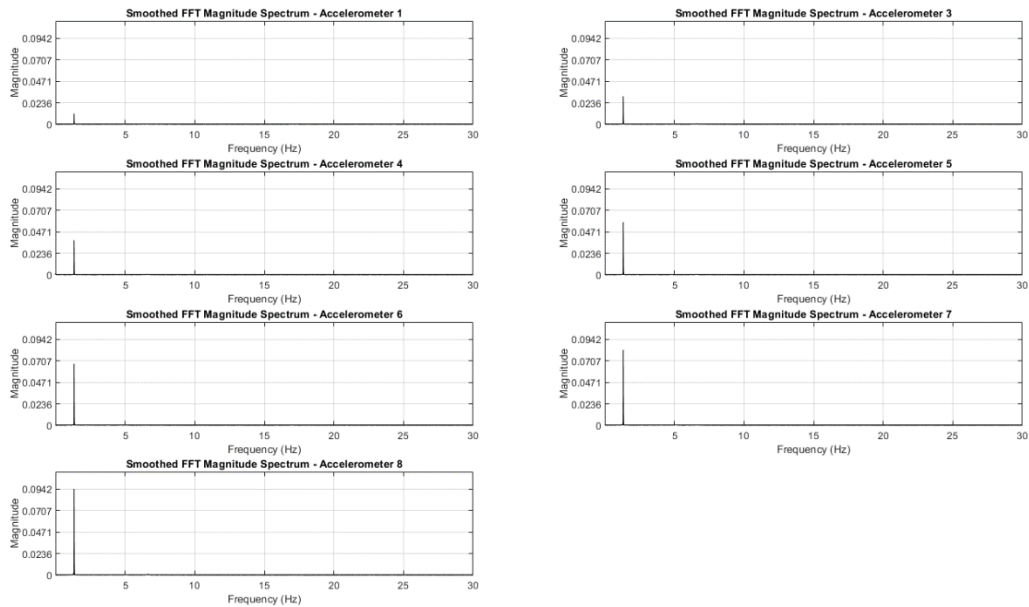


Figure B.22 The results of FFT of the forced vibration test performed on the SW direction on Pole 12-Gravel showing the natural frequency of first mode shape

56 - Dynamic - SW - 12 - Gravel - Mode Shape 2

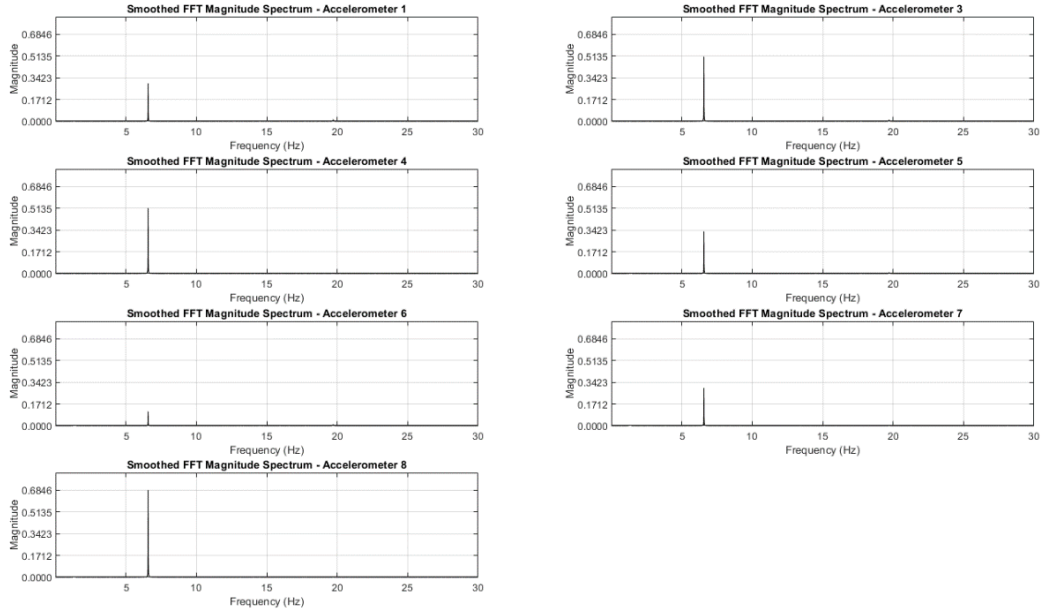


Figure B.23 The results of FFT of the forced vibration test performed in the SW direction on Pole 12-Gravel showing the natural frequency of the second mode shape

56 - Dynamic - SW - 12 - Gravel - Mode Shape 3

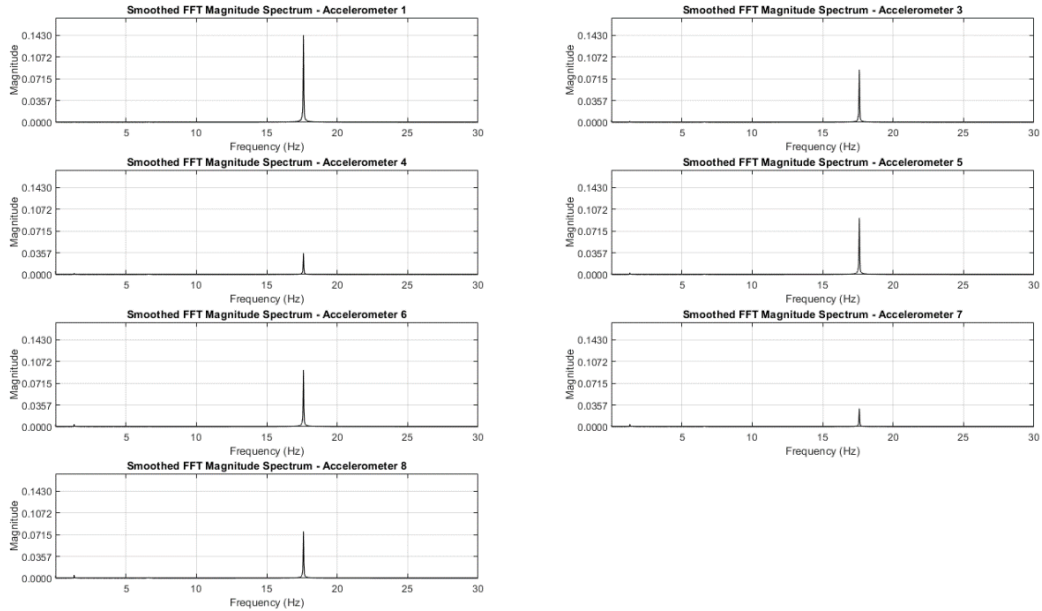


Figure B.24 The results of FFT of the forced vibration test performed in the SW direction on Pole 12-Gravel showing the natural frequency of the third mode shape

Appendix C Inclinometer Rotations

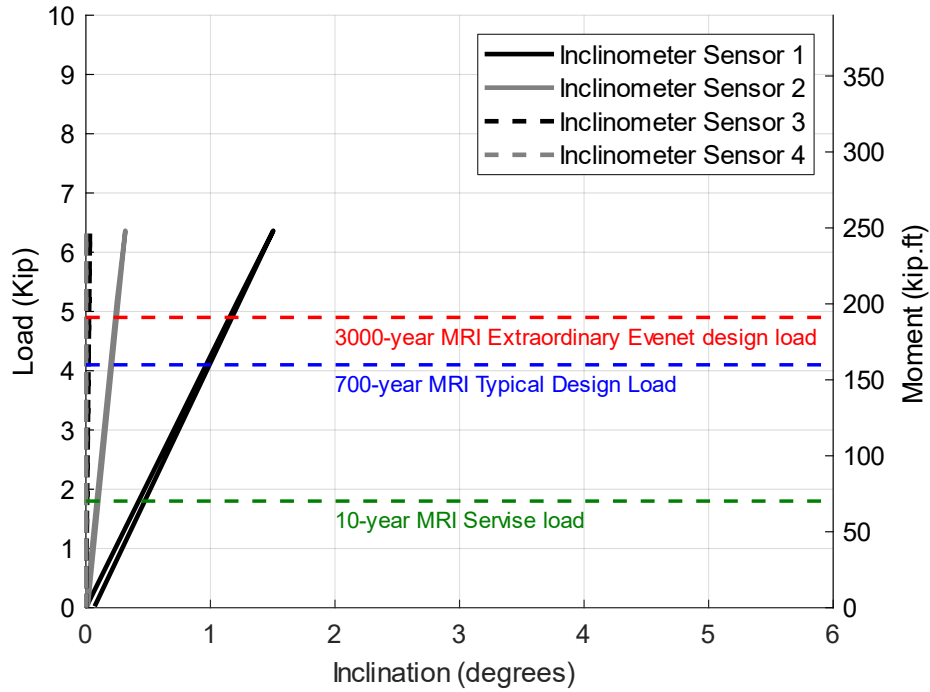


Figure C.1 The results of the first static test performed in the SE direction on Pole 16-concrete showing the inclination vs load and moment

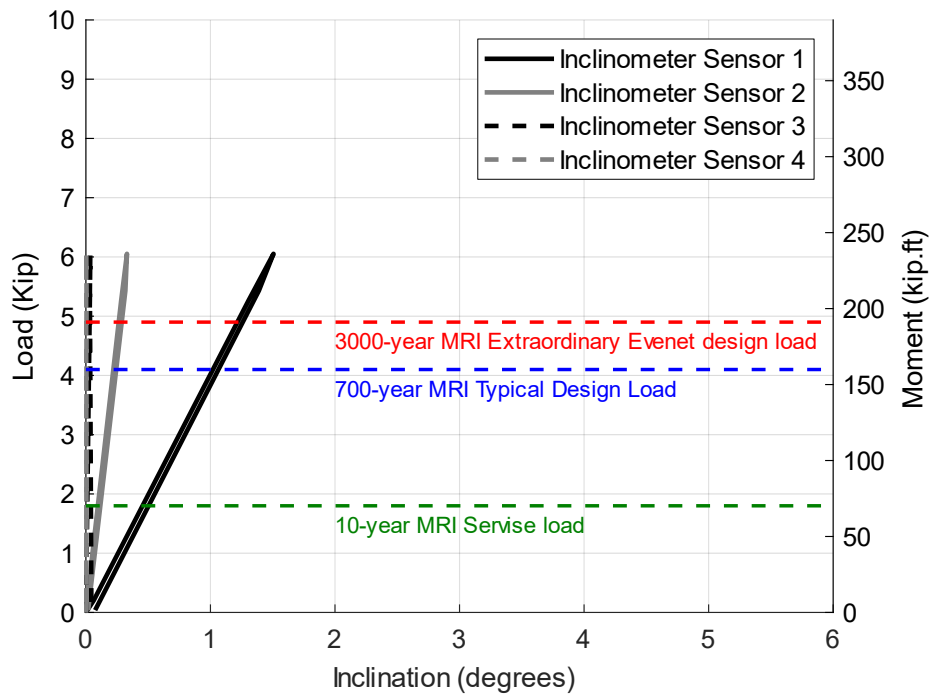


Figure C.2 The results of the second static test performed in the SE direction on Pole 16-Concrete showing the inclination vs load and moment

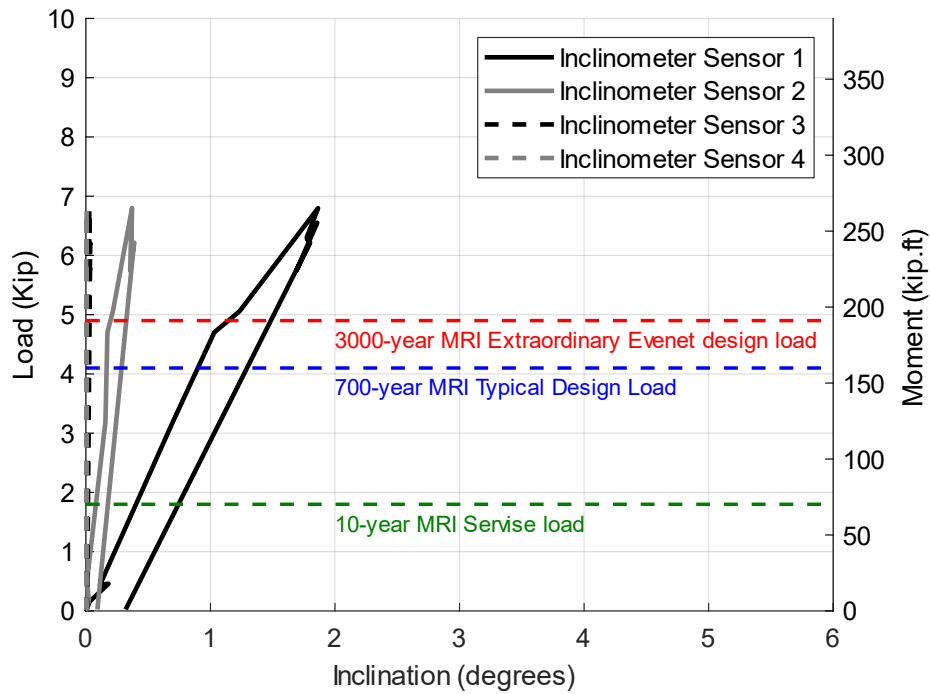


Figure C.3 The results of the third static test performed in the SE direction on Pole 16-Concrete showing the inclination vs load and moment

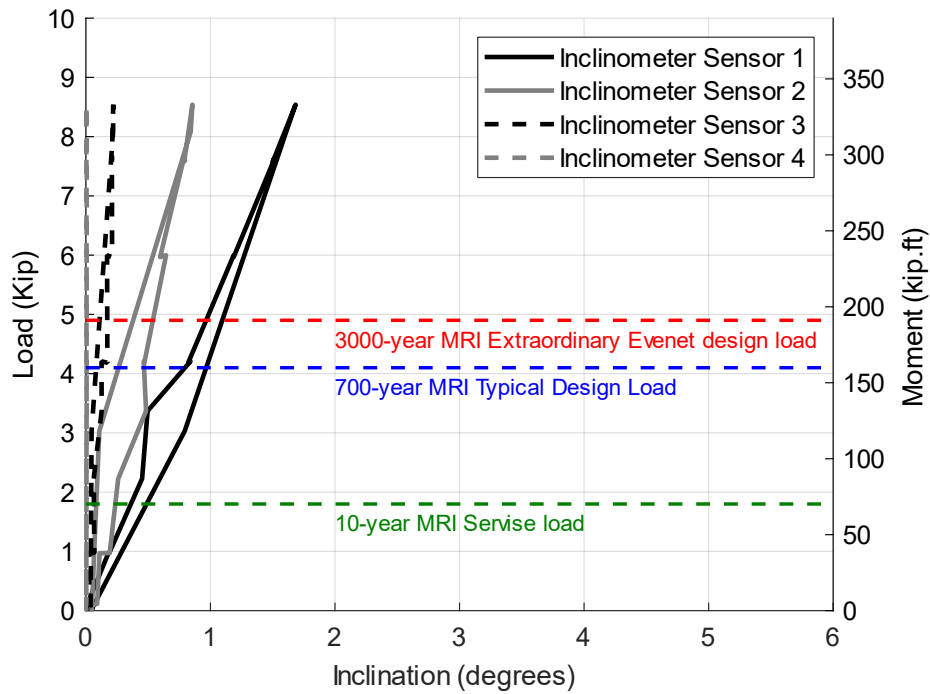


Figure C.4 The results of the first static test performed in the NE direction on Pole 16-Gravel showing the inclination vs load and moment

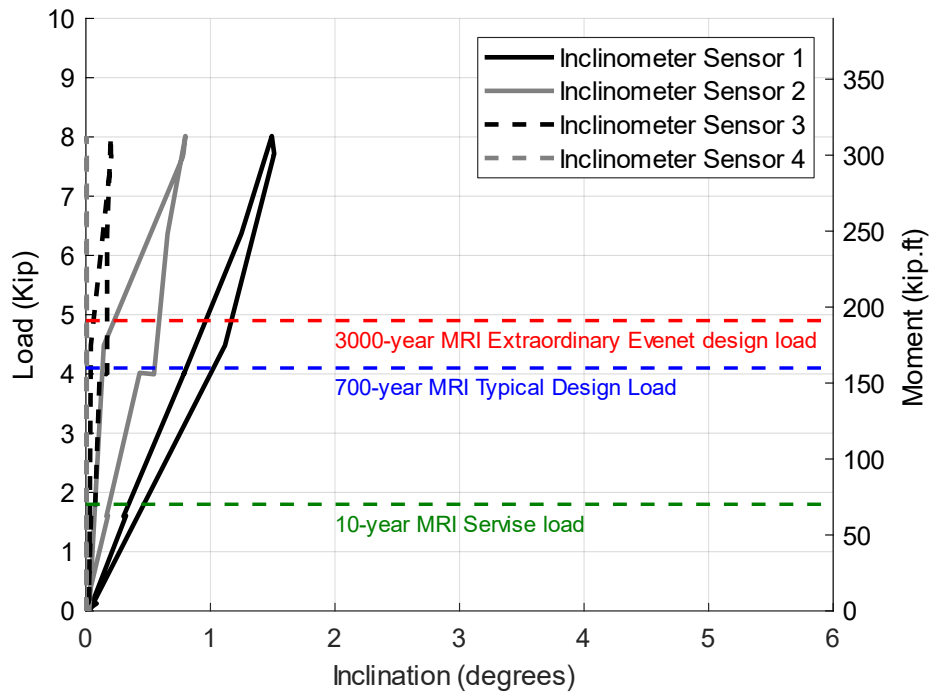


Figure C.5 The results of the second static test performed in the NE direction on Pole 16-Gravel showing the inclination vs load and moment

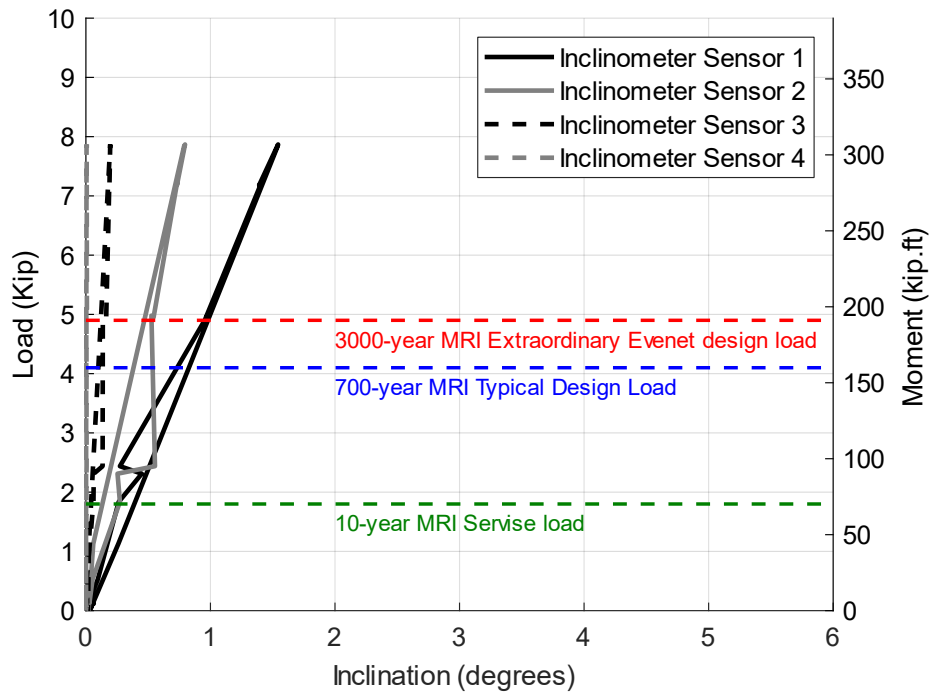


Figure C.6 The results of the third static test performed in the NE direction on Pole 16-Gravel showing the inclination vs load and moment

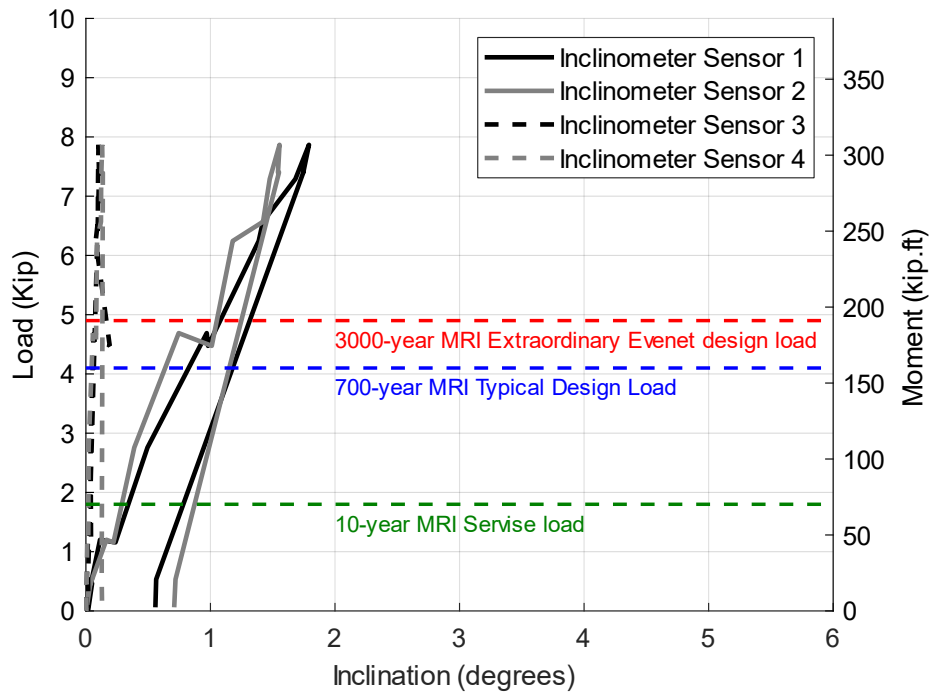


Figure C.7 The results of the first static test performed in the SW direction on Pole 16-Gravel showing the inclination vs load and moment

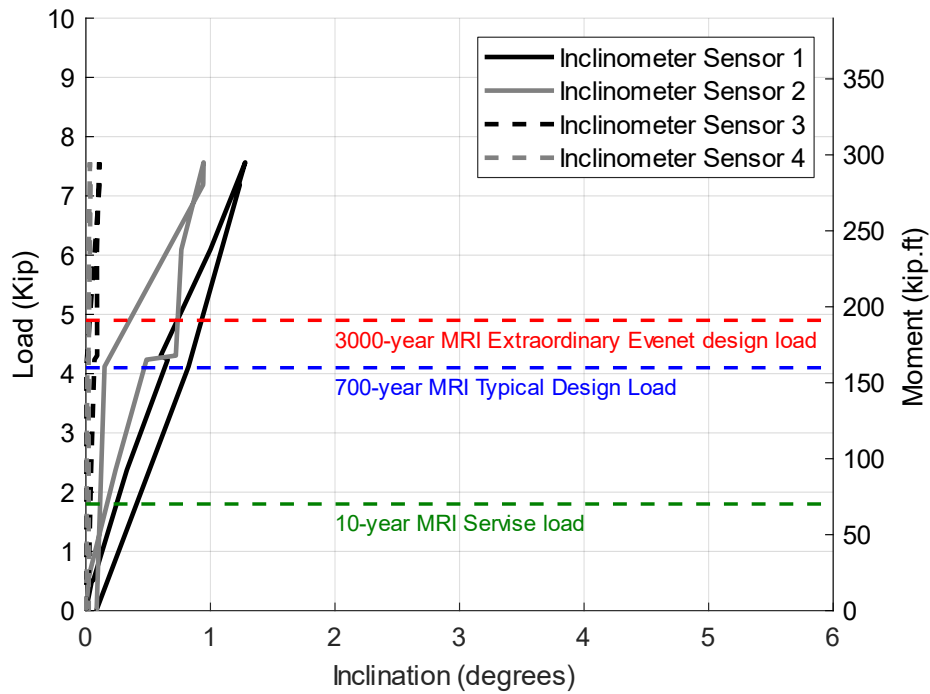


Figure C.8 The results of the second static test performed in the SW direction on Pole 16-Gravel showing the inclination vs load and moment

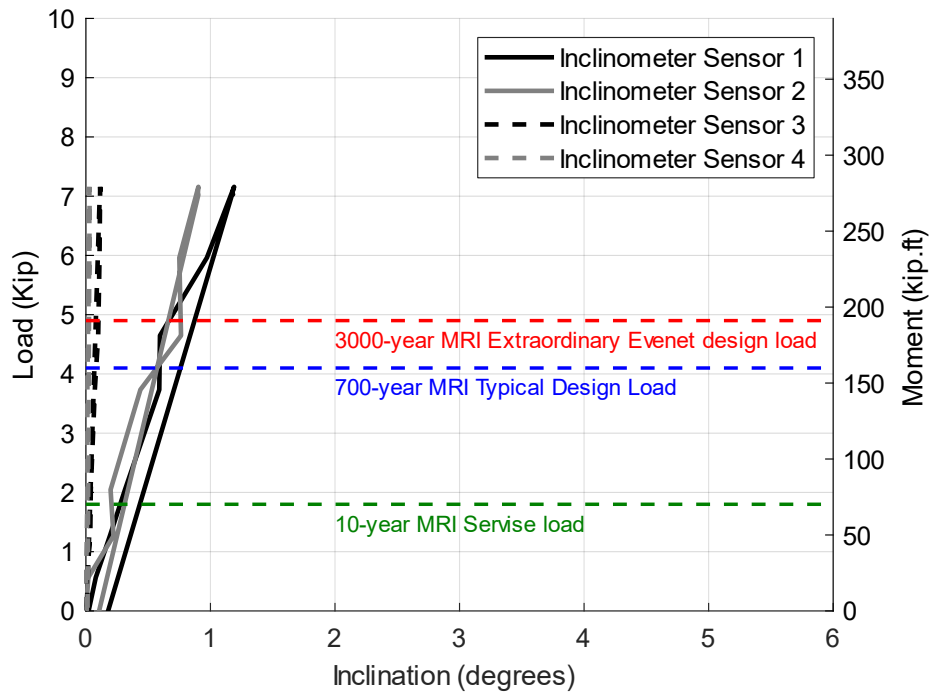


Figure C.9 The results of the third static test performed in the SW direction on Pole 16-Gravel showing the inclination vs load and moment

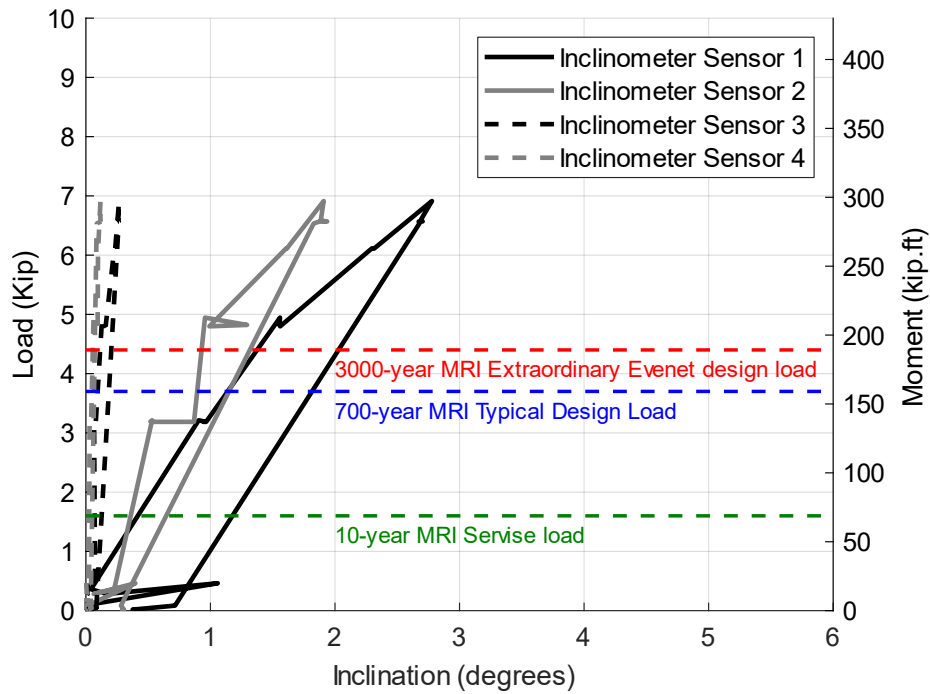


Figure C.10 The results of the first static test performed in the NE direction on Pole 12-Concrete showing the inclination vs load and moment

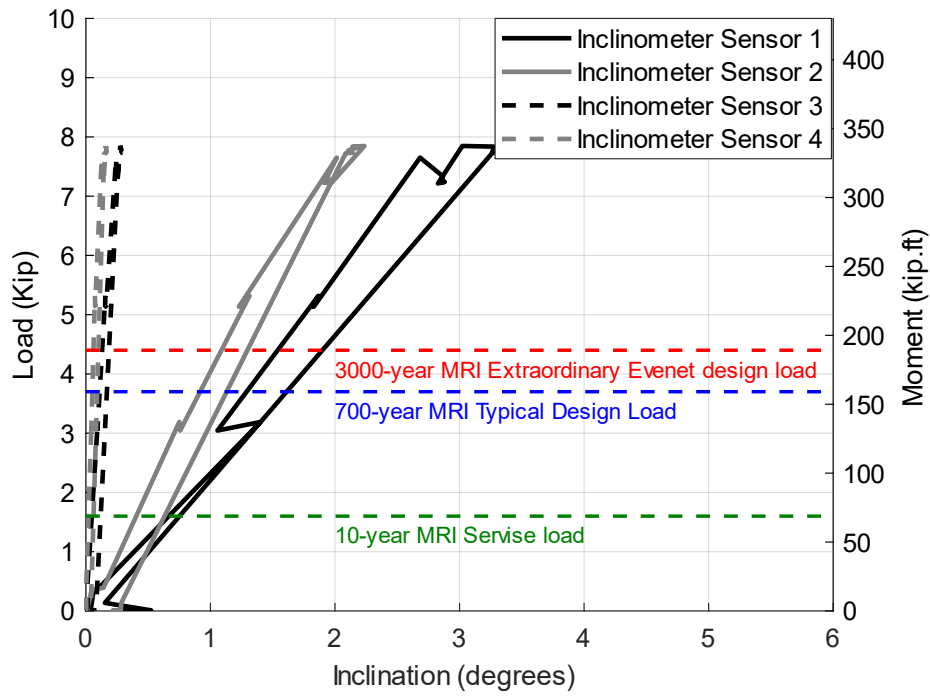


Figure C.11 The results of the second static test performed in the NE direction on Pole 12-Concrete showing the inclination vs load and moment

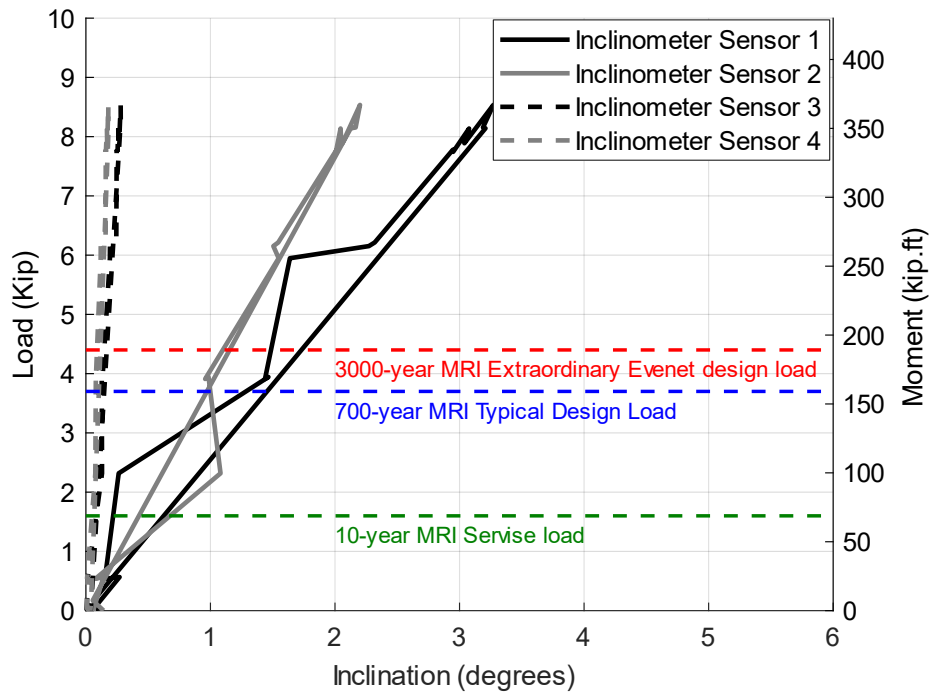


Figure C.12 The results of the third static test performed in the NE direction on Pole 12-Concrete showing the inclination vs load and moment

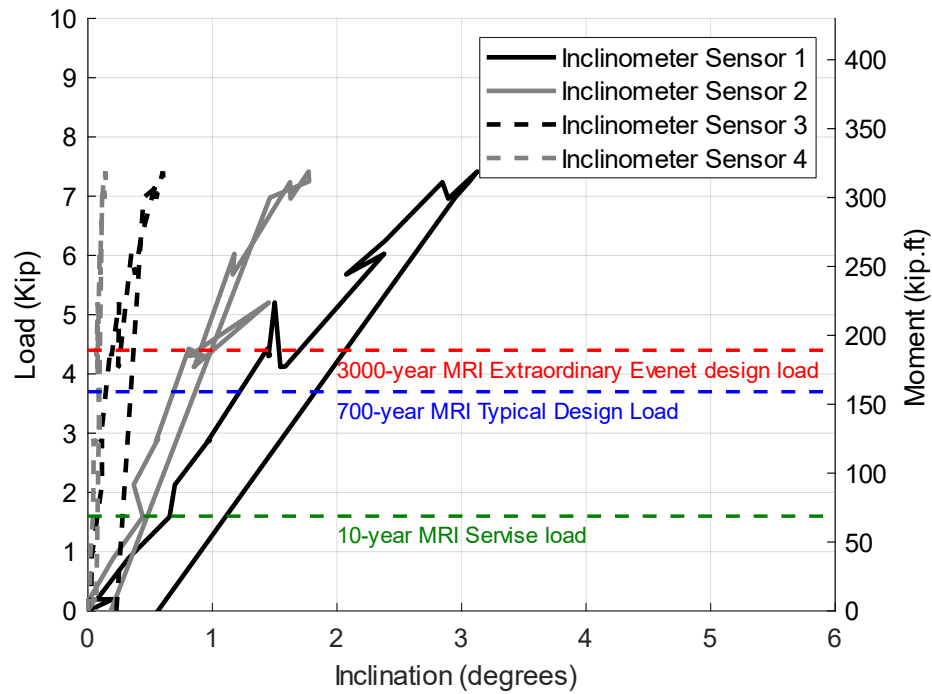


Figure C.13 The results of the first static test performed in the SW direction on Pole 12-Concrete showing the inclination vs load and moment

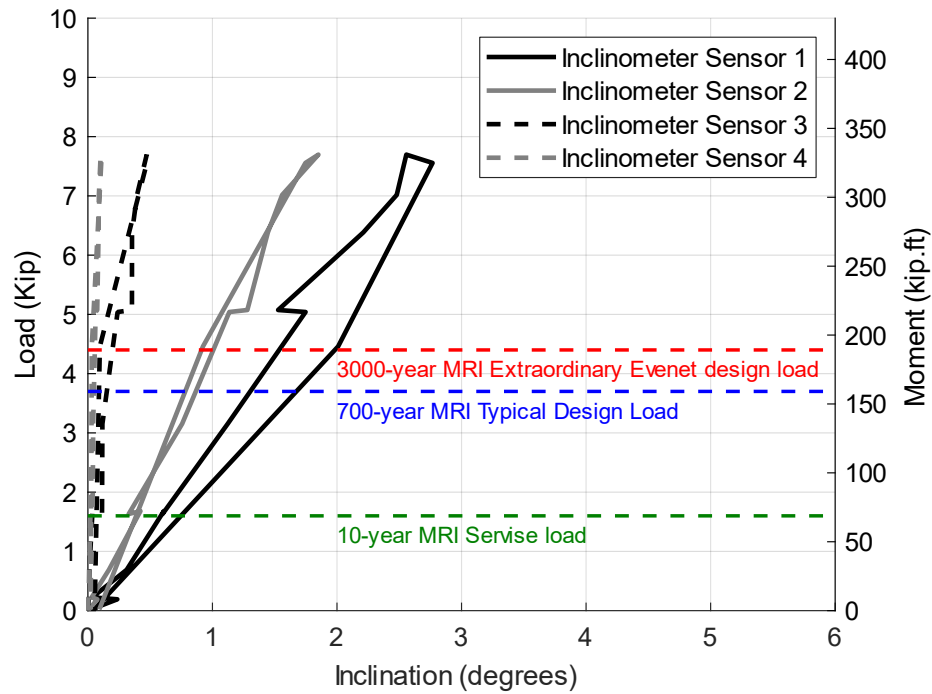


Figure C.14 The results of the second static test performed in the SW direction on Pole 12-Concrete showing the inclination vs load and moment

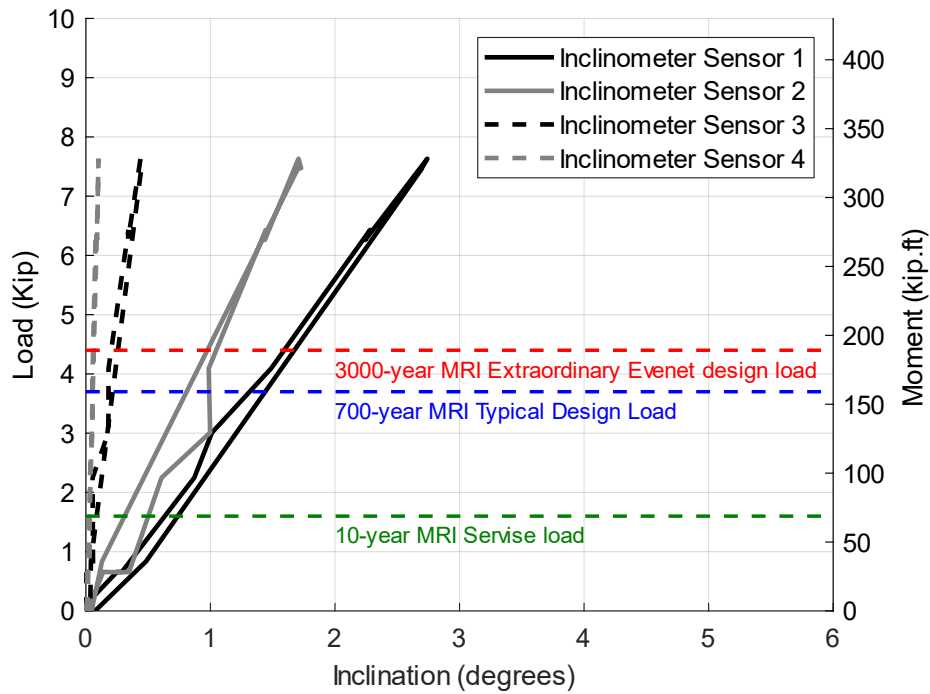


Figure C.15 The results of the third static test performed in the SW direction on Pole 12-Concrete showing the inclination vs load and moment

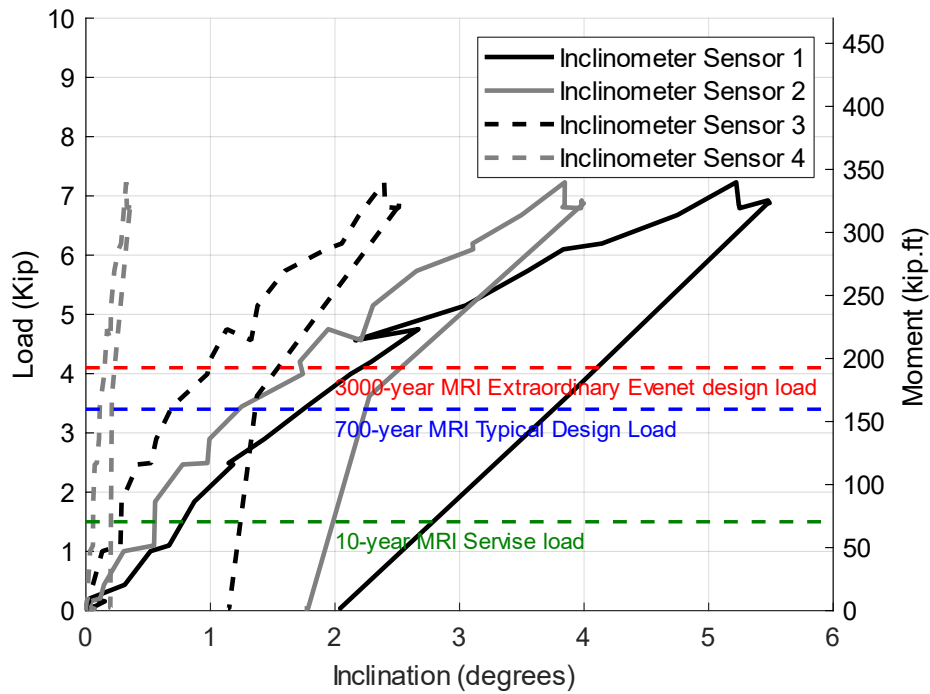


Figure C.16 The results of the first static test performed in the NE direction on Pole 12-Gravel showing the inclination vs load and moment

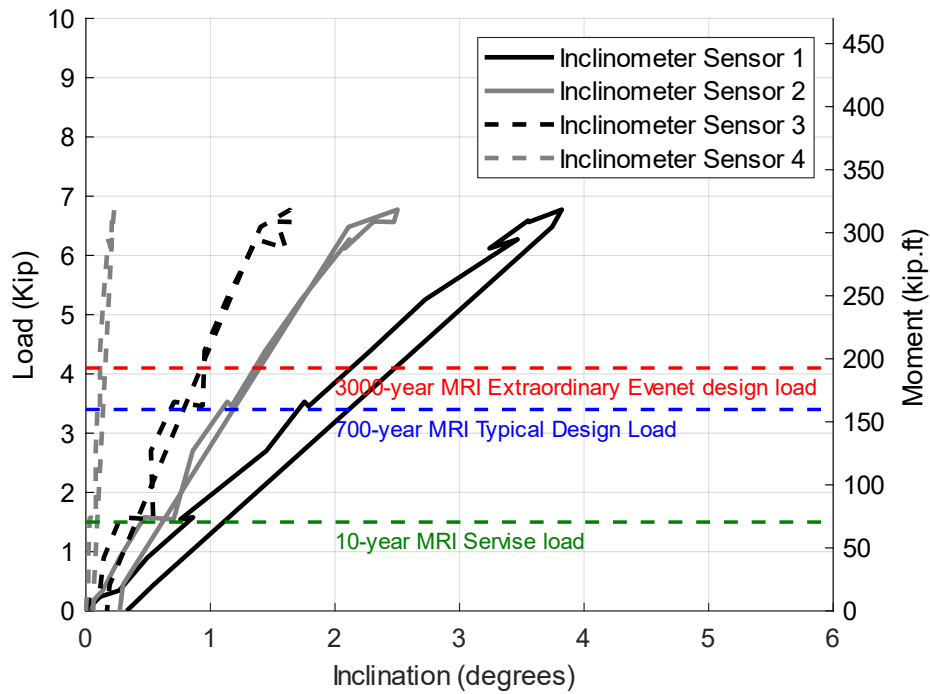


Figure C.17 The results of the second static test performed in the NE direction on Pole 12-Gravel showing the inclination vs load and moment

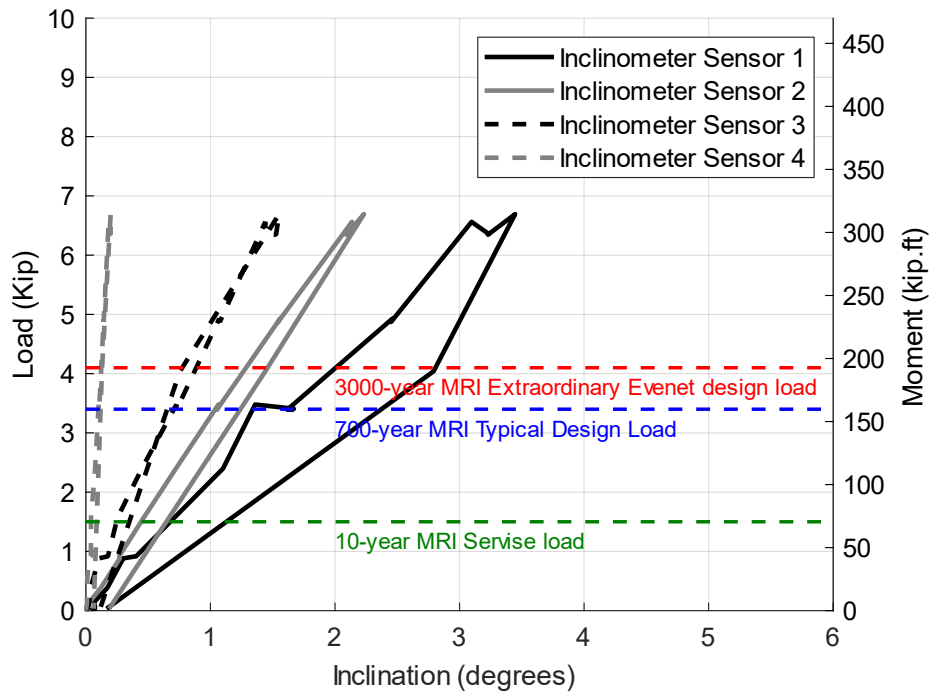


Figure C.18 The results of the second static test performed in the NE direction on Pole 12-Gravel showing the inclination vs load and moment

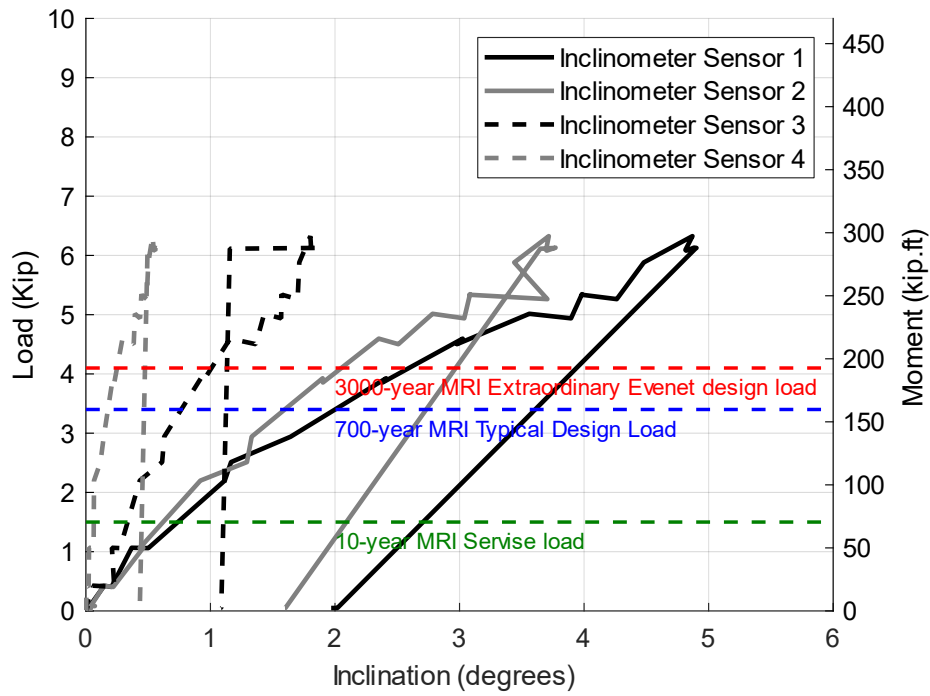


Figure C.19 The results of the first static test performed in the SW direction on Pole 12-Gravel showing the inclination vs load and moment

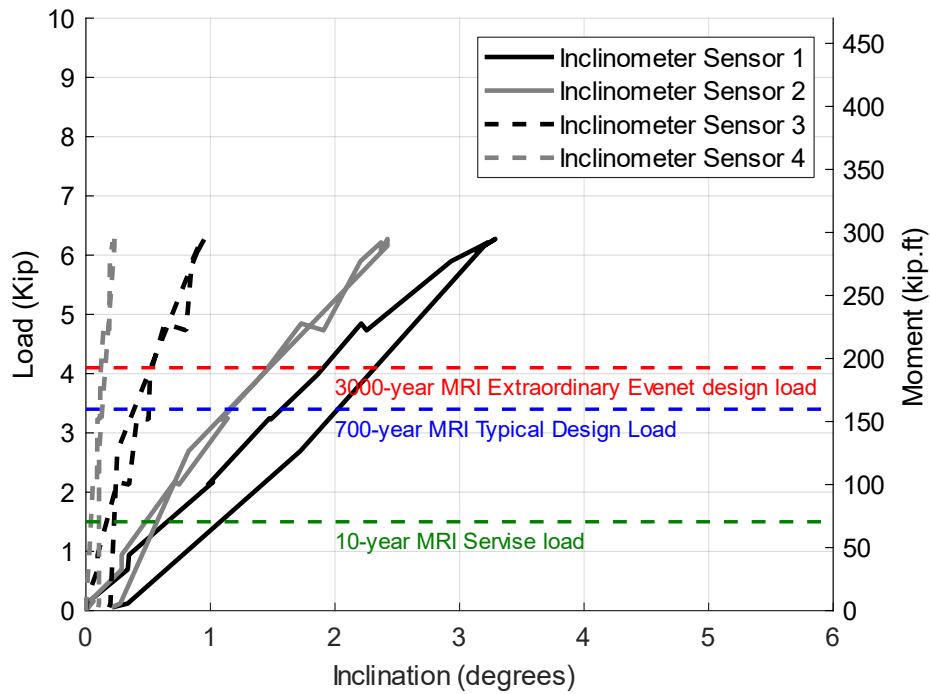


Figure C.20 The results of the second static test performed in the SW direction on Pole 12-Gravel showing the inclination vs load and moment

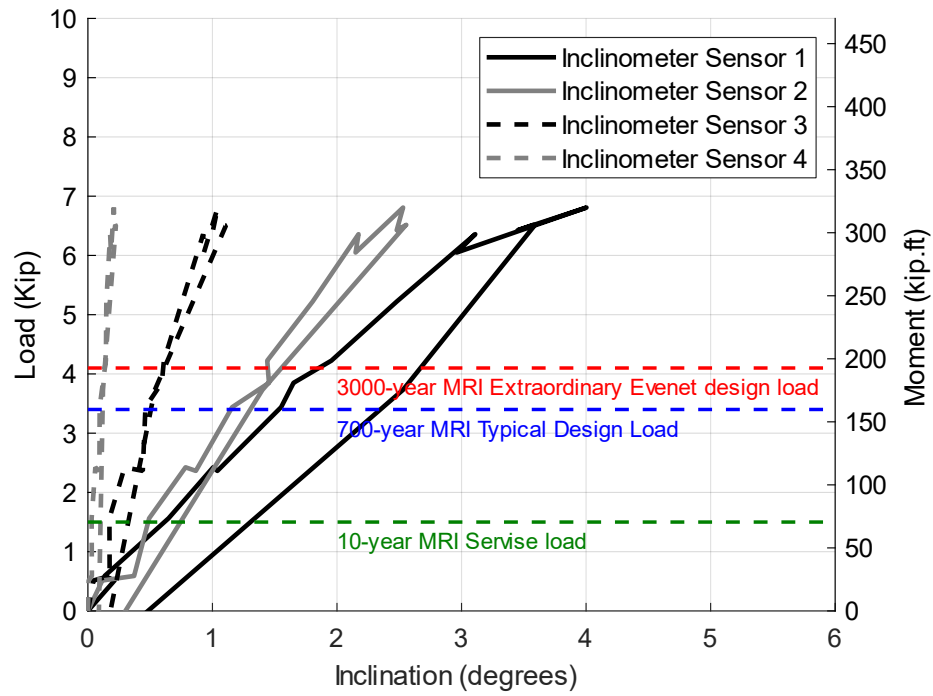


Figure C.21 The results of the third static test performed in the SW direction on Pole 12-Gravel showing the inclination vs load and moment

Appendix D Inclinometer Rotations at Maximum, 0.5 Maximum (approximate design), and Unloaded

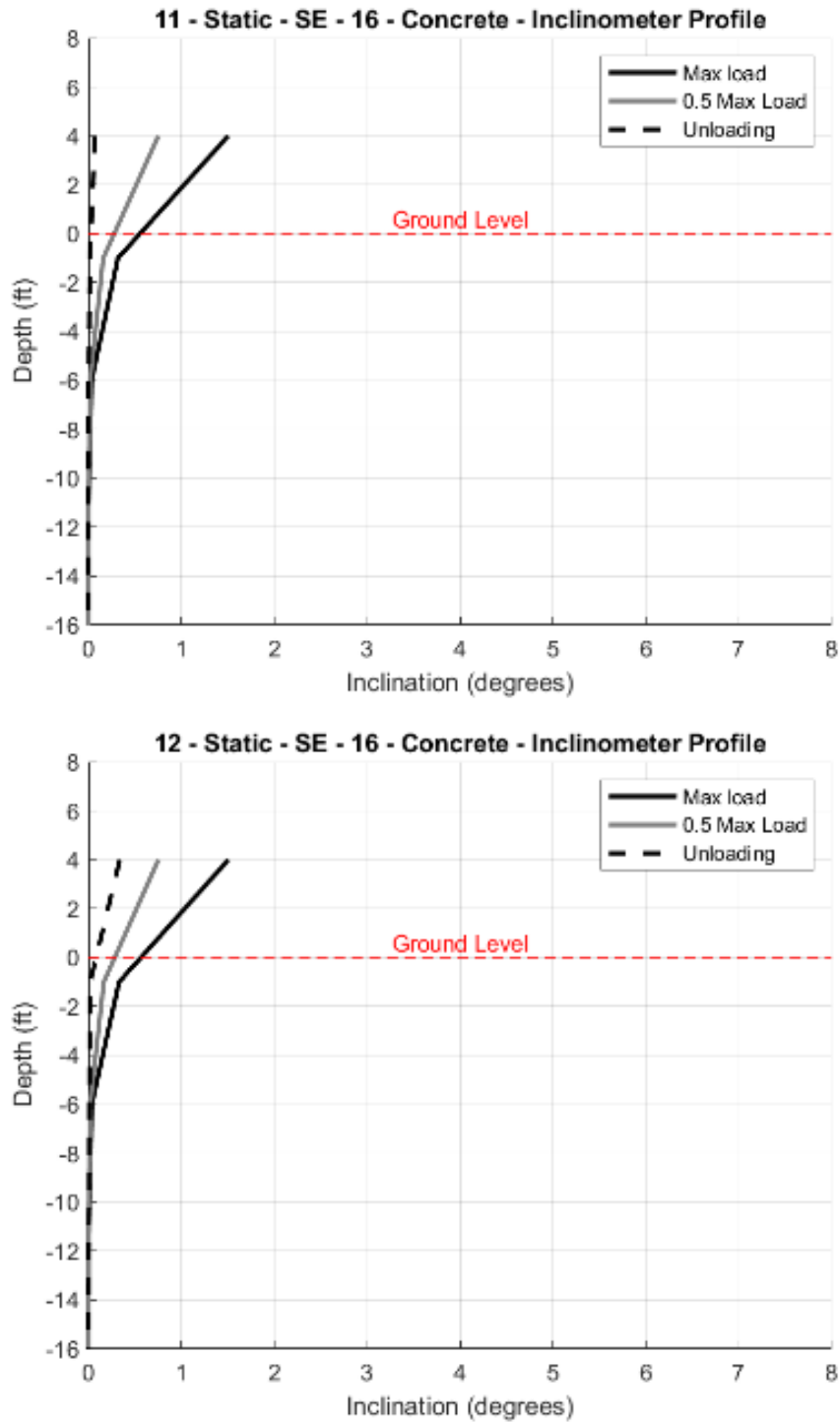


Figure D.1 The rotation vs inclination at ground level of static test 11 and 12 in SE direction performed on pole 16 – Concrete, the 700-yr design load is approximately 0.5 of the maximum load

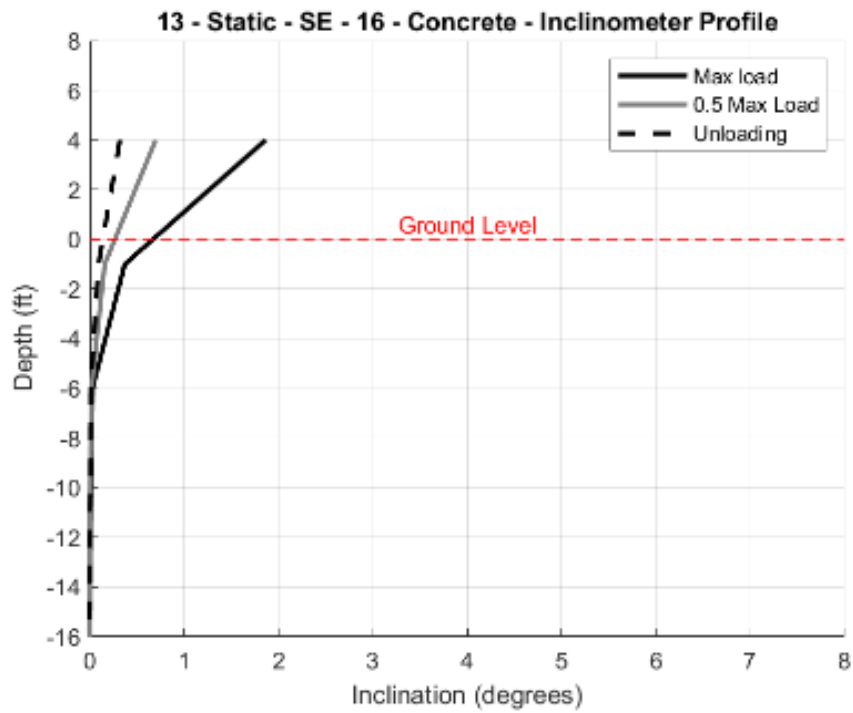


Figure D.1 The rotation vs inclination at ground level of static test 11 and 12 in SE direction performed on pole 16 – Concrete, the 700-yr design load is approximately 0.5 of the maximum load

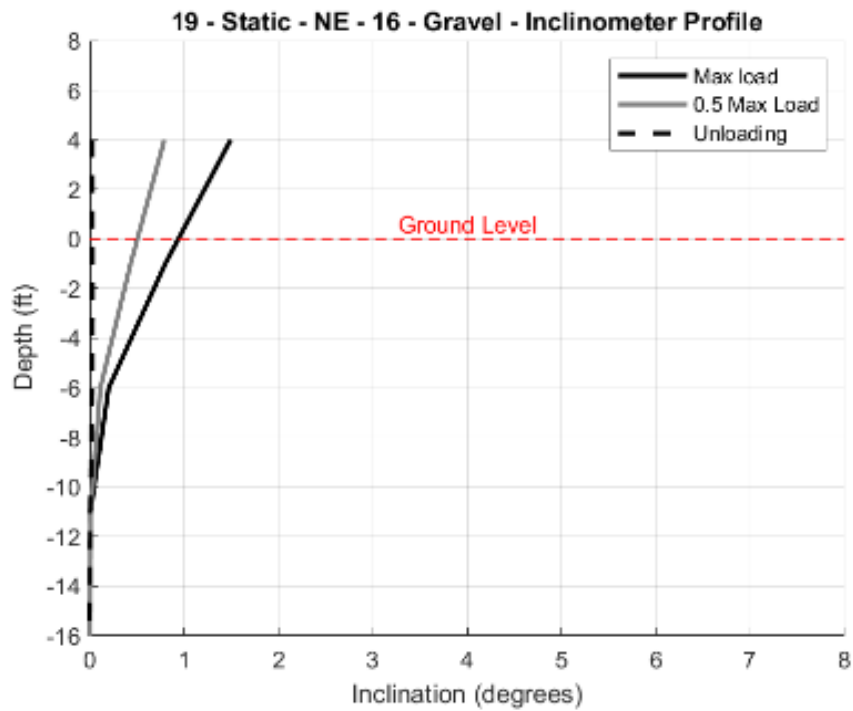
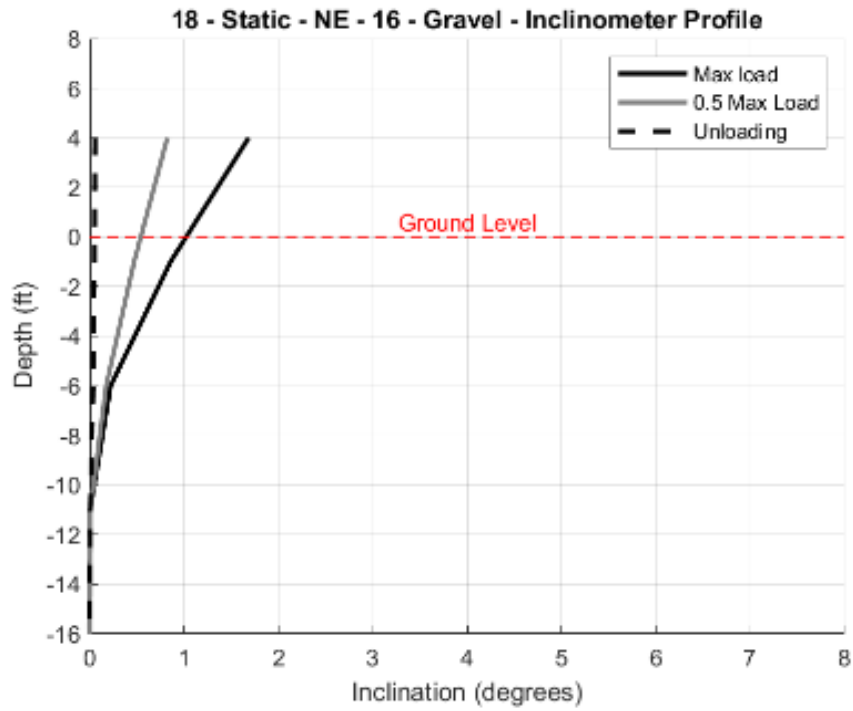


Figure D.2 The rotation vs inclination at ground level of static tests 18 and 19 in NE direction performed on pole 16 – Gravel, the 700-yr design load is approximately 0.5 of the maximum load

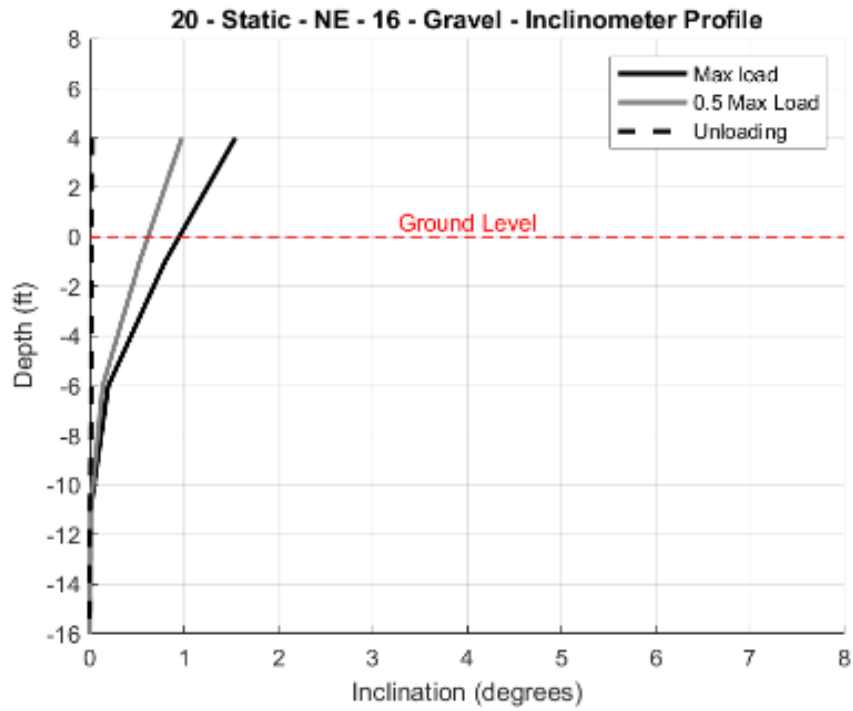


Figure D.2 The rotation vs inclination at ground level of static tests 18 and 19 in NE direction performed on pole 16 – Gravel, the 700-yr design load is approximately 0.5 of the maximum load

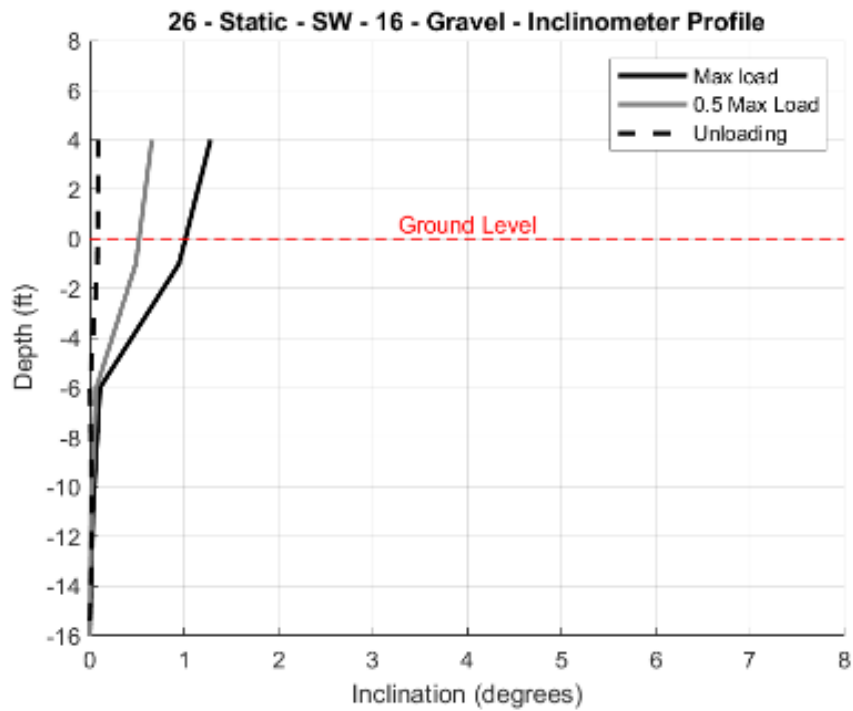


Figure D.3 The rotation vs inclination at ground level of static test 25 and 26 in SW direction performed on pole 16 – Gravel, the 700-yr design load is approximately 0.5 of the maximum load

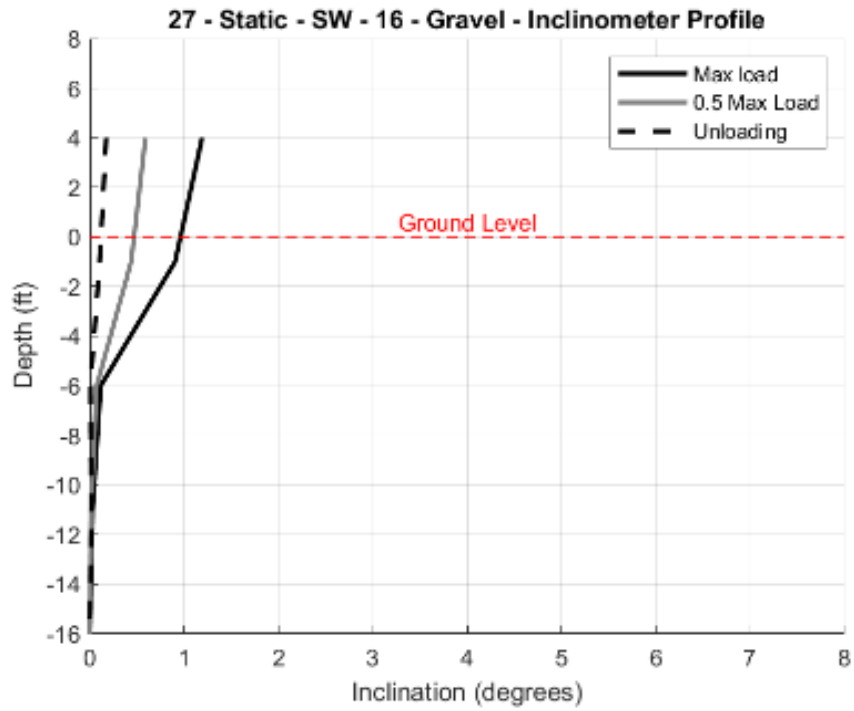


Figure D.3 The rotation vs inclination at ground level of static test 25 and 26 in SW direction performed on pole 16 – Gravel, the 700-yr design load is approximately 0.5 of the maximum load

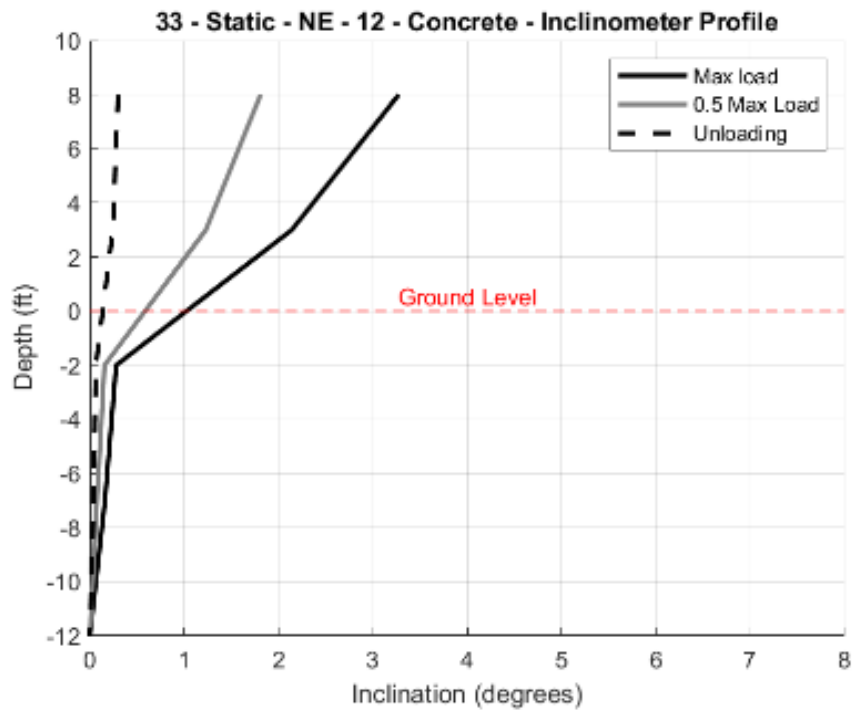
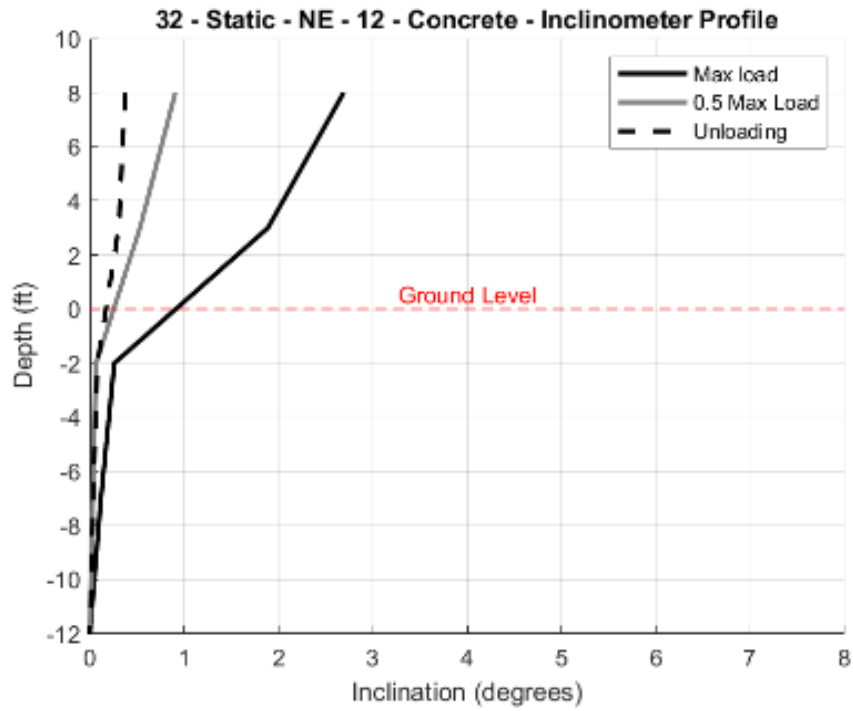


Figure D.4 The rotation vs inclination at ground level of static tests 32 and 33 in NE direction performed on pole 12 – Concrete, the 700-yr design load is approximately 0.5 of the maximum load

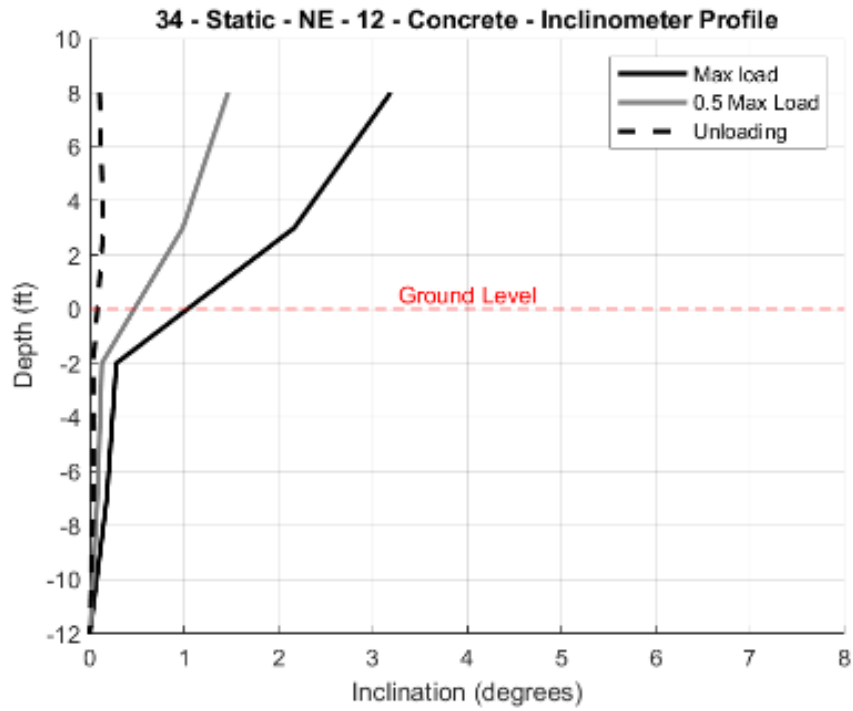


Figure D.4 The rotation vs inclination at ground level of static tests 32 and 33 in NE direction performed on pole 12 – Concrete, the 700-yr design load is approximately 0.5 of the maximum load

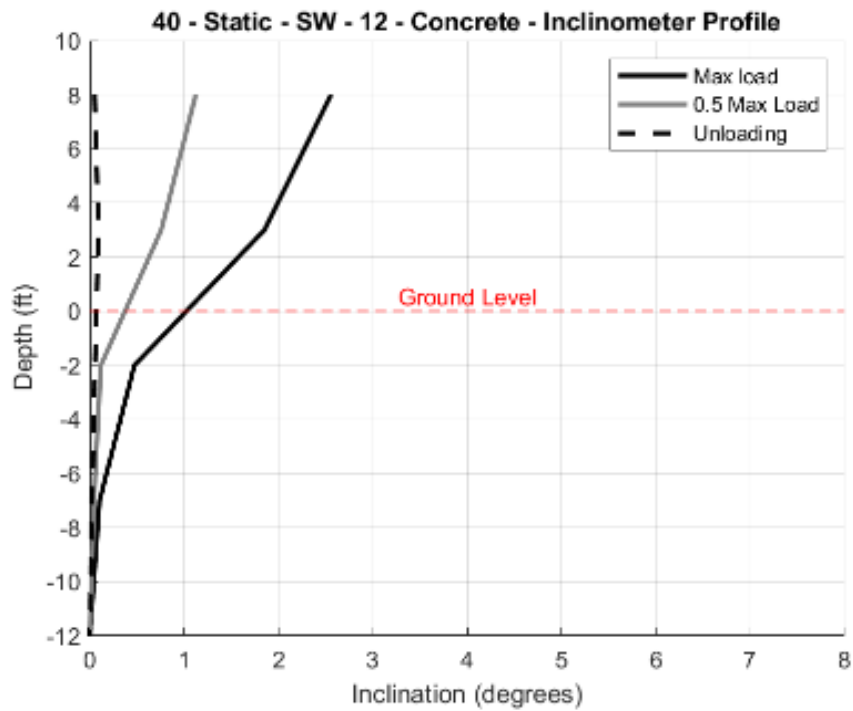
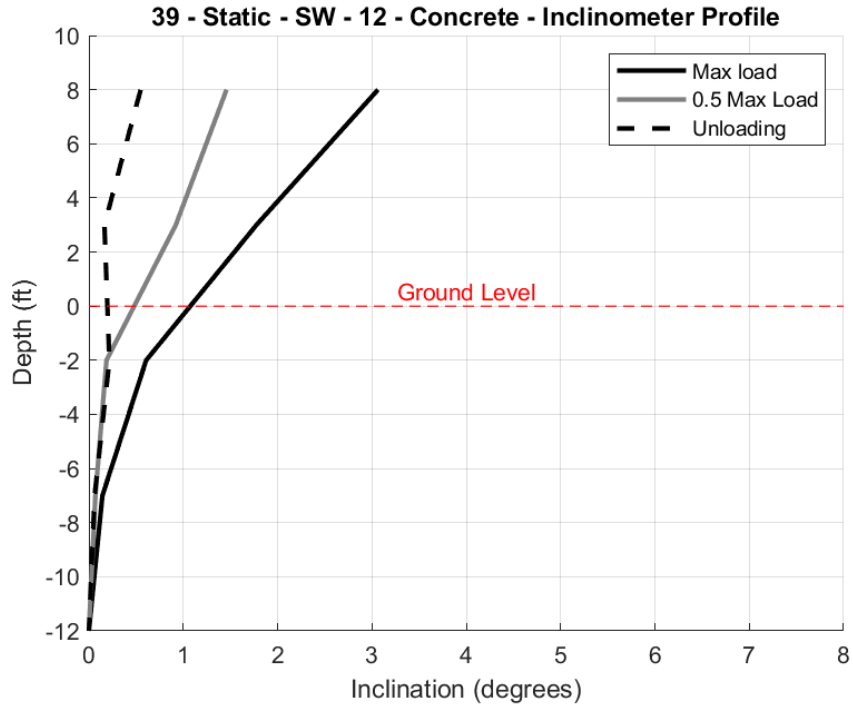


Figure D.5 The rotation vs inclination at ground level of static tests 39 and 40 in SW direction performed on pole 12 – Concrete, the 700-yr design load is approximately 0.5 of the maximum load

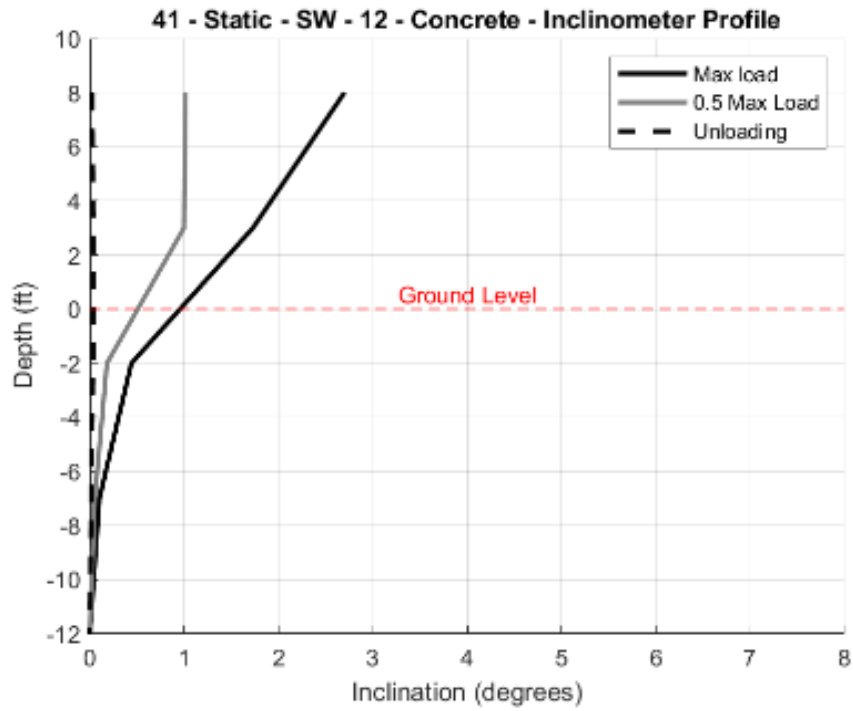


Figure D.5 The rotation vs inclination at ground level of static tests 39 and 40 in SW direction performed on pole 12 – Concrete, the 700-yr design load is approximately 0.5 of the maximum load

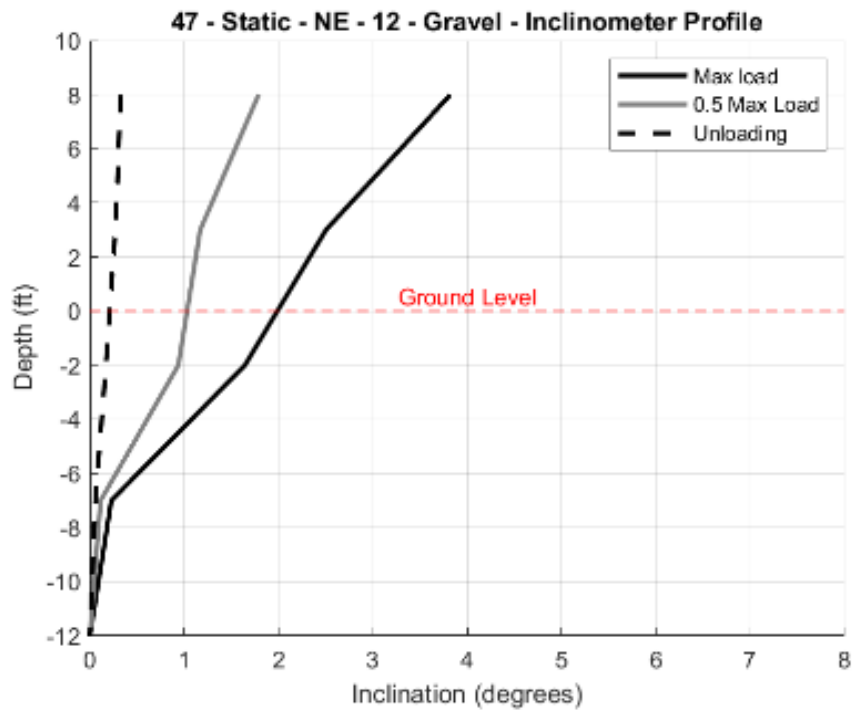
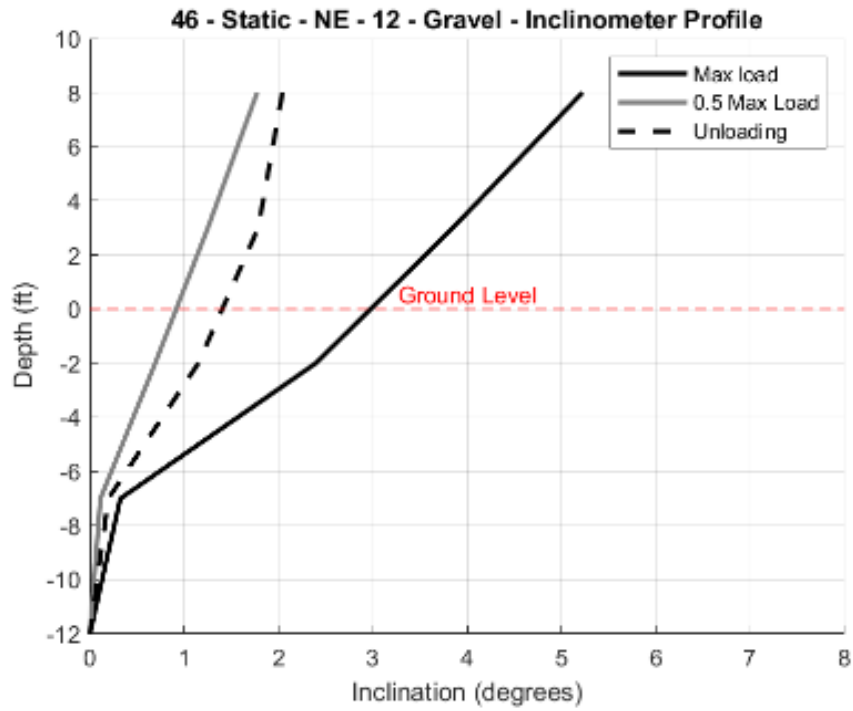


Figure D.6 The rotation vs inclination at ground level of static tests 46 and 47 in NE direction performed on pole 12 – Gravel, the 700-yr design load is approximately 0.5 of the maximum load

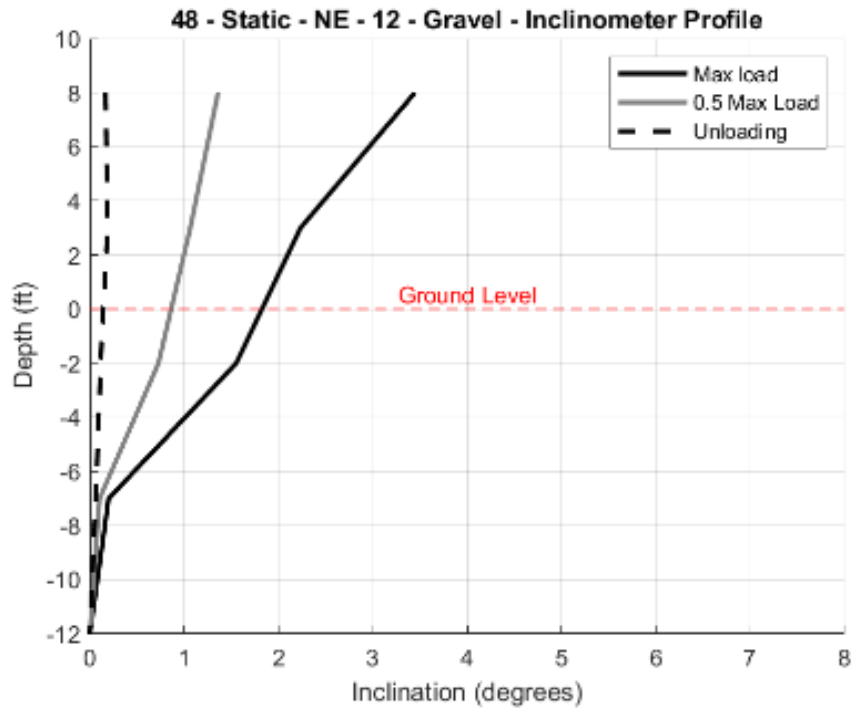


Figure D.6 The rotation vs inclination at ground level of static tests 46 and 47 in NE direction performed on pole 12 – Gravel, the 700-yr design load is approximately 0.5 of the maximum load

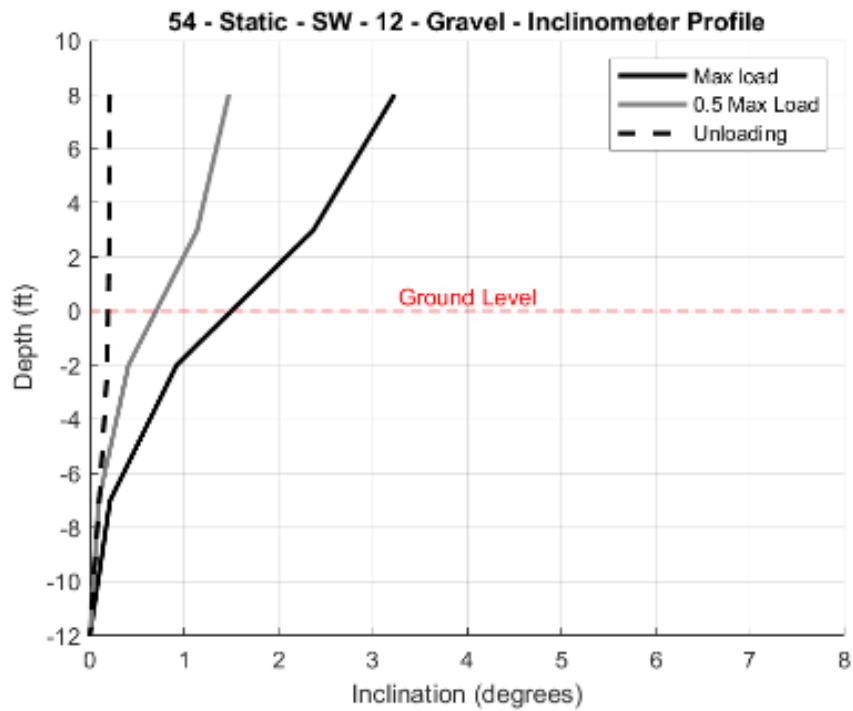
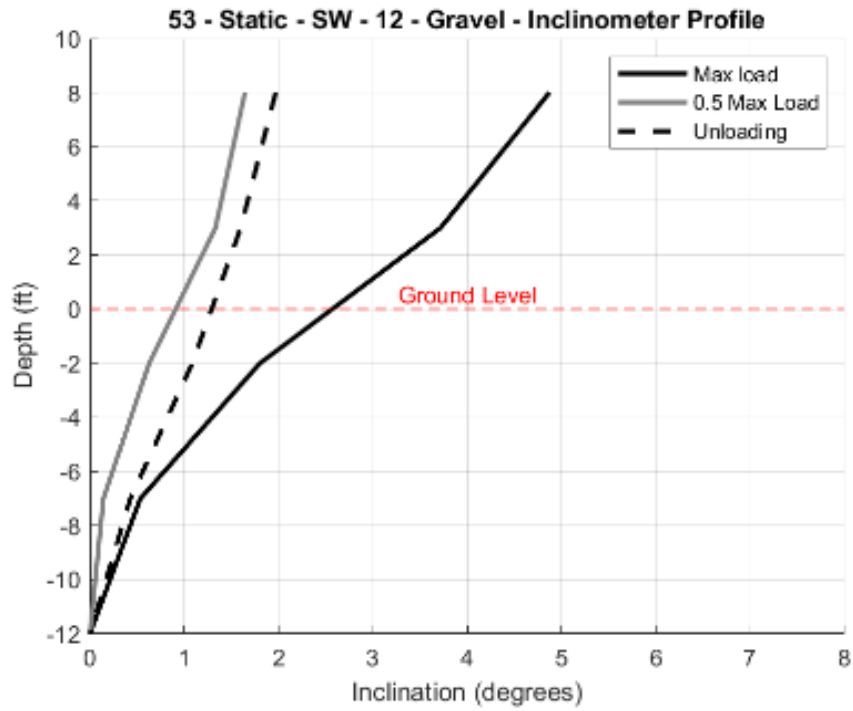


Figure D.7 The rotation vs inclination at ground level of static tests 53 and 54 on SW direction performed on pole 12 – Gravel, the 700-yr design load is approximately 0.5 of the maximum load

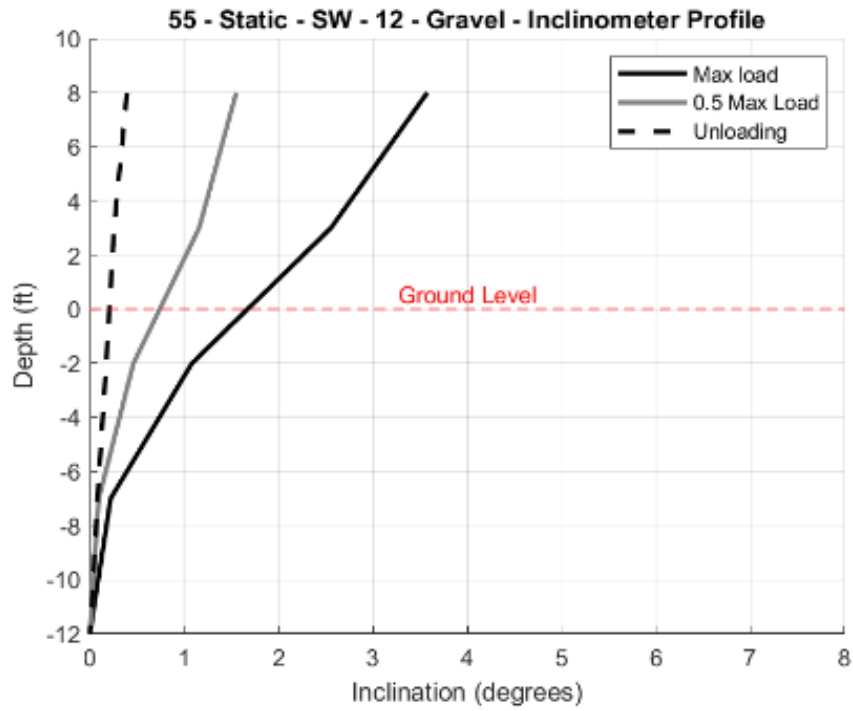


Figure D.7 The rotation vs inclination at ground level of static tests 53 and 54 on SW direction performed on pole 12 – Gravel, the 700-yr design load is approximately 0.5 of the maximum load

Appendix E Discussion on Musco Foundations

In an email in June 2024, NDOT asked to comment on foundations from Musco. Although Musco's foundation is beyond the scope of this project, this appendix was developed to explain its system in general terms. NDOT is encouraged to contact Musco directly.

Table F.1 illustrates an example of Musco's structural and foundation system. It is similar to the direct embed method used in the present work. However, key differences are noted:

- a) A precast concrete shaft is placed in the drilled shaft.
- b) A concrete shaft extends above the groundline as shown.
- c) The concrete backfill is placed against the precast and soil.
- d) Design reactions are provided in addition to the shaft size and depth.
- e) For the NDOT 80-ft standard pole, the ASD reactions are shown in Table F.1.
- f) Based on the table provided in the Foundation Schedule, types B1, B3, and B2 might be appropriate. These shafts are 42-in diameter with 14-ft. Note shafts A1, A2, and A3, which have 40-in diameters, are likely fine with the 14-ft depth. The suggested quantities are provided.
- g) Musco's system keeps the steel above the groundline, which eliminates any concern about soil-structure corrosion issues. It likely does not require the mastic membrane used in the direct embed.
- h) Like direct embed, the fatigue-prone details of welds, bolts, baseplates, etc. are removed as the pole-to-pile connection is a slip fit. There is a seam weld that could come into play.
- i) Assume soil parameters are shown on the plans.
- j) Note this is an example and likely varies depending on soil requirements.

The Musco system is a viable alternative to direct embed. Important differences in delivery method, cost, availability, etc. need to be understood; however, this is beyond the present scope. A good phase III project might be to test Musco's system similarly. The research team is well up on how this could be done.

Table E.1 AASHTO Standard Specification LTS summary

Axial Load (kip)	4.18
Shear Load (kip)	1.73
Moment (kip-ft)	89.8
Tip Translation (inch)	12.2
Base stress (ksi)	8.1
Base moment magnification factor	1.01

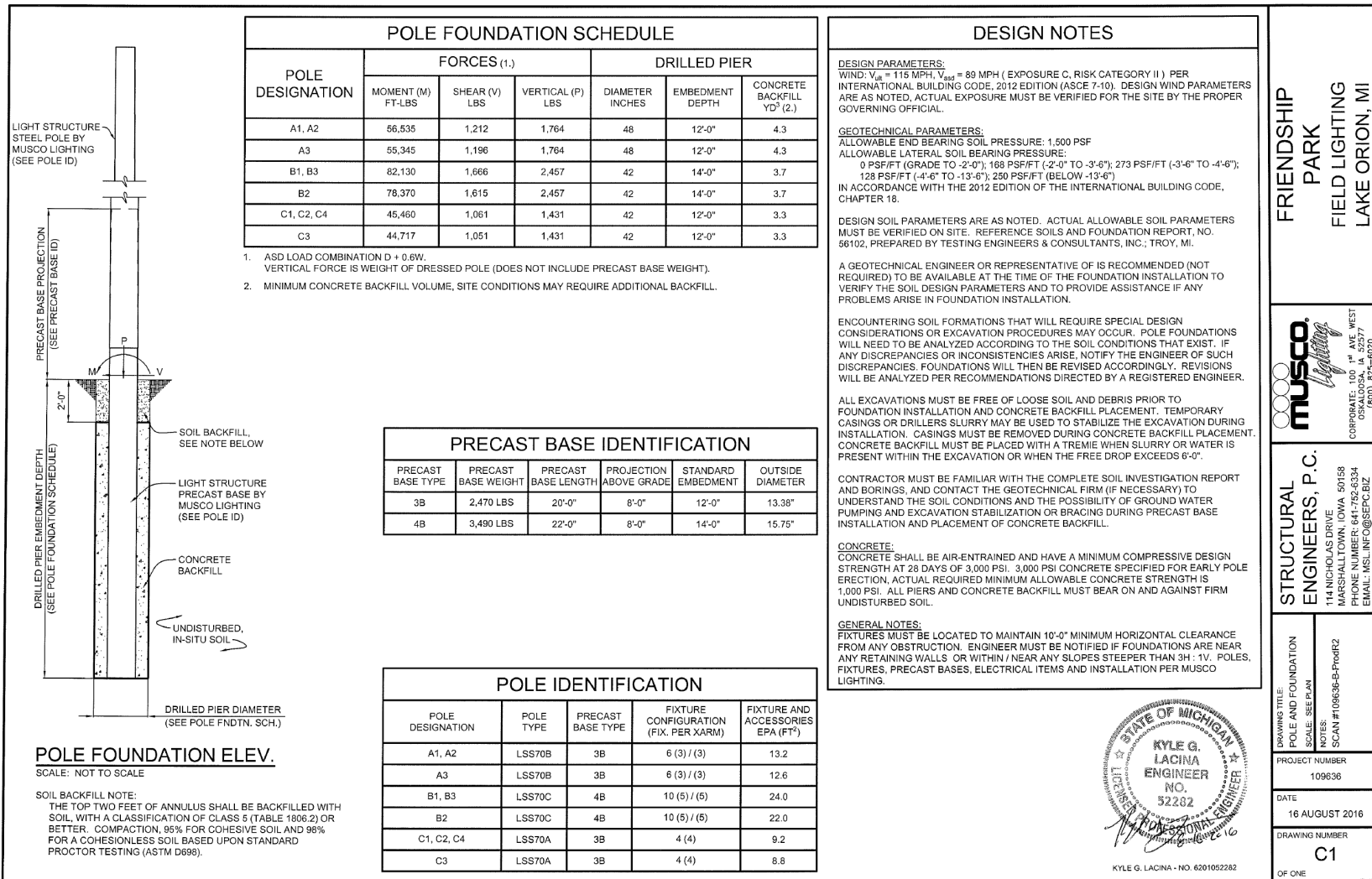


Figure E.1 Example foundation (<https://cms5.revize.com/revize/orionparks/RFP/2020/Ballfield%20Lighting%20RFP/2016.08.17%20-%20musco%20lighting%20submittal%20-%20revised%20%20-%20signed.pdf>)

Appendix F NDOT Sample Construction Specification for Direct Embedded Poles

F.1 Introduction

The following sample construction specifications were developed originally as part of the Phase I report. The Phase II work, presented herein, provided an opportunity to use/test the process and provide additional information. The following sections represent an adaptation and update from the Phase I report.

F.2 Qualifications and Submittals

Submit the following for review at least 10 working days before constructing drilled piers. NDOT review of the Contractor's personnel qualifications and installation plan does not relieve the Contractor of the responsibility for obtaining the required results in the completed work.

F.2.1 Personnel Qualifications

Construction Personnel. Use a supervisor with at least three years of experience in constructing directly embedded poles. The supervisor must remain on-site during all direct embedment installation activities. Upon request, provide a resume of job experience, a project description, and the agency's name, email address, and phone number.

F.2.2 Submittals

Furnish the following in the installation plan:

1. Details of proposed pier drilling methods; methods for removing materials from the piers; procedures for maintaining correct horizontal and vertical alignment of the excavation; and a disposal plan for the excavated material.
2. A description, including capacities, of the proposed equipment, including cranes, drills, drilling unit, augers, bailing buckets, and final cleaning equipment.
3. Demonstrate an understanding of the subsurface conditions at the site. Reference the available geotechnical report and/or any other subsurface data provided by the Company.
4. Details of methods to ensure drilled pier hole stability during excavation and concrete placement. Include a review of the chosen method's suitability for the anticipated site and subsurface conditions. If permanent casings are proposed or

required, provide casing dimensions and detailed procedures for permanent casing installation.

5. As applicable, details of bracing, centering centralizers, and lifting and support methods.
6. Details of Aggregate placement, including compaction methods.
7. Details of concrete placement, including proposed operations procedures for free fall, tremie, or pumping methods. Provide a summary of proposed actions to be taken when concrete does not meet minimum specifications or when unforeseen delays occur during the concreting process.

Other Required Submittals

1. Concrete Mix Design – if used
2. Concrete Aggregate Gradation – if used
3. Aggregate Backfill Gradation – if used
4. Direct Embedment Installation Record.

F.3 Execution

F.3.1 Drilling Operations

1. Excavate holes (Figure F.1) according to the installation plan. Report all deviations from the plan to the onsite inspector.
2. When required, casings shall be installed as the drilling proceeds or immediately after the equipment is withdrawn to prevent sloughing and caving of the excavation walls. The casing shall be advanced in the drilling operation to maintain a soil plug capable of producing a positive seal at the bottom that prevents piping of water or other material into or out of the hole.

3. Slurry may be used to stabilize the excavation; however, a specific plan, including the material to be used, must be submitted to NDOT for review prior to use. Refer to FHWA Standard Specifications for Construction of Road and Bridges, Section 565 “Drilled Shaft Installation” for all slurry use requirements.
4. Steel casings of ample strength to withstand handling and installation stresses shall be used. Use a casing with an outside diameter equal to or greater than the specified diameter of the pole and an inside diameter not exceeding the specified diameter of the pole by more than six (6) inches.
5. Each drilled shaft shall be accurately located, sized, and plumbed. The maximum deviation of the drilled pier from its designated location shall not be more than two inches at its top elevation. The drilled shaft shall not be out of plumb more than one (1) inch in five (5) feet of height.
6. Each drilled excavation shall be made to the approximate depth indicated on the drawings. All weathered and loose material shall be removed from the excavations. NDOT shall verify the final tip elevation before concrete or aggregate placement. Classification of the excavated materials will not be made except for identification purposes. Drilled excavation shall include the removal and handling of all excavated materials from the site.



Figure F.1 Drilling operations

F.3.2 Aggregate Placement

1. Backfill: Holes shall be backfilled with crushed aggregate backfill as specified on the Drawings.
2. Backfill shall be compacted in twelve (12) in. lifts until fully compacted as shown in Figure F.2.
3. Engineered backfill shall be banked and tamped twelve (12) in. above the natural ground surface.
4. Surplus excavated material shall be evenly spread along the right-of-way or hauled to an offsite location for dumping, according to the permissions and requirements of each landowner.
5. Lifts of aggregate backfill material shall not exceed twelve (12) inches in depth. Any extremely dry materials shall be dampened during the backfill operation to obtain the desired density.



Figure F.2 Gravel backfill is used to fill the drilled holes with a pneumatic tamper to ensure uniformly compacted around the annulus

F.3.3 Concrete Placement

1. Dry Method

Use the dry construction method at sites where the groundwater level and soil conditions are suitable to permit construction in relatively dry conditions and where the sides and bottom of the excavation may be visually inspected before placing concrete.

- i. Unless otherwise accepted by the NDOT, concrete shall be placed in drilled holes within 24 hours of completing excavation.
- ii. All water and loose materials shall be removed from the holes, and reinforcement shall be thoroughly cleaned before concrete is placed.
- iii. Free-fall concrete placement, up to sixteen (16) ft, tremie or funnel are acceptable means of installation in a dry hole.
- iv. The top six (6) feet of concrete shall be rodded or vibrated to provide a dense mass free of voids.
- v. If approved casings are left in place, the void areas between the form and the excavation walls shall be filled with lean concrete mix. The lean concrete or grout mix shall be placed and tamped to fill the annular space.
- vi. The volume of each drilled excavation shall be documented and compared to the concrete volume of each drilled pier. If the concrete volume placed is less than the calculated (theoretical) volume, the NDOT shall be notified immediately.
- vii. Concrete shall maintain a minimum six-inch slump for the duration of the pour.
- viii. Self-consolidated concrete may be used to meet NDOT specifications. In this case, rodding or vibrating per iv above is not necessary.



Figure F.3 Placing the concrete backfill and using an electric vibrator to ensure proper compaction

2. Wet Method

Use the wet construction method or the casing construction method for shafts that do not meet the above requirements for the dry construction method.

- i. Concrete shall not be deposited underwater except with NDOT permission. The proportions for underwater concrete mix shall be adjusted to provide seven to nine (7 to 9) inches of slump and the cement factor shall be increased by one sack per cubic yard.
- ii. Underwater concrete shall be placed through a tremie equipped with a seal at the lower end and a hopper at the upper end. The tremie shall be watertight and have a minimum diameter of six (6) times the maximum concrete aggregate size to allow a free flow of concrete. After the flow of concrete is started, the lower end of the tremie shall be kept below the surface of the deposited concrete. The entire mass of concrete shall be placed as quickly as possible and shall flow into place without shifting horizontally under the water.
- iii. Fluid within the excavation shall be stable when concrete is deposited and shall be maintained at a height necessary to ensure hydrostatic equilibrium during concrete placement, but not less than five (5) ft above the water table. After placing, the groundwater level in the area adjacent to the drilled shaft shall be kept static (no pumping) until the concrete has taken its initial set.
- ix. Concrete shall maintain a minimum seven (7)-inch slump for the duration of the pour.

F.4 Direct Embedment Installation Record

An accurate record of each pier installation and concrete placement shall be completed and contain, at a minimum, the information listed below. The Contractor shall submit the installation record to the Company Field Representative at the end of each day. Submitted records will not become official until the Company Field Representative agrees with the accuracy and completeness, and signs the document.

The drilled shaft installation record shall contain the following information:

- i. Contractor's name
- ii. Drilled shaft number and location
- iii. Overall depth of excavation
- iv. Depth to water
- v. Final depth, if different from design drawings
- vi. Note any caving, sloughing of excavation and drilling difficulties
- vii. Casing insertion, size and length, and whether or not removed
- viii. Date and time of start and finish excavation
- ix. Date and time concrete placed
- x. Calculated volume of excavation based on the diameter of shaft
- xi. Concrete batch plant ticket numbers

F.5 Project Contract Drawing

The drawings used to construct the four test pole are provided in Figure F.4. These drawings can be adapted for NDOT according to NDOT standards. The drawing is also provided in .pdf format within the project shared folder.

GENERAL NOTES:

- THIS DESIGN IS FOR RESEARCH PURPOSES ONLY BY UNIVERSITY OF NEBRASKA. LOAD TESTING SHALL BE PERFORMED IN A CONTROLLED MANNER UNDER THE SUPERVISION OF EXPERIENCED PERSONNEL. REFERENCES USED FOR ANALYSIS:
- SEE GUIDE FOR TRANSMISSION STRUCTURE FOUNDATION DESIGN AND TESTING, STD 891-2001.
- DESIGN LOADS:

	UNFACTORED LOAD CASE 1	FACTORED LOAD CASE 2
AXIAL	4.18 KIP	4.18 KIP
SHEAR	1.73 KIP	3.07 KIP
MOMENT	89.6 KIP-FT	159.6 KIP-FT

- LOADS LOCATED AT TOP OF FOUNDATION.
- EXERCISE CAUTION IF APPLYING TEST LOADS IN EXCESS OF THOSE IN THE ABOVE LOAD CASES.
- DESIGN ASSUMES 80 FEET TALL HIGH MAST LIGHT POLE WITH 22 INCH BASE DIAMETER AND SIDE WALL THICKNESS OF 3.375 INCHES BY VALMONT OR SIMILAR.
- EXISTING GEOTECHNICAL CONDITIONS:

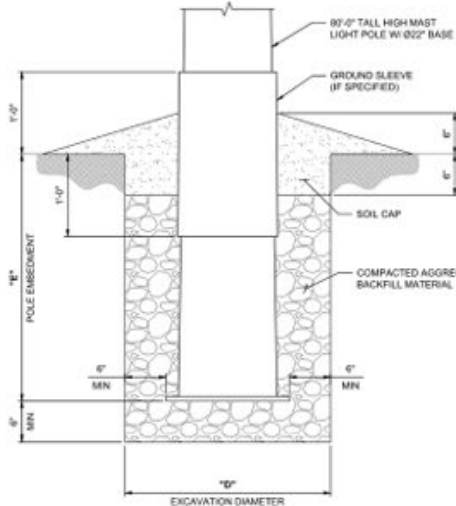
- GEOTECHNICAL DESIGN PARAMETERS AND CONDITIONS BASED ON PROVIDED BOREHOLE REPORT NO. 1 BY NEBRASKA DEPARTMENT OF TRANSPORTATION, DATED 7/14/22. TESTS SHALL BE LOCATED WITHIN THE PROPERTY THAT THE BOREHOLE WAS COMPLETED.
- THE EXISTING SUBGRADE IS UNDERSTOOD TO CONSIST OF LOOSE TO MEDIUM DENSE SAND AND SILTY SAND EXTENDING FROM THE GROUND SURFACE (ELEVATION 1183 FEET) TO A DEPTH OF 24 FEET (ELEVATION 1159 FEET).
- SOILING WAS TERMINATED IN SANDSTONE AT A DEPTH OF 25 FEET (ELEVATION 1158 FEET).
- GROUNDWATER WAS ENCOUNTERED AT A DEPTH OF 5.5 FEET BELOW GROUND SURFACE (ELEVATION 1177.5 FEET).

- DRILLING
- CONTRACTOR MAY USE TEMPORARY CASING.
- AGGREGATE BACKFILL:
- MATERIAL:
 - THE BACKFILL MATERIAL SHALL CONSIST OF A WELL BLENDED MIXTURE OF COHESIONLESS MATERIAL, CONSISTING OF THREE (3) PARTS OF No. 2 CRUSHED LIMESTONE AND ONE (1) PART OF No. 10 SAND. ALL MATERIAL SHALL CONSIST OF SOUND NATURAL MATERIAL AND CRUSHED AGGREGATES OF CLASSIFIED BY AGGREGATE SIZE DESIGNATIONS AND RANGES IN THE MECHANICAL ANALYSIS TEST ASTM D-448-86.
 - ALTERNATE BACKFILL GRADATIONS MAY BE USED WITH APPROVAL. LOCALLY AVAILABLE MATERIAL AND MIXTURES PROVIDING A RECOGNIZED COST AND PERFORMANCE ADVANTAGE CAN BE CONSIDERED SHOULD THE MAXIMUM AGGREGATE DIAMETER BE LESS THAN 1 INCHES. A WELL COMPACTED AND UNIFORMLY DENSE BLEND MUST BE OBTAINABLE CONSIDERING THE SITE CONDITIONS, BACKFILL MATERIAL, MOISTURE CONTENT AND TAMPING EQUIPMENT AND PROCEDURES AVAILABLE.
 - TO OBTAIN SATISFACTORY COMPACTION, THE BACKFILL MATERIAL MOISTURE CONTENT SHALL APPROACH OPTIMAL. THE OPTIMAL MOISTURE CONTENT SHALL BE DETERMINED USING ASTM D999-91. THE STATE OF COMPACTION SHALL BE EVALUATED USING ASTM D-4253-93.

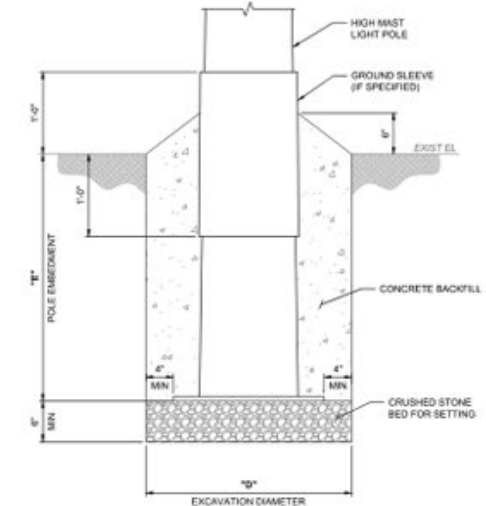
- PROCEDURE:
 - THE SUCCESSFUL PERFORMANCE OF EMBEDDED FOUNDATIONS IS DEPENDANT ON BACKFILL MATERIAL AND PARTICULARLY THE COMPACTION METHOD. THE BACKFILL SHALL BE THOROUGHLY TAMPED USING A SATISFACTORY MECHANICAL TAMPER. EACH LIFT SHALL NOT EXCEED 6 INCHES. TAMPING SHALL BE CONSISTENT WITH EACH LIFT USING A MINIMUM OF TWO (2) PASSES PER LIFT UNIFORMLY AROUND THE ANNULUS TO ACHIEVE A HIGH DEGREE OF AVAILABLE COMPACTNESS.
 - PRODUCE A SOIL CAP CONSISTING OF NATIVE CLAY SOILS OR A PREDOMINANTLY COHESIVE SOIL MIXTURE SUCH THAT THE COMPACTED BACKFILL MATERIAL IS SUFFICIENTLY COVERED. SLOPE THE SOIL CAP FROM THE POLE IN ALL DIRECTIONS AND COMPACT TO PREVENT FUTURE SURFACE WATER INFILTRATION AND DEPRESSIONS.
 - THE EXCAVATION AND ALL BACKFILL MATERIAL SHALL BE PROTECTED FROM CONTAMINATION BY WATER, MUD, SNOW, ICE OR FREEZING THROUGHOUT THE CONSTRUCTION PROCESS UNTIL ALL BACKFILL AND SOIL CAPS HAVE BEEN INSTALLED AND COMPACTED. BACKFILL MATERIAL ASSUMED TO BE PLACED IN THE DRY. NO SLURRY SUPPORT.

- CONCRETE BACKFILL:
 - ALL CONCRETE MATERIAL, PLACEMENT AND CURING SHALL BE PER ACI STANDARD SPECIFICATIONS.
 - SHALL ATTAIN A MINIMUM COMPRESSIVE STRENGTH (FC) OF 4000 PSI.
 - ALL EXPOSED CONCRETE SHALL BE FORMED OR FINISHED TO UNIFORM SURFACE. A SLOPING SURFACE FOR DRAINAGE SHALL BE USED AS REQUIRED.
- ALL MANUFACTURED ITEMS SHALL BE INSTALLED PER MANUFACTURER'S GUIDELINES AND SPECIFICATIONS.
- CONTRACTOR TO VERIFY ALL DIMENSIONS AND SITE CONDITIONS PRIOR TO COMMENCING WORK. ANY ERRORS, OMISSIONS, OR UNUSUAL CONDITIONS ARE TO BE REPORTED TO THE ENGINEER IMMEDIATELY.

ID	SECTION TYPE	BACKFILL TYPE	EXCAVATION DIAMETER (FT) "D"	EMBEDMENT DEPTH (FT) "E"	THEORETICAL DEFLECTION AT GROUND SURFACE (IN)	THEORETICAL PILE ROTATION AT GROUND SURFACE (DEG)
1	A	COMPACTED AGGREGATE	3	18	0.13	0.18
2	A	COMPACTED AGGREGATE	3	12	0.17	0.20
3	B	CONCRETE	3	18	0.04	0.03
4	B	CONCRETE	3	12	0.09	0.08



SECTION @ TYPE "A"
SCALE: 1/8"



SECTION @ TYPE "B"
SCALE: 1/8"

						PROJECT TITLE		PROJECT LOCATION		TSCD RISK	
						UNIVERSITY OF NEBRASKA RESEARCH PROJECT		LINCOLN, NE		LOW	
						PROJECT TASK		JOB-TASK NO.			
						HIGH MAST LIGHT POLE DIRECT EMBED FOUNDATIONS		23-000-550.01.02			
						SHEET TITLE		SHEET ID			
						TYPICAL SECTIONS & DETAILS		S-001			
MARK	DATE	DESCRIPTION	DRWN	DESG	CHKD						
B	04-19-23	ISSUED FOR CONSTRUCTION	P.R.K.	J.G.	J.G.						

Figure F.4 High mast light pole direct embed foundations. (a) gravel backfill , and (b) concrete backfill

Appendix G Service Analysis of NDOT Pole Design

NDOT's current standard high-mast pole was analyzed for a wind of 76 mph, which is a 10-year MRI prescribed for the Service I limit state. NDOT's standard pole has two steel sections:

1. 22-in diameter tapering to 17 in. at nominally 35 ft (0.375-in wall thickness), and
2. 17-in diameter tapering to 11 in. at nominally 80 ft (0.1875-in wall thickness).

Using a spreadsheet computation considering a simplified assumption of continuously changing diameter and wall thickness, the tip translation was estimated at 8.7 in. The pole was separately modeled in SAP2000, which discretized the pole into 20 nonprismatic sections, and the tip translation was estimated at 10.0.

According to the AASHTO LRFD LTS (Section 10.4.2), the acceptable translation for a high-mast pole is 10 percent of the height, $10\% (80 \text{ ft.} = 960 \text{ in.}) = 96 \text{ in.}$ The translation associated with the foundation rotation is $96 - 10 = 86 \text{ inches.}$ The base rotation could then be $86/960 = 0.09 \text{ radians (5.2 degrees).}$ This rotation far exceeds any tested rotations observed under loads more than double the Extreme I limit state.

Conclusion: Service I tip translation is not of concern, and the limiting movements at the top of the shaft should be based on judgment.

Appendix H Concrete Foundation Mixture Design

The concrete that was used for the foundations is presented in Table H.1

Table H.1 Concrete Mixture Design for the high-mast tower concrete foundations.

Material	Weight (lb)	Volume (cubic ft)
IL Cement	575	2.96
47B, Size 57 Limestone	915	5.51
47B Sand/Gravel	2104	12.87
Water	254	4.07
Air Content	6%	1.62